

https://dspace.org/

Proton induced radiation damage studies on plastic scintillators for the tile calorimeter of the atlas detector

Jivan, Harshna

2016

http://hdl.handle.net/10539/21672

Jivan, Harshna (2016) Proton induced radiation damage studies on plastic scintillators for the tile calorimeter of the atlas detector, University of the Witwatersrand, Johannesburg, <http://hdl.handle.net/10539/21672>

Downloaded from a DSpace repository. https://dspace.org/



UNIVERSITY OF THE
WITWATERSRAND,
JOHANNESBURG

PROTON INDUCED RADIATION DAMAGE STUDIES ON PLASTIC SCINTILLATORS FOR THE TILE CALORIMETER OF THE ATLAS DETECTOR

Harshna Jivan

Supersior: Bruce Mellado
Co-supervisor: Elias Sideras-Haddad

A Dissertation submitted to the Faculty of Science, University of the Witwatersrand, Johannesburg, in fulfilment of the requirements for the degree of Master of Science.

Johannesburg, 2016

Declaration

I declare that this Dissertation is my own, unaided work. It is being submitted for the Degree of Master of Science at the University of the Witwatersrand, Johannesburg. It has not been submitted before for any degree or examination at any other University.



_____

8th day of August 2016 in Johannesburg.

Abstract

Plastic scintillators play a key role in reconstructing the energy and tracks of hadronic particles that impinge the Tile Calorimeter of the ATLAS detector as a result of high energy particle collisions generated by the Large Hadron Collider of CERN. In the detector, plastic scintillators are exposed to harsh radiation environments and are therefore susceptible to radiation damage.

The radiation damage effects to the optical properties and structural damage were studied for PVT based commercial scintillators EJ200, EJ208, EJ260 and BC408, as well as PS based UPS923A and scintillators manufactured for the Tile Calorimeter. Samples of dimensions 5x5x0.3 mm were subjected to irradiation using 6 MeV protons to doses of approximately 0.8 MGy, 8 MGy, 25 MGy and 25 MGy using the 6 MV tandem accelerator of iThemba LABS.

Results show that damage leads to a reduced light output and loss in transmission character. Structural damage to the polymer base and the formation of free radicals occur for doses $\geq$ 8 MGy leading to reduced scintillation in the base and re-absorption of scintillation light respectively. Scintillators containing a larger Stokes shift, i.e. EJ260 and EJ208 exhibit the most radiation hardness. EJ208 is recommended as a candidate to be considered for the replacement of Gap scintillators in the TileCal for the 2018 upgrade.

Related research outputs

Published proceedings:

H. Jivan, R. Erasmus, B. Mellado, G. Peters, K. Sekonya and E. Sideras-Haddad, "Radiation hardness of plastic scintillators for the Tile Calorimeter of the ATLAS detector", *Proceedings of SAIP2014, the 59th Annual Conference of the South African Institute of Physics*, edited by Chris Engelbrecht and Steven Karataglidis (University of Johannesburg, July 2014), pp.199-205. ISBN: 978-0-620-65391-6.

H. Jivan, B. Mellado, E. Sideras-Haddad, R. Erasmus, S. Liao, M. Madhuku, G. Peters and O. Solvyanov, "Radiation hardness of plastic scintillators for the Tile Calorimeter of the ATLAS detector", *Journal of Physics: Conference Series*, vol. 623, no. 012016, 2015. doi:10.1088/1742-6596/623/1/012016.

H. Jivan, E. Sideras-Haddad, R. Erasmus, S. Liao, M. Madhuku, G. Peters, K. Sekonya and O. Solvyanov, "Radiation hardness of plastic scintillators for the Tile Calorimeter of the ATLAS detector", *Journal of Physics: Conference Series*, vol. 645, no. 012019, 2015. doi:10.1088/1742-6596/645/1/012019

S. Liao, R. Erasmus, H. Jivan, C. Pelwan, G. Peters and E. Sideras-Haddad, "A comparative study of the radiation hardness of plastic scintillators for the upgrade of the Tile Calorimeter of the ATLAS detector", *Journal of Physics: Conference Series*, vol. 645, no. 012021, 2015. doi:10.1088/1742-6596/645/1/012021

Submitted proceedings:

S. Tlou, H. Jivan, B. Mellado, R. Erasmus, M. Madhuku, K. Sekonya and E. Sideras-Haddad, "Impact of dose rate on radiation damage of plastics scintillators for the Tile Calorimeter of ATLAS", submitted to *Proceedings of SAIP2015, the 60th Annual Conference of the South African Institute of Physics*.

Other conference and workshop outputs:

Oral Presentation: “Study of Proton induced radiation damage in plastic scintillators for the Tile Calorimeter of the ATLAS detector”, at the *DST-NRF Centre of Excellence in strong materials Annual student workshop*, Wits University, 2016.

Oral Presentation: “Radiation hardness of plastic scintillators for the Tile Calorimeter of the ATLAS detector”, at the *High energy particle physics workshop (HEPPW2016)*, iThemba LABS, 2016.

Poster Presentation: “Radiation hardness of plastic scintillators for high energy physics detector applications”, at the *7th Cross Faculty Graduate Symposium*, Wits University, 2015.

Oral Presentation: “Radiation damage of plastic scintillators for the Tile Calorimeter of the ATLAS detector”, at the *NECSA-WITS workshop on radiation, material science and high energy physics*, Pelindaba, 2015

Poster Presentation: “Radiation hardness of plastic scintillators for high energy physics detector applications including the upgrade of the Tile Calorimeter of ATLAS”, at the *DST-NRF Centre of Excellence in strong materials Annual student workshop*, Wits University, 2015.

Oral presentation: “Radiation damage of plastic scintillators for high energy physics detector applications”, at *The South African Raman workshop*, Wits University, 2014.

Poster Presentation: “Radiation damage of plastic scintillators for high energy physics detector applications”, at the *6th Cross Faculty Graduate Symposium*, Wits University, 2014.

Abstracts accepted:

Oral Presentation: “Proton induced radiation damage to the fluorescence capability of plastic scintillators for the Tile Calorimeter of ATLAS”, to be presented at the *60th Annual Conference of the South African Institute of Physics*, July 2016.

Oral Presentation: “A study into the rate of photo-bleaching undergone by radiation damaged plastic scintillators”, to be presented at the *60th Annual Conference of the South African Institute of Physics*, July 2016.

Acknowledgments

I would like to convey my sincere gratitude to my advisors Prof Bruce Mellado and Prof Elias Sideras-Haddad. I have gained an invaluable amount of experience whilst working on this project. Thank you for challenging me and my abilities, pushing me to achieve my very best and motivating me when I needed it most.

To Dr Rudolph Erasmus, thank you for showing me the ropes for use of the Varian Cary spectrophotometer, the LabRAM HR Raman spectrograph and for all your assistance in conducting the Raman spectroscopy and fine tuning of the fluorescence testing. My research would not be where it is were it not for your willingness to lend a hand and your helpful suggestions.

Thank you to iThemba LABS, Gauteng, for allowing the use of the 6 MV Tandem accelerator. To Dr Morgan Madhuku, Mr Fritz Baltzun and Mr Oleg Pekar, thank you for assisting me with the proton irradiations and for the countless hours spent on fine tuning of the beam optics.

I also wish to covey thanks to the following people:

- Mr Gerrard Peters for fashioning the ideal sample preparation method.
- Mr Vincent Govender and staff at the workshop for making up all of the samples holders, mounts and odd parts needed for experiments.
- Mr Oleg Solovyanov for assisting me with use of the light box set-up at CERN
- Members of the TileCal community, particularly the late Mrs Eirini Vichou and Mrs Anna Hendriques, for their positive suggestions as well as for procuring the scintillators under study.

On a personal note, I wish to convey my utmost appreciation and gratitude to my mum, Maya, my sister Rupal and my fiancé Nishaan, as well as to the rest of my extended family and friends who have supported me along the way.

"It is only a paper moon
Sailing over a cardboard sea
But it wouldn't be make believe
If you believed in me"

The support of the DST-NRF Centre of Excellence in Strong Materials (CoE-SM) towards this research is hereby acknowledged. The financial assistance of the National Research Foundation (NRF) towards this research is hereby acknowledged. Opinions expressed and conclusions arrived at, are those of the author and are not necessarily to be attributed to the CoE-SM or to the NRF.

Contents

Declaration ..... **i**

Abstract ..... **ii**

Related research outputs ..... **iii**

Acknowledgments ..... **v**

List of Figures ..... **ix**

List of Tables ..... **xiii**

Nomenclature ..... **xiv**

1 Introduction **1**

1.1. Motivation 1

1.2. Research aims and objectives 3

1.3. Presentation of chapters 4

2 The Tile Calorimeter of the ATLAS detector **5**

2.1. The ATLAS co-ordinate system 7

2.2. Plastic scintillators in the Tile Calorimeter 8

2.2.1. The Barrel regions 8

2.2.2. The Gap regions 10

2.3. The radiation environment of plastic scintillators in the Tile Calorimeter of the ATLAS detector 12

3 Scintillation and Plastic Scintillators **14**

3.1. The scintillation mechanism 14

3.2. Radiation damage in plastic scintillators 17

3.3. Description of plastic scintillators under study 20

4 Experimental details 23

4.1. Overview of radiation damage methods 23

4.1.1. SRIM simulations 23

4.1.2. Sample preparation 25

4.1.3. Proton irradiation at iThemba LABS Gauteng 28

4.1.4. Calculation of dose 30

4.2. Overview of the techniques used to analyse damage 31

4.2.1. Light Transmission spectroscopy 31

4.2.2. Light yield testing in response to ^{90}Sr 32

4.2.3. Fluorescence spectroscopy 33

4.2.4. Raman Spectroscopy 35

5 Results and analysis 36

5.1. Observations 36

5.2. Results of the light transmission 37

5.2.1. Features in the transmission spectra 37

5.2.2. Comparison of light transmission loss 39

5.3. Results of the light yield studies 42

5.4. Results of the fluorescence studies 47

5.4.1. Fluorescence peak features 47

5.4.2. Photo-bleaching vs time correlation 48

5.4.3. Comparison of fluorescence results 50

5.5. Results of Raman spectroscopy 52

5.5.1. Structural damage as a function of dose 54

5.5.2. Healing of structural damage 56

6 Conclusion 58

Appendix A 61

Appendix B 65

Appendix C **73**

Appendix D **79**

Appendix E **85**

Appendix F **91**

References **93**

List of Figures

Figure 2-1: A computer generated image of the ATLAS detector [ATLAS Experiment © 2013 CERN] 5
Figure 2-2: Schematic diagram of the particle interactions through a wedge of the ATLAS detector. 7
Figure 2-3: Diagram depicting the ATLAS calorimeter regions. 8
Figure 2-4: Representation of a Tile Module and its various components 10
Figure 2-5: Layout of the ITC scintillators relative to the cells of the Tile Calorimeter barrels 11
Figure 2-6: Photograph of the Gap region. The MBTS are indicated by 1 and the cryostat scintillators are indicated by 2. 11
Figure 2-7: Radiation map of the total ionising dose accumulated over a year in the calorimeter region at $\sqrt{s}$=14 TeV and nominal luminosity of 10^{34} $cm^{-2}s^{-1}$ .. 12
Figure 3-1: Energy level diagram of an organic molecule with π-electron structure, adapted from [1]. 15
Figure 3-2: Radiative transfer of energy between polymer base, primary and secondary fluors adapted from [15]. 17
Figure 3-3: (a) Pulse height spectra for BC505 samples before and after the 5 Mrad irradiation. (b) The transmission spectra for the BC505 sample. (c) The transmission spectra for the undoped base of BC505 before and after the 5 Mrad irradiation. Obtained from [19]. 18
Figure 3-4: Photographs of plastic scintillators under study 20
Figure 4-1: TRIM simulation of 6 MeV protons in PVT target. 24
Figure 4-2: Plot of the range over which protons stop within the PVT and PS targets. 25
Figure 4-3: Photographs of (a) the Buehler IsoMet cutting machine, (b) a front view of an EJ260 bar being cut, (c) a side view of the EJ260 bar being cut. ... 26
Figure 4-4: Aluminium holders used to mount the samples onto before polishing. 26
Figure 4-5: Photographs of the Struers polishing machine. 27

Figure 4-6: The final product of a polished sample, and a sample mounted into the brass holder. 28
Figure 4-7: Schematic representation of the tandem accelerator at iThemba LABS. 28
Figure 4-8: Photograph of proton beam line leading to the nuclear microprobe chamber. 29
Figure 4-9: Photograph of sample carousel before being lowered into microprobe chamber 30
Figure 4-10: Photograph of the Varian Cary 500 spectrophotometer. 32
Figure 4-11: Set-up of the light box used to test the light yield. 33
Figure 4-12: (a) Back view showing the path travelled by the laser into the LabRAM HR, (b) front view of the spectrograph, (c) zoomed view of the sample undergoing fluorescence. 34
Figure 5-1: EJ208 samples irradiated to doses of ~80 MGy, 25 MGy, 8 MGy and 0.8 MGy from left to right. 36
Figure 5-2: Fading of discolouration observed in ~25 MGy irradiated EJ208 samples. 36
Figure 5-3: Relative transmission spectra at several dose for the different scintillator types, taken four weeks after irradiation. 39
Figure 5-4: Relative transmission at 430 nm for the various sample types measured 4 weeks after irradiation. 40
Figure 5-5: Relative transmission for the various sample types at their respective wavelengths of maximum emission, measured 4 weeks after irradiation. 42
Figure 5-6: 2D mapping of the PMT signal with Sr90 source position, indicating signal regions corresponding to regions on the experimental set-up. 43
Figure 5-7: 3D mappings of the light yield for several EJ200 samples with different levels of proton induced radiation damage. 44
Figure 5-8: The effect of the experimental systematics on the measured light yield signal. 45
Figure 5-9: Relative light yield as a function of radiation damage dose. 46

Figure 5-10: Spectra showing the photo-bleaching of fluorescence lights with laser exposure time for an un-irradiated EJ200 sample. 49
Figure 5-11: Representation of how the correction factor *'C'* was computed using the photo-bleaching correlation curves and relevant equations 50
Figure 5-12: Fluorescence loss at 430 nm. 51
Figure 5-13: Fluorescence loss integrated over 300-500 nm 51
Figure 5-14: Raman spectra for the un-irradiated plastic scintillator samples.. 53
Figure 5-15: Raman spectra for EJ208 samples. 54
Figure 5-15: Possible configurations resulting from dehydrogenation of benzene. 55
Figure 5-16: Background subtracted Raman spectra for EJ200 sample measured several days after radiation exposure to a dose of 8.11 MGy. 56
Figure 5-17: Plot of Raman peak intensity ratios relative to the C-C aromatic peak intensity for EJ200 sample irradiated to 8.11 MGy. 57
Figure B-1: Beam current distributions for the various EJ200 samples. 67
Figure B-2: Beam current distributions for the various EJ208 samples. 68
Figure B-3: Beam current distributions for the various EJ260 samples. 69
Figure B-4: Beam current distributions for the various BC408 samples. 70
Figure B-5: Beam current distributions for the various UPS923A samples. 71
Figure B-6: Beam current distributions for the various TileCal samples. 72
Figure C-1: Transmission spectra relative to air for BC408 samples irradiated to doses of: (a) 1.06, (b) 1.00, (c) 8.07, (d) 8.44, (e) 29.2, (f) 26.0, (g) 82.9 and (h) 97.2 MGy. 73
Figure C-2: Transmission spectra relative to air for EJ200 samples irradiated to doses of: (a) 0.90, (b) 1.08, (c) 8.06, (d) 8.11, (e) 25.8, (f) 25.7, (g) 76.1 and (h) 73.1 MGy. 74
Figure C-3: Transmission spectra relative to air for EJ208 samples irradiated to doses of: (a) 0.858, (b) 0.825, (c) 8.80, (d) 8.30, (e) 24.8, (f) 26.4, (g) 80.8 and (h) 83.1 MGy. 75
Figure 6-4: Transmission spectra relative to air for EJ260 samples irradiated to doses of: (a) 1.18, (b) 1.07, (c) 8.88, (d) 8.54, (e) 22.7, (f) 26.2, (g) 94.2 and (h) 86.5 MGy. 76

Figure C-5: Transmission spectra relative to air for UPS923A samples irradiated to doses of: (a) 0.934, (b) 0.904, (c) 10.7, (d) 6.50, (e) 25.7, (f) 28.3, (g) 81.6 and (h) 86.2 MGy. 77
Figure C-6: Transmission spectra relative to air for TileCal samples irradiated to doses of: (a) 0.955, (b) 0.948, (c) 8.23, (d) 6.60, (e) 25.7, (f) 25.3, (g) 88.9 and (h) 78.5 MGy. 78
Figure D-1: Fluorescence spectra for various EJ200 samples (a-d), and their respective photo-bleaching rate curves (e-h). 79
Figure D-2: Fluorescence spectra for various EJ208 samples (a-d), and their respective photo-bleaching rate curves (e-h). 80
Figure D-3: Fluorescence spectra for various EJ260 samples (a-d), and their respective photo-bleaching rate curves (e-h). 81
Figure D-4: Fluorescence spectra for various BC408 samples (a-d), and their respective photo-bleaching rate curves (e-h). 82
Figure D-5: Fluorescence spectra for various UPS923A samples (a-d), and their respective photo-bleaching rate curves (e-h). 83
Figure D-6: Fluorescence spectra for various Tile Cal samples (a-d), and their respective photo-bleaching rate curves (e-h). 84
Figure E-1: Raman spectra for EJ200 samples. 85
Figure E-2: Raman spectra for EJ208 samples. 86
Figure E-3: Raman spectra for BC408 samples. 87
Figure E-4: Raman spectra for EJ260 samples. 88
Figure E-5: Raman spectra for UPS923A samples. 89
Figure E-6: Raman spectra for Tile Cal samples. 90

List of Tables

Table 3-1: Table summarising the various properties of the scintillators under study. 21
Table 5-1: Summary of peak allocation to functional and vibrational groups .. 54
Table B-1 summarising the proton irradiation conditions for EJ200, EJ208 and EJ260 samples. 65
Table B-2 summarising proton irradiation conditions for BC408, UPS923A and TileCal samples. 66

Nomenclature

ATLAS	A Torroidal LHC Apparatus
CERN	European Organization for Nuclear Research
EB	Extended Barrel
HEP	High Energy Physics
ID	Inner detector
ITC	Intermediate Tile Calorimeter
LAr	Liquid Argon
LB	Long Barrel
LHC	Large Hadron Collider
PMT	Photo-Multiplier Tube
PS	Polystyrene [C_8H_8]
PVT	Polyvinyl toluene [C_9H_{10}]
POPPOP	1,4-bis(5-phenyloxazol-2-yl) benzene [$C_{24}H_{16}N_2O_2$]
PTP	para-Terphenyl [$C_{18}H_{14}$]
Run 1	LHC operation at p-p energies of 3-7 TeV (2009 - 2012)
Run 2	LHC operation at p-p energies of 13 TeV (2015 - 2018)
SCT	Semi-Conductor tracker
TileCal	Tile Calorimeter, hadronic calorimeter of ATLAS
TRT	Transition Radiation tracker
WLS fiber	Wavelength shifting fiber
$\delta(X-X)$	Scissoring/Twisting/Rocking vibration of $X-X$ bond
$\nu(X-X)$	Stretching vibration of $X-X$ bond
$X-X$	Skeletal representation for single bond between X elements
$X=X$	Skeletal representation for double bond between X elements
$X\cong X$	Skeletal representation for triple bond between X elements

1 Introduction

Plastic scintillators are organic materials which exhibit the effect of luminescence when interacting with ionising radiation. Incident radiation causes electronic excitations within the scintillator material which then relax back to their ground state through the fluorescence process where emission of light occurs [1]. Since the amount of light emitted is dependent on the energy of the exciting particle, scintillators can be utilized for particle identification and hence play an important role in the field of detector physics.

In addition to detection of ionising particles, plastic scintillators can be used for neutron identification since neutrons can elastically scatter with hydrogen, resulting in proton recoils. Plastic scintillators have been used for a vast number of applications. They are employed in radiation dosimetry in medical physics and in cosmic detection systems like the Alpha Magnetic Spectrometer (AMS) in the field of astrophysics, but it is their applications to high energy detector systems that are of interest to this study.

1.1. Motivation

The ATLAS detector (A Torroidal LHC Apparatus), is a multipurpose detector involved in the search for new particles through the reconstruction of high energy proton-proton (p-p) collisions generated at the Large Hadron Collider (LHC) of CERN. During the data taking period of 2009-2012 (Run1), the LHC generated p-p collisions at energies of up to $\sqrt{s} = 7$ TeV, and in 2012, ATLAS announced the discovery of a boson consistent with that of the Higg's boson. This discovery lends support to the idea of the existence of a Higg's field which plays a crucial role in explaining how particles gain mass. [2]. The Tile calorimeter of ATLAS contains tiles of plastic scintillators which provide the key detection mechanism for detecting hadronic jets and showers of quarks and gluons that result from the proton-proton collisions.

Plastic scintillators are ideal for use in the Tile calorimeter since their properties of high light output and high optical transmission ensure that good resolution in measurements can be achieved. Their fast rise and decay times are ideal since fast timing responses are required [1]. Furthermore, plastic scintillators are easier to manufacture as compared to inorganic crystals which require special growing methods that can prove to be costly. As a result, plastic scintillators are more cost effective for covering large detector areas [3].

The main drawback of plastic scintillators however, is their susceptibility to radiation damage. When charged particles pass through a scintillator, they dissipate their energy to the scintillator molecules via ionization losses. This generates a large number of electronic excitations along the path of the particle which may fluoresce to emit light. Ionization may also lead to the formation of ions and free radicals which can affect both the structural and optical properties of the scintillators. Any processes occurring that reduce the intensity of fluorescence emission are regarded as quenching processes.

Radiation damage may lead to additional quenching of the scintillation light emitted by a scintillator [1]. This introduces an error into the data acquired by the detector, and if not accounted for correctly, can compromise the credibility of the detector accuracy. As the amount of radiation exposure is increased, these light losses may become more significant. Therefore, plastic scintillators that are employed need to exhibit a certain degree of tolerance against radiation damage.

Presently, the LHC is undertaking several upgrades in order to broaden the scope of physics that can be studied. In 2015, Run2 began with the first beams of 13 TeV being reached. In addition, the LHC plans to increase the luminosity (number of proton collisions per bunch crossing) by a factor of 10 beyond its design value after 2022.

These upgrades will significantly impact the radiation environment that scintillators are exposed to. Several new collider and detection systems are also presently under discussion with plans to commence within the next 20 years. Some of these plan to run at much higher energy and luminosities [4].

As such, a need has arisen for a study into how sustainable current available scintillators used in high energy physics detectors are. Furthermore, the Tile Calorimeter has implemented a series of upgrades in order to ensure that the detector performance can be sustained for several years to come. Part of phase two of this upgrade will be implemented in 2018 where scintillators from the Gap region of the Tile Cal will be replaced with more radiation tolerant plastics.

This study, therefore, investigates the radiation damage undergone by polystyrene and polyvinyl toluene based plastic scintillators after exposure to proton irradiation. Proton irradiation was decided upon since the Tile calorimeter interacts with hadrons. In addition, the proton carries charge and would therefore account for the coulomb interactions that occur in collisions between charged particles. The facilities for proton irradiation were readily available for the study, i.e. the 6 MV Tandem accelerator of iThemba LABS.

Scintillators obtained from Eljen Technologies, Saint Gobain Crystals as well as those presently used by the Tile Calorimeter of ATLAS have been investigated. This study forms part of a larger investigative effort that will be used for choosing the scintillator replacement candidate for the 2018 upgrade of the Tile Calorimeter.

1.2. Research aims and objectives

The Primary aim of this study is to obtain a comprehensive understanding of how radiation damage from proton irradiation occurs in current “radiation hard” plastic scintillators which are typically employed in present day high energy detectors. The research aims to understand how this radiation damage affects the scintillator on a structural level and how this in turn affects the optical properties of the scintillator.

The study further aims to perform a comparative assessment of the radiation hardness between several plastic scintillators available to the study which are typically employed within high energy detection systems today. This comparative analysis will then aid in the decision making of which scintillator grade will be

used to replace the current Gap scintillators of the Tile Calorimeter in the ATLAS detector during the Phase 2 upgrade in 2018.

The information gathered in this study will also aid in improving the future of the plastic scintillator industry. If plastic scintillator design can be improved to accommodate for these damage mechanisms, future plastics could exhibit more resilience against radiation as will be required for future high energy collider and detector systems.

In order to realise these aims, the following objectives have been set:

(1) Study and analyse the change in light transmission as a function of proton irradiation dose in each sample type.
(2) Identify the loss to light yield as a function of damage by studying the response of the scintillators to a radioactive Sr^{90} source.
(3) Study the effect of damage to the fluorescence capability of the scintillators upon UV laser excitation.
(4) Identify the change to bonding structure in each sample as a function of proton dose exposure using Raman spectroscopy (A technique based on the Raman Effect, described in section 4.2.2).
(5) Study the damage recovery to both the structural and optical properties of the scintillators.
(6) Perform a comparative of the radiation hardness between the different scintillators under study.

1.3. Presentation of chapters

In chapter 2, an overview of the Tile calorimeter is given with focus on how plastic scintillators are used to generate a signal in the detector. The scintillation mechanism and radiation damage mechanisms are discussed in chapter 3.

Chapter 4 describes the experimental procedures followed for inducing radiation damage in thin plastic scintillator samples using 6 MeV protons, and describes the analysis techniques used for assessing this damage. The results of this study are presented in chapter 5, with conclusions summarised in chapter 6.

2 The Tile Calorimeter of the ATLAS detector

The ATLAS detector [5] is a general purpose detector at the Large Hadron collider of CERN. It spans a length of 42 m, a diameter of 25 m and weighs a heavy 7000 tons. Proton bunches are accelerated within the 27 km long LHC tunnels and two beams are sent towards each other, which collide at the interaction point at the centre of the detector. Various particle fragments result from the collisions and interact with the various detector layers.

The ATLAS detector contains four main components which each play a significant role in reconstructing the original collision in order for new physics to be probed. These are the inner detector, the calorimeters, the muon spectrometer and the magnetic system. A schematic representation of the ATLAS detector is shown in Figure 2-1.

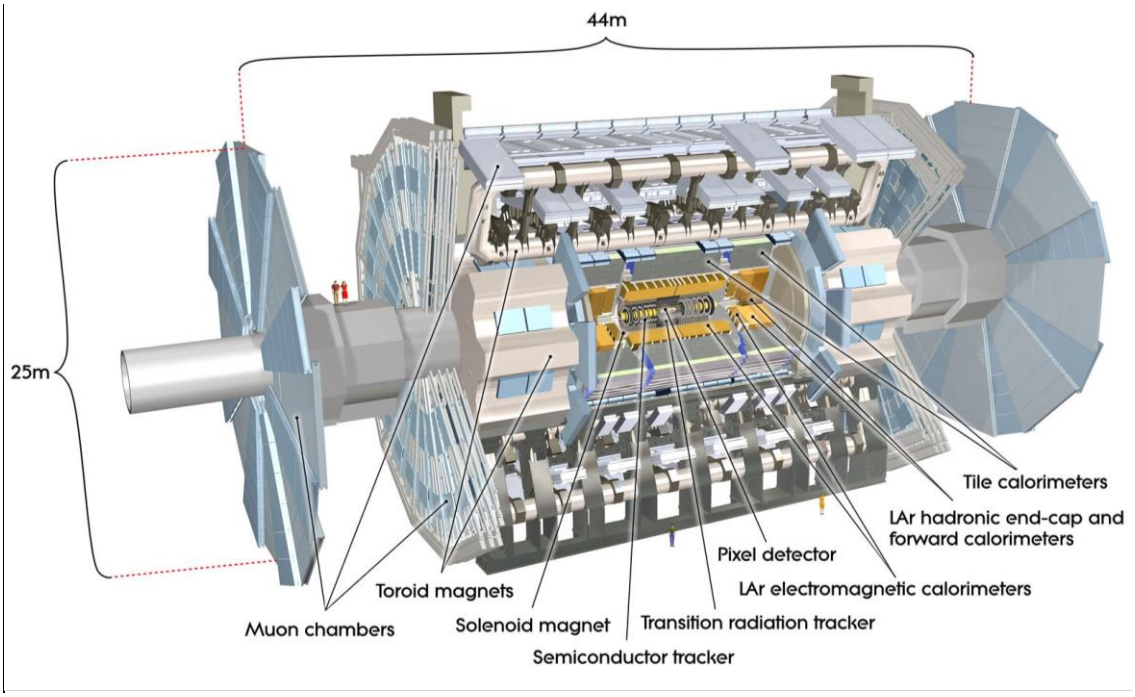


Figure 2-1: A computer generated image of the ATLAS detector [ATLAS Experiment © 2013 CERN]

The Inner Detector (ID) is situated closest to the beam pipe. It consists of three sub-detectors; the Pixel detector, the Semi-Conductor Tracker (SCT) and the Transition Radiation Tracker (TRT), and is surrounded by a superconducting

solenoid magnet which generates a 2 Tesla magnetic field. The ID is used for measuring the tracks of charged particles that emerge from the collisions. The tracks are curved due to the influence of the magnetic field, enabling their momenta to be determined.

Surrounding the ID concentrically are the Electromagnetic Calorimeters and the Tile Calorimeter, hadronic end-cap and forward calorimeters. The Calorimeters are based on “Sampling Calorimeter” technologies and are used to measure the energy of both charged and neutral particles. The calorimeters are designed to contain all electromagnetic and hadronic showers developing within them, and only neutrinos and muons manage to exit from these layers.

The Muon spectrometer surrounds the calorimeters and operates within a magnetic field generated by eight toroidal magnets. The Muon spectrometer measures the tracks of muons as they are bent by this magnetic field. Neutrino’s pass through ATLAS undetected.

A schematic of how the different particles interact through a wedge in the ATLAS detector is shown in Figure 2-2. A more detailed description of how each sublayer works in order to detect or track particles is provided in Appendix A.

The interactions of the various particles, resulting from the collision, with the different detector layers generate a huge amount of data. The ATLAS detector therefore incorporates a trigger and data acquisition (DAQ) system in order to only record events containing physics potential. This three level system uses particular selection criteria, with each level refining the decision made by its predecessor.

The recorded data is then analysed using complex algorithms which aim to reconstruct the original event. Monte Carlo simulations of theoretical models predict the complex physics processes that could occur during collisions. These simulations are compared to experimental data. When excesses in the data are observed as compared to predictions, this indicates a potential discovery.

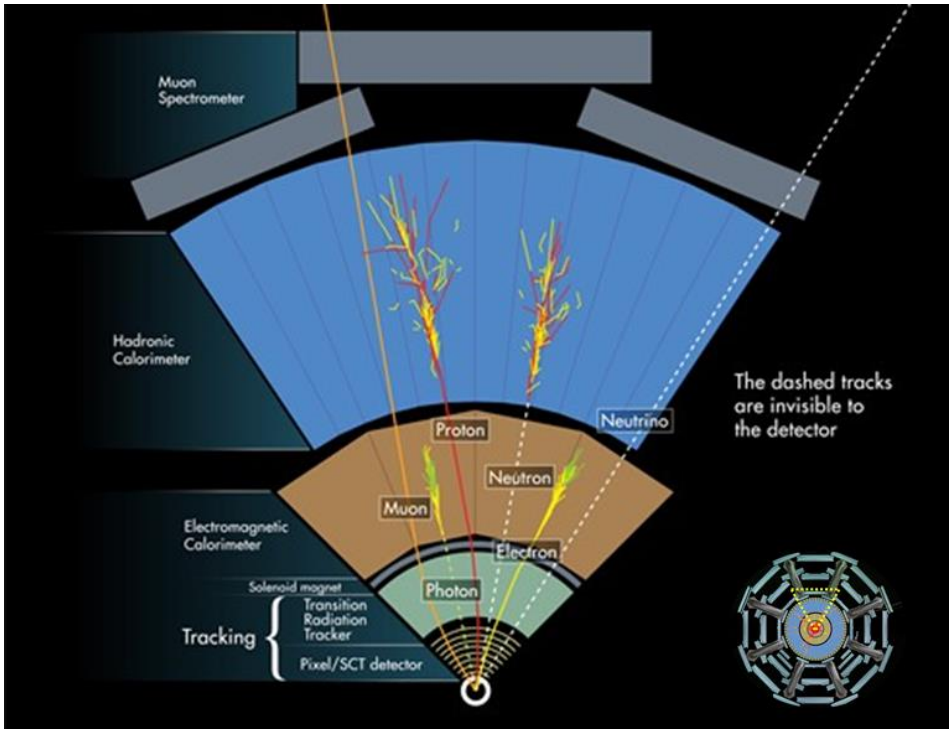


Figure 2-2: Schematic diagram of the particle interactions through a wedge of the ATLAS detector.

2.1. The ATLAS co-ordinate system

The ATLAS co-ordinate system [5] is defined around the interaction point being the origin. The longitudinal z-axis coincides with the length of the beam line. The "A-side" of the detector corresponds to the region with positive z-values, and the "C-side" corresponds to the other half. The transverse x-y plane corresponds to the region perpendicular to the beam pipe. The positive x-axis points from the interaction point to the centre of the LHC ring. The positive y-axis points upward to the surface of the earth.

The transverse plane is generally described in terms of r-φ coordinates. The radial dimension "r", measures the distance from the beam line. The azimuthal angle "φ", measures the angle around the beam pipe from the x-axis. The polar angle "θ", is the angle around the y-axis from the positive z-axis. The spatial co-ordinate preferred within most hadronic colliders however, is pseudorapidity "η" [6]. It is defined as $\eta = -ln\ \tan(\theta/2)$. The distance ΔR is defined in $\eta - \varphi$ space as $\Delta R = \sqrt{\Delta\eta^2 + \Delta\varphi^2}$.

2.2. Plastic scintillators in the Tile Calorimeter

The Tile Calorimeter [7] (TileCal) is the hadronic calorimeter of ATLAS [5]. It is a sampling calorimeter, using steel as the absorber medium and scintillator tiles as the active medium. It is responsible for measuring the energy and tracks of hadrons, taus and jets and was designed to contain all hadronic showers developing from the p-p collisions. It also contributes to the reconstruction of missing transverse energy. A zoomed view into the Calorimeter region of the ATLAS detector is shown Figure 2-3.

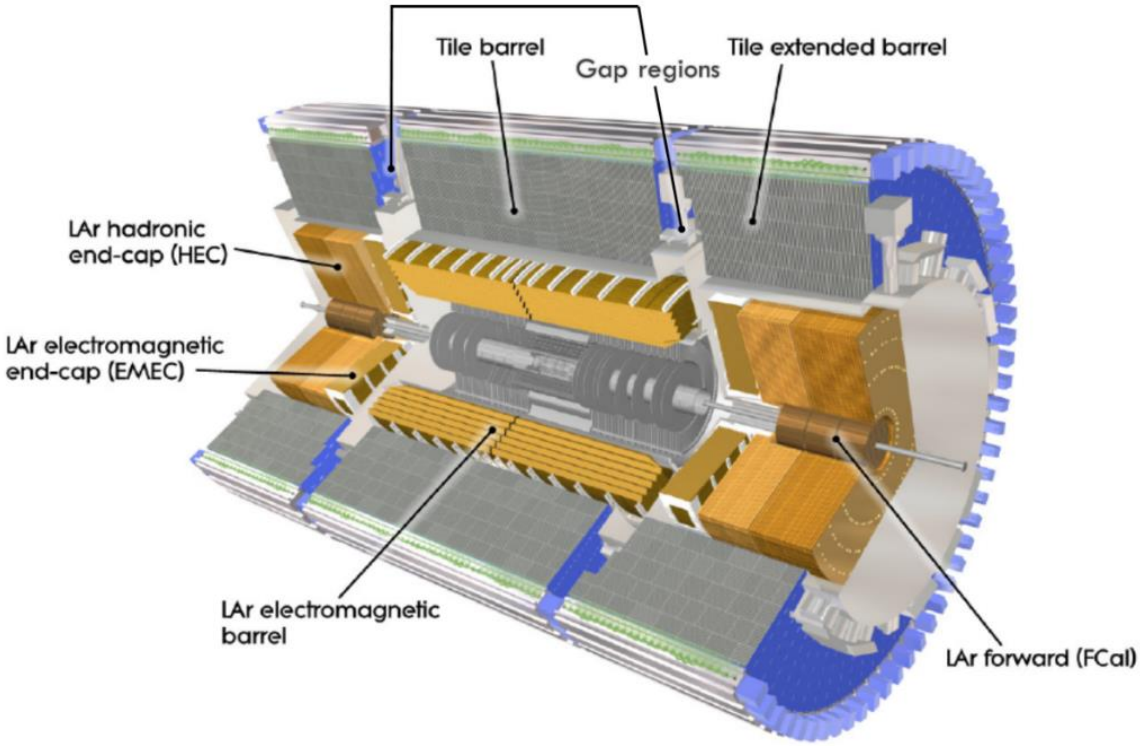


Figure 2-3: Diagram depicting the ATLAS calorimeter regions.

2.2.1. The Barrel regions

The TileCal consists of a central long barrel (LB) flanked on either side by extended barrels (EB). Each barrel consists of 64 modules stacked azimuthally, resulting in a cylindrical structure of inner radius 2.23 m and outer radius 4.23 m. The LB modules cover the region $0 < |\eta| < 0.8$, whilst the EB modules cover the region $0.8 < |\eta| < 1.7$.

Each module consists of a matrix of 3 mm thick scintillator tiles sandwiched between 4 mm thick steel plates arranged perpendicular to the beam pipe. The scintillator tiles are arranged in 11 rows and vary in size.

As a high energy hadron passes through the tile modules, it interacts with the atomic nuclei of the steel absorber, to produce a shower of lower energy particles. These interact with the scintillator tiles which absorb energy from the incoming particles and fluoresce to emit light.

The scintillation light is collected by wavelength shifting (WLS) optical fibers coupled along two of the exposed tile edges. Currently, Y11 fibers obtained from Kuraray are employed. The fibers are arranged in plastic profiles to ensure contact with individual tiles.

Tiles are grouped into readout cells and the fibers of these are bundled together in Lucite tubes. The cells are segmented into three longitudinal layers, (A, BC and D) which are approximately 1.4, 4.0 and 1.8 interaction lengths thick respectively at $\eta = 0$. The cells are numbered according to the pseudorapidity range that it covers, with A and BC cells numbered in pseudorapidity intervals of 0.1 and D cells in intervals of 0.2 [8]. The cell segmentation for the LB and EB modules is shown in Figure 2-5.

An LB module contains 337 scintillator tiles per row, leading to a total of 3377 tiles. An EB module contains 1591 scintillating tiles. The fiber bundles are coupled to photomultiplier tubes (PMT), and light detected by the PMT's generate a signal. Tiles are wrapped in Tyvek paper and fibers are aluminized on the ends which are not coupled to the PMT's, in order to maximise the amount of light collected.

Each cell is read out by two PMT's, which detect the light from each side of the module. This is done for redundancy and to ensure special uniformity. The signal generated by the PMT's is then processed with readout electronics housed in the same steel girder as the PMT's. These then digitize the data which can be analysed thereafter [9]. Figure 2-4 shows a schematic of a TileCal barrel module.

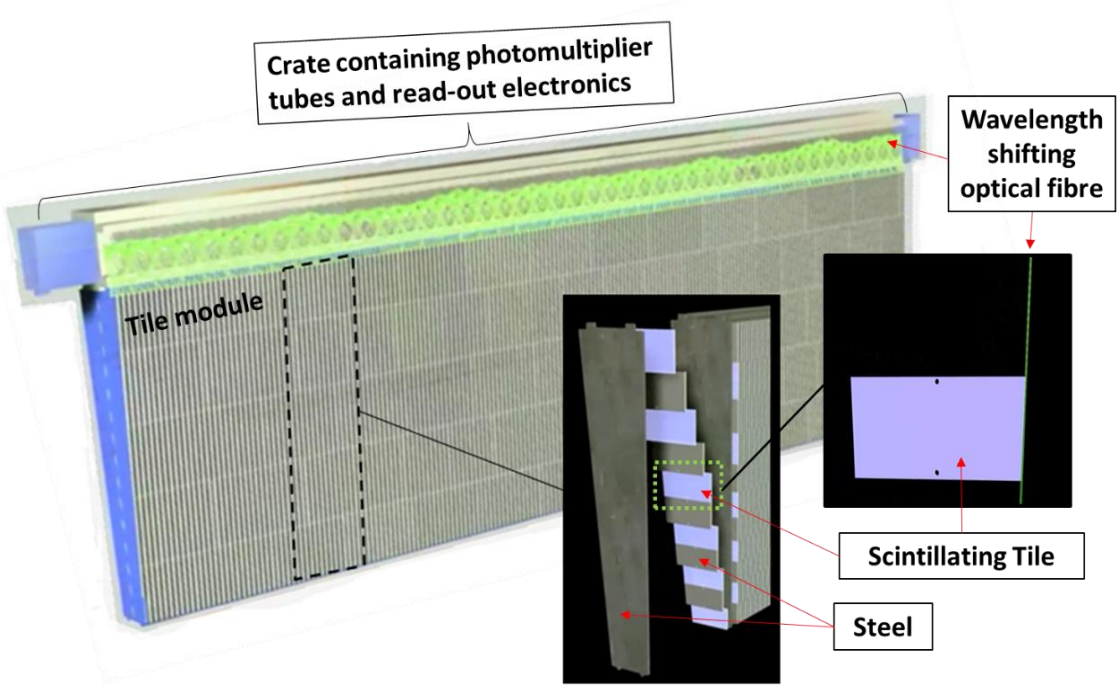


Figure 2-4: Representation of a Tile Module and its various components

2.2.2. The Gap regions

In the region between the central and extended Tile barrels, there is a 68 cm thick gap which contains the services to the inner detector systems, the read-out electronics crates and the Liquid Argon (LAr) cryostat flange. These result in a build-up of "dead material" within the detector where the reconstructed energy signal may be lost.

In order to correct for this energy loss across the gap, the Intermediate Tile Calorimeter (ITC) detector is employed which uses additional plastic scintillator plates to sample the energy across the gap. The scintillators are coupled to WLS fibers and are encased in aluminium cans. The fibers then lead to PMT's and the signal is digitized using the same read-out electronics as those used in the Tile barrels.

The scintillators of the ITC are referred to as the Gap scintillators (E1 and E2) and the Cryostat scintillators (E3 and E4). The Gap scintillators are located between the central and extended Tile Barrels, covering the η region from 1.0 to 1.2, and are used to correct the hadronic energy response. The Cryostat, or Crack,

scintillators are located between the central and endcap electromagnetic calorimeter cryostats, covering the η region from 1.2 to 1.6, and are used for correcting the electromagnetic energy response. [10]

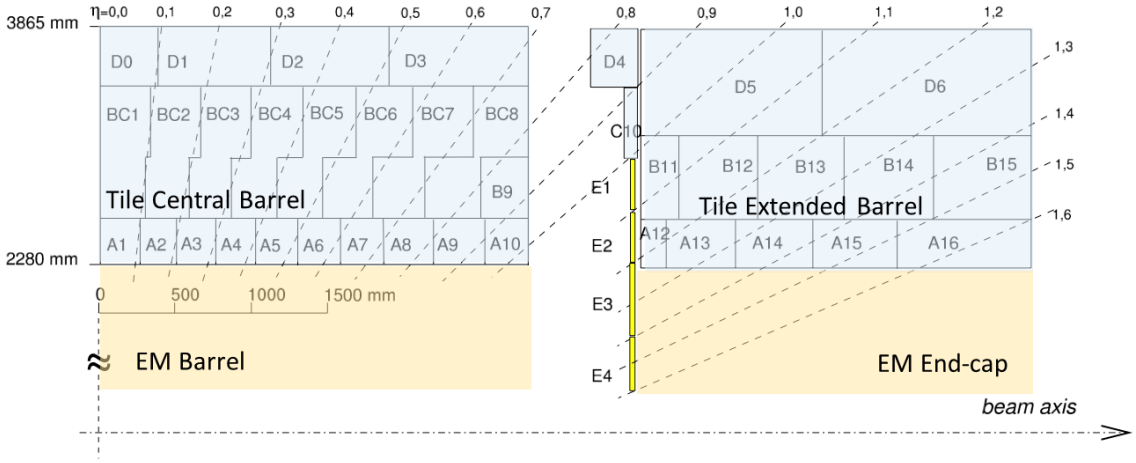


Figure 2-5: Layout of the ITC scintillators relative to the cells of the Tile Calorimeter barrels

In addition to the Tile Calorimeter and the ITC, the Minimum Bias Trigger system also employs plastic scintillators. The Minimum Bias Trigger Scintillators (MBTS) are located within the Gap, at a smaller radius from the beam pipe, near the inner pixel detector. They cover the η region from 2.09 to 3.84. These scintillators form part of the first level hardware trigger system and provide a trigger signal for when to record events which have potential for physics of interest. [9] The photograph in Figure 2-6 shows the radial distribution of the MBTS and cryostat scintillators in the Gap region.

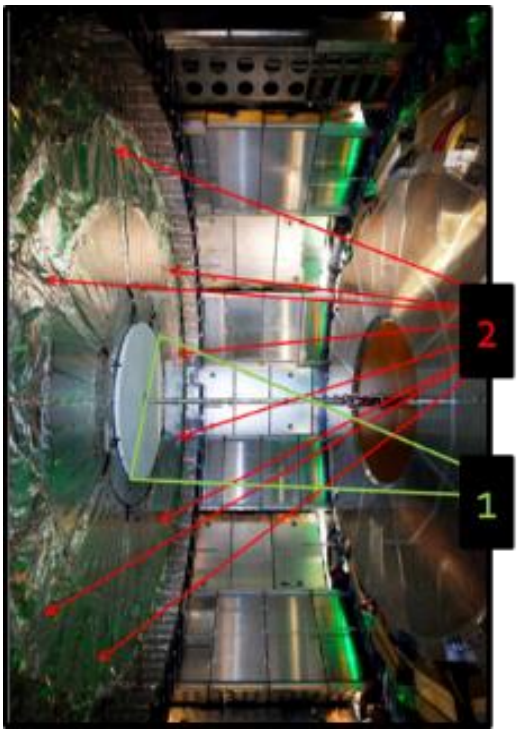


Figure 2-6: Photograph of the Gap region. The MBTS are indicated by 1 and the cryostat scintillators are indicated by 2.

2.3. The radiation environment of plastic scintillators in the Tile Calorimeter of the ATLAS detector

Prior to Run 1 of LHC data taking, several studies were conducted in order to estimate the impact of the predicted radiation environment on the performance of the detector. GCALOR [11] and FLUKA [12] simulations predicted that the radiation levels in the Gap region would be greater than those in the barrel regions, with the MBTS scintillators being exposed to the most radiation. The predicted radiation map of the total ionising dose accumulated over a year in the calorimeter region at $\sqrt{s} = 14$ TeV and nominal luminosity of 10^{34} $cm^{-2}s^{-1}$ is shown in Figure 2-7 [13]. The dose is calculated in units of Gray (Gy), which is defined as 1 Joule of radiation energy absorbed per 1 kilogram of matter.

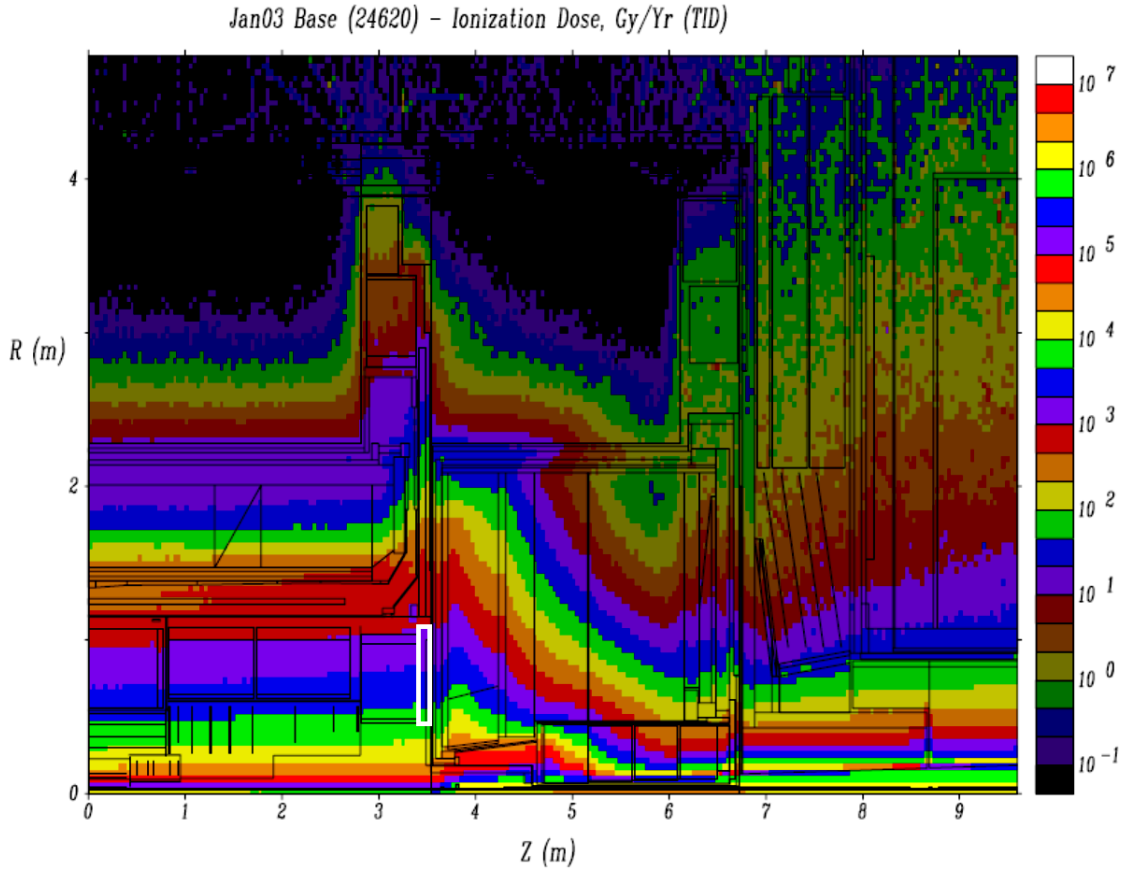


Figure 2-7: Radiation map of the total ionising dose accumulated over a year in the calorimeter region at √s=14 TeV and nominal luminosity of 10^{34} $cm^{-2}s^{-1}$

The position of the MBTS scintillators is outlined in white, whilst the cryostat and gap scintillators are positioned at larger radial values, R, along the Gap region. For the scintillators in the Tile Barrels, it was predicted that the worst light losses after 10 years of LHC operation would be approximately 5% in the region closest to the beam pipe [13].

After Run 1, with $\sqrt{s}$ reaching a maximum of 7 TeV, the estimated dose that the MBTS scintillators received was between $0.1{\sim}0.4 \times 10^4$ Gy [14]. At a dose in the range of 10^4 Gy, a loss of 50% in light transmission of the scintillator plus fiber system was anticipated [14]. A small fraction of yellow discolouration was observed in these scintillators

3 Scintillation and Plastic Scintillators

In order to understand how scintillators undergo radiation damage and how this in turn affects their performance, it is important to understand the fundamental mechanism behind scintillation. This Chapter focuses on explaining how scintillation occurs and how radiation affects the scintillation mechanism. The scintillators being investigated are then described.

3.1. The scintillation mechanism

Plastic scintillators primarily consist of organic fluors suspended in a polymer base. The polymer base that is employed generally contains some form of aromatic ring structure which gives rise to a delocalized π-electron structure within the molecule. When ionizing radiation impinges the scintillator, part of its energy may be absorbed by these delocalized π-electrons, resulting in molecular excitations. The absorption is typically exhibited in the visible and ultra-violet regions corresponding to excitation of the singlet π-electron state. The energy level diagram of a π-electron is shown in Figure 3-1. [1]

An excited π-electron may return to its ground state through several types of deactivation processes, with the preferred process being that which results in the shortest lifetime of the excited state. For excitations to higher states (S_2, S_3 or T_2, T_3), these de-excite to lower states of the same multiplicity (S_1 or T_1) by means of internal conversion within a short time span of the order of picoseconds.

This usually occurs when the energy levels of two excited states are close enough that their respective vibrational modes may overlap. Excitations which have additional vibrational energy, for example the S_{11}-S_{13} states, can also lose energy through vibrational relaxation, whereby heat is dissipated and thermal equilibrium is reached in the molecule. Both internal conversion and vibrational relaxation are non-radiative processes.

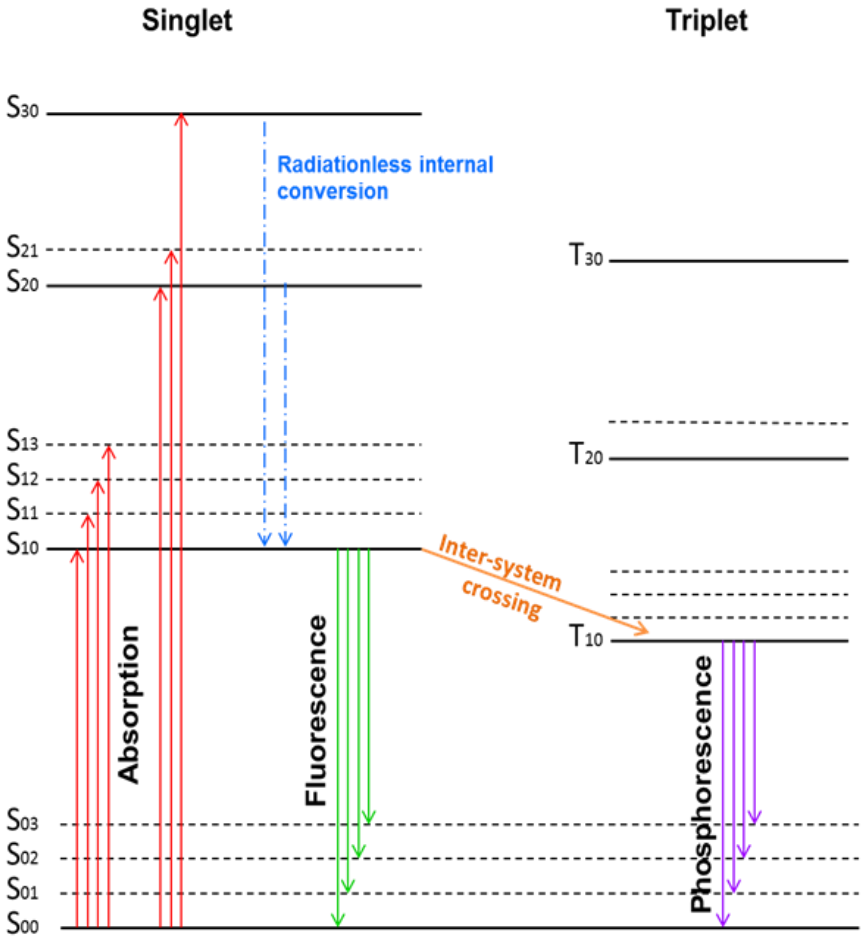


Figure 3-1: Energy level diagram of an organic molecule with π-electron structure, adapted from [1].

The fluorescence process occurs for transitions from the lowest vibrational first excited state (S_{10}) to the ground state, where energy is emitted as a photon of a characteristic wavelength. This process forms the primary mechanism for scintillation in organic plastic scintillators. Fluorescence occurs within a matter of nanoseconds which gives plastic scintillators their fast response capability.

Sometimes, transitions called inter-system crossing can occur whereby excited singlet states are converted to triplet states. The lifetime of the T_{10} triplet state is longer than that of the S_{10} state and so the de-excitation to the ground state from the triplet state takes longer. As a result, a delayed light emission called phosphorescence occurs. The wavelength of the light emitted in phosphorescence is longer than that of light emitted by fluorescence.

A final energy loss mechanism that may occur is the process of delayed fluorescence. In this process, molecules in the triplet state may undergo thermal excitation and excite back into the singlet state before undergoing fluorescence to the ground state. [1] Phosphorescence and delayed fluorescence are considers as quenchers of fluorescent light since these three radiative processes can compete with each other.

The energy of fluorescent light is generally less than the energy required for absorption because the fluorescence transition can occur to any of the ground state's vibrational levels and because absorption causes a change to the equilibrium internuclear potential [15]. However, a small amount of overlap may occur between the absorption and emission wavelength ranges resulting in re-absorption of scintillation light. Typical plastic scintillator bases have a very low fluorescent yield and therefore aren't very transparent to their own scintillation light.

Primary fluor dopants are thus added in small concentrations (typically < 3% by weight). Primary fluors are chosen such that their absorption spectra match the emission spectra of the base and generally contain a high quantum yield of the energy transfer transition. Light can be transferred between base and fluor via either radiative re-absorption, or by a non-radiative coulombic interaction called Forster resonance energy transfer. [15]

Forster energy transfer is limited by the distance between the interacting states and is therefore more likely to occur with increasing fluor concentrations until a saturation is reached. Light is then emitted by the fluors at higher wavelengths, generally in the UV range of 340-360 nm.

Since this wavelength is still below the peak efficiency of common photomultipliers, a secondary fluor is added at concentrations of < 0.1% by weight. The secondary fluor acts as a wavelength shifter and prevents re-absorption of scintillation light by the primary fluor. It also helps to increase the bulk attenuation length of the emitted light. Energy transfer between the primary and secondary fluors occurs via radiative exchange [15]. A schematic of the

radiative transfer of energy from polymer base to the primary fluor and secondary fluor is shown in Figure 3-2.

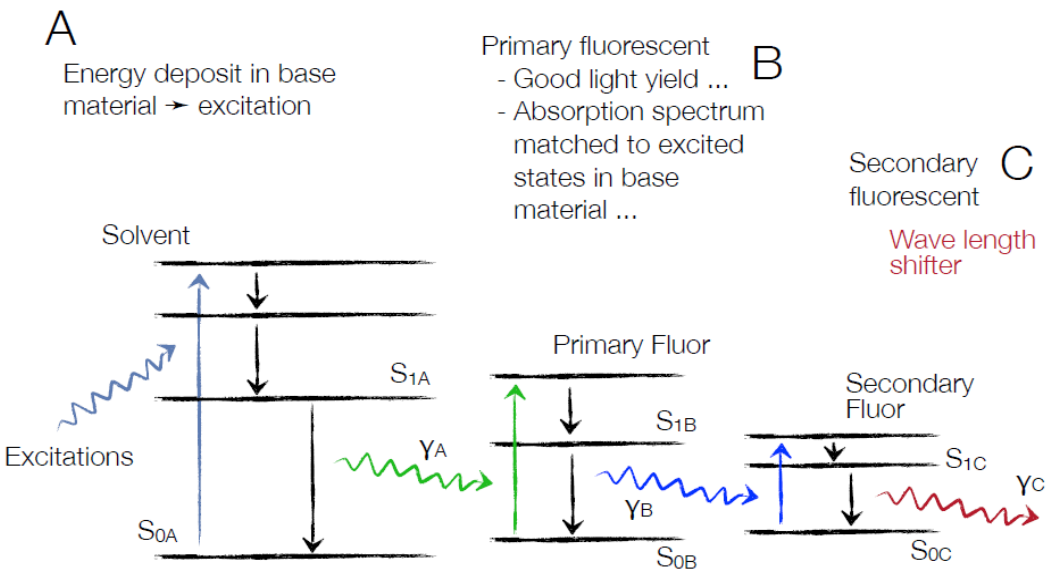


Figure 3-2: Radiative transfer of energy between polymer base, primary and secondary fluors adapted from [16].

3.2. Radiation damage in plastic scintillators

Whilst plastic scintillators provide an efficient way to detect ionizing particles, it is this same interaction that causes its subsequent damage. When ionizing particles pass through the scintillator medium, they leave behind them a wake of excited particles, some of which undergo fluorescence to emit light. At high incident doses however, this radiation may also break chemical bonds therefore modifying the polymer properties.

The damage process is complicated and can be influenced by a number of factors including the rate of irradiation, the amount of dose absorbed, and the nature of the impinging particle (particularly its stopping power), as well as the environment under which the radiation occurs [17] [18] [19]. Structural properties of the plastic polymer can also influence the extent to which the damage occurs.

The biggest effect of radiation damage is that it alters the optical properties of the scintillator. This can manifest in two ways, either a decrease in actual scintillation light output due to damage to the fluorescent component, or through a degradation in its transmission character as a result of the formation of optical absorption centres. The change in transmission character further affects the light attenuation length of the scintillator. [15]

Primary and secondary fluor dopants are in general relatively radiation hard. It is therefore believed that majority of the radiation damage arises in the polymer base. This was demonstrated in studies performed on an organic doped liquid scintillator (BC505), after exposure to 5 Mrad (50 kGy) of irradiation from a 600 Ci ^{60}Co gamma source [20].

In these studies, large losses were observed in the intrinsic scintillation output in response to a radioactive source despite the fairly small transmission losses seen. Upon investigation of the un-doped liquid base, a transparency loss was observed to occur, indicating the formation of an absorptive front which tails off at higher wavelengths. The relevant spectra of this study are shown in Figure 3-3.

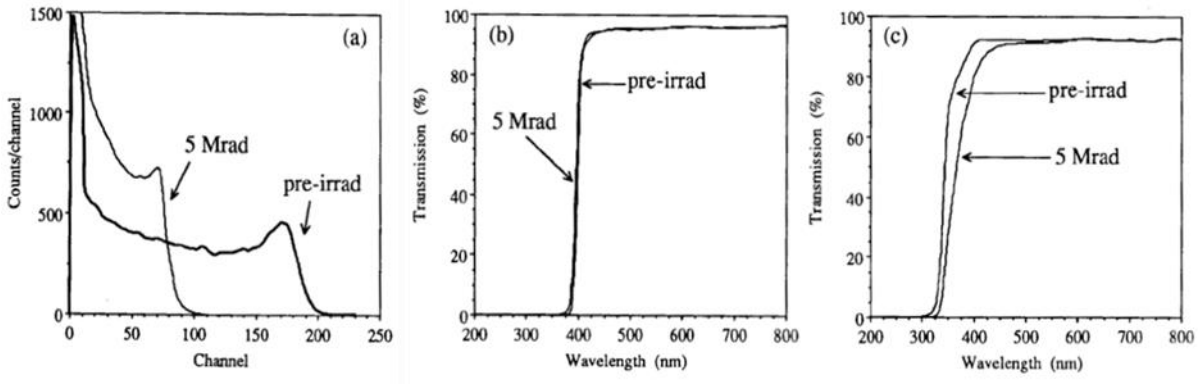


Figure 3-3: (a) Pulse height spectra for BC505 samples before and after the 5 Mrad irradiation. (b) The transmission spectra for the BC505 sample. (c) The transmission spectra for the undoped base of BC505 before and after the 5 Mrad irradiation. Obtained from [20].

When this additional absorptive component extends to the wavelength region where radiative transfer between fluors occurs, this forms a competitive process to the regular light shifting mechanism and hence reduces the intrinsic light output of the scintillator. Furthermore, if the induced absorption extends to even

higher wavelengths, it can greatly reduce the attenuation length and cause additional losses in bulk samples.

The formation of new absorptive centres, is proportional to the absorbed dose and can be related to degradation of the polymer base. A study was conducted by Torrisi [17] that investigated the types of species desorbed by the polymer polyvinyl toluene (~200 μm thick) during proton bombardment. This was assessed using "in situ" mass quadrupole spectroscopy. It was found that C-H bond breaking, hydrogen degassing and free radical formation occurred for high stopping power irradiations. In these studies, both free radical formation as well as their recombination occurred at a rapid rate, with a diffusion of recombined species being observed towards the polymer surface.

It should be noted that plastic scintillators show a discolouration along with damage. For blue emitting scintillators, this is typically observed as a yellowing, increasing with absorbed dose until subsequent browning ensues. Orange and green discolouration have also been observed in some scintillators [15]. These discolouration's can be linked to free radical production or to trapped electrons and conjugated double bonds [18]. Free radicals in particular absorb light and therefore cause a reduction to the amount of scintillation light emitted.

A fraction of the radiation induced absorption is recoverable and this 'healing' of damage may be accelerated by exposure to oxygen or heating under vacuum. Free radicals react with oxygen to produce peroxide radicals which generally do not absorb visible light and therefore result in bleaching [18].

If irradiation occurs under oxygen exposure, this influences the amount of damage undergone by the scintillator and the rate of oxygen diffusion into the sample has been shown to play a role in dose rate dependant effects. If oxygen is absent, 'healing' can still occur when radicals interact with hydrogen or when two radicals annihilate. These second order processes can occur via cross-linking, disproportionation or recombination and therefore modify the polymer structure [19].

3.3. Description of plastic scintillators under study

Four commercial plastic scintillators (EJ200, EJ208, EJ260 and BC408) and two types employed by the ATLAS detector (UPS923A and TileCal) were investigated. The plastics are composed of either a polyvinyl toluene (PVT) or polystyrene (PS) base. Polyvinyl toluene consists of long chains of vinyl toluene molecules which comprise of a benzene ring bonded to a methyl group (CH_3) and a vinyl group (CH_2-CH-).

Polystyrene consists of long chains of styrene monomers. Styrene is very similar to vinyl toluene except that it does not contain a methyl group. In both polymers, the benzene ring gives rise to the delocalized π-electrons. All the scintillators investigated were blue emitting, with the exception of EJ260 which emits light in the green wavelength region. Details on their composition and properties are listed in the Table 3-1.

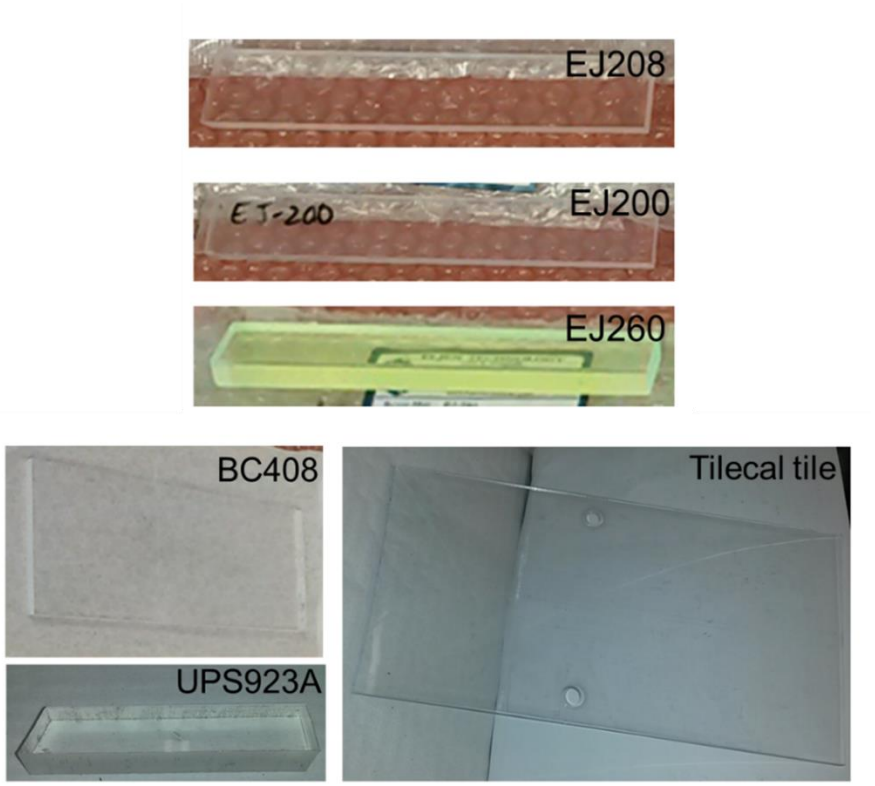


Figure 3-4: Photographs of plastic scintillators under study

Table 3-1: Table summarising the various properties of the scintillators under study.

Scintillator	EJ200	EJ208	EJ260	BC408	UPS923A	Protvino
Manufactured by:	Eljen Technology	Eljen Technology	Eljen Technology	Saint Gobain Crystals	Institute of Scintillating Materials, Kharkiv. (Used in MBTS)	Institute of High Energy Physics (IHEP), Protvino in association with SIA luch, Podolsk. (Used in Tile Barrel)
Base	PVT	PVT	PVT	PVT	PS	PS
Primary Fluor	0.3% organic fluors	0.3% organic fluors	0.3% organic fluors	Not available (However, listed as a performance equivalent of EJ200)	2% PTP	1.5% PTP
Secondary Fluor					0.03% POPOP	0.044% POPOP
Light Output, % Anthracene	64	60	60	64	60	Not available
Wavelength of Max. Emission, nm	425	435	490	425	425	
Rise Time, ns	0,9	1	~	0,9	0,9	
Decay Time, ns	2,1	3,3	9,2	2,1	3,3	
Density, g/cc:	1,023	1,023	1,023	1,032	1,06	
Refractive Index	1,58	1,58	1,58	1,58	1,6	
Light attenuation length (cm)	~400*	~400*	~400*	380**	400	
Source	[21]			[22]	[23]	[24]

*In a cast sheet of dimensions 2 cm x 20 cm x 300 cm

**In a cast sheet of dimensions 1 cm x 20 cm x 200 cm

The Protvino type plastic scintillators were manufactured specifically for the Tile Calorimeter using an injection molding technique. The design of the scintillator was specifically geared towards cutting cost of manufacture since these scintillators were to be used in the barrels and would require a large quantity of material. In comparison to a similar Bicron RH4 cast scintillator, the Protvino scintillator yielded ~2.5 times less light in response to ~3 MeV minimum ionizing beta particles from a Ru^{106} source [25].

Studies were also conducted by the Institute of High Energy Physics (IHEP) team, into the effect of changing concentration of the fluors. For an increase in PTP concentration from 0.1% to 0.2%, the light output increased by 10%, whilst an increase in concentration of POPOP from 0.02% to 0.1% had little effect on light yield [24]. Since UPS923A scintillators are very similar in composition to the Protvino type, with the exception of different concentrations of fluors, we can assume that they are the better performing of the two in terms of light response. UPS923A is marketed by the manufacturer as being a good general purpose scintillator with good transparency.

EJ200 and BC408 are recommended by their respective manufacturers, for use in time of flight systems which require large area coverage due to their short rise and decay times. They also have the highest light output from the 6 scintillators investigated.

EJ208 has a longer emission wavelength than EJ200, and is ideal for systems in which uniformity of light collection is of utmost importance, whilst timing takes a secondary priority. In addition, EJ208 is predicted to offer greater tolerance against radiation damage since damage results in the increased optical attenuation of light at shorter wavelengths.

EJ260 has the longest emission wavelength and shifts light to the green spectrum. It is therefore proposed to offer greater radiation tolerance than conventional blue emitting plastic scintillators and can still be coupled to common blue sensitive phototubes.

4 Experimental details

4.1. Overview of radiation damage methods

The 6 MV EN Tandem accelerator of iThemba LABS in Gauteng was used to irradiate samples with 6 MeV protons. To ensure that the study simulated a similar type of particle-scintillator interaction as observed in the Tile Calorimeter, protons were required to pass through the samples whilst imparting energy primarily through electronic energy loss due to electronic excitation and ionisation interactions.

The stopping range of 6 MeV protons and their energy deposited within the scintillator material was determined using the SRIM software package. Samples were then prepared using a cutting and polishing procedure based on standard metallographic techniques. Samples were irradiated with doses of approximately 0.8 MGy, 8 MGy, 25 MGy and 80 MGy and their damage analysed using several techniques.

4.1.1. SRIM simulations

SRIM (the Stopping and Range of Ions in Matter) [26], is a program that simulates the interaction of ions in matter. It takes into account the screened Coulomb collision between ions and target atoms as well as the exchange and correlation interactions between the overlapping electron shells, in order to calculate the stopping and range of ions into matter.

SRIM contains an additional program called TRIM (the Transport of Ions in Matter) which is a Monte-Carlo program that calculates the interaction of ions within a target. It establishes the collision details between ions and target atoms by inputting a random number for the impact parameter and distance to the next colliding atom to create a probability distribution that is dependent on the target density [26].

For these simulations, preset PVT and PS based scintillator materials from the SRIM database were used and adjusted to accommodate for the Carbon to Hydrogen (CH) ratio and density of the plastics as indicated by the manufacturer. The following figure shows the TRIM simulation for 6 MeV protons (hydrogen ions) through a PVT based target.

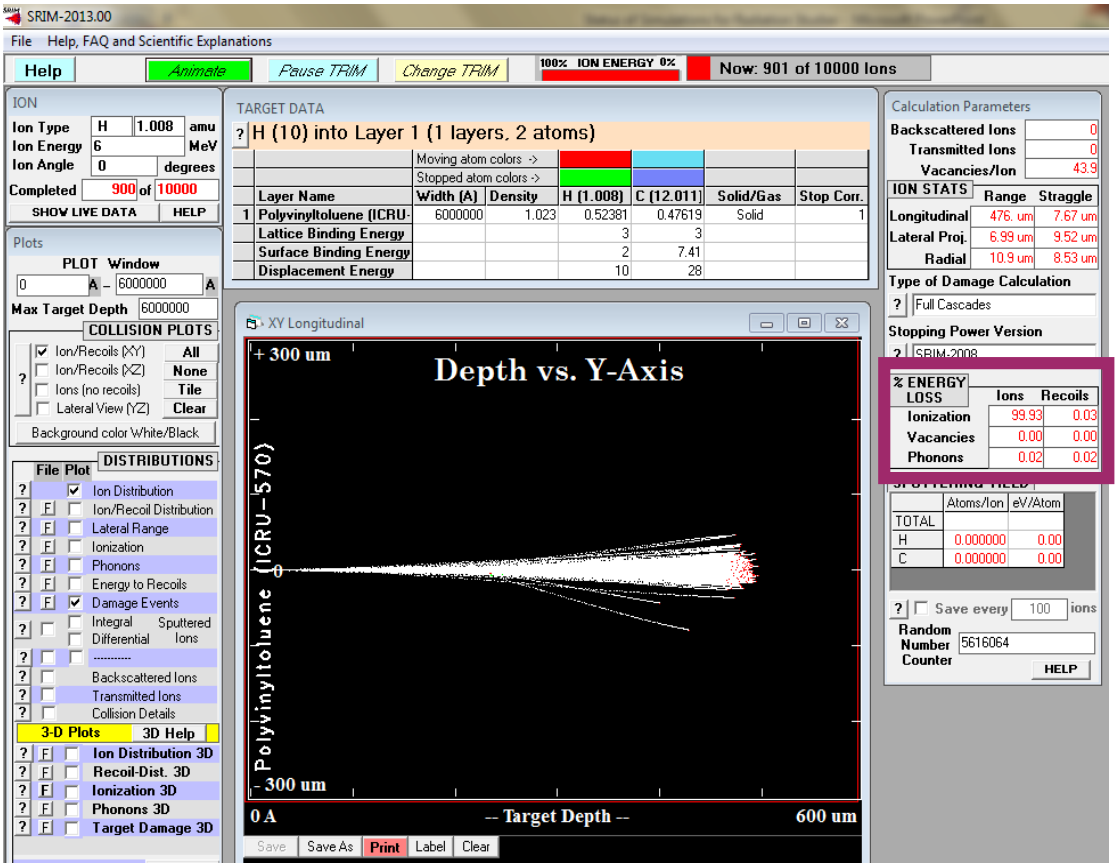


Figure 4-1: TRIM simulation of 6 MeV protons in PVT target.

As highlighted in the purple box, about 99.93% of the energy loss is due to ionization imparted by the protons. Figure 4-2 shows the range of the ions over the PVT based and the PS based target. Most of the ions stop at around 476 µm in PVT and 466 µm in PS. Due to the requirement that protons pass through the samples and not stop within them, a thickness of ~350 µm was decided. This range is well before any stopping begins to occur in both sample base types. Thicknesses of less than 250 µm were ruled out as the machining of such samples induced stress related structural damage to them.

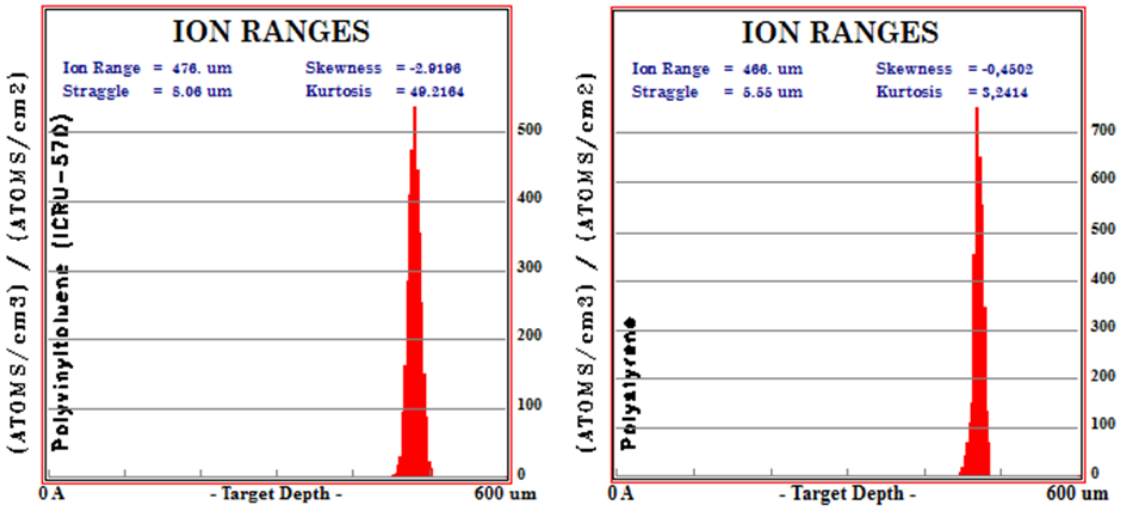


Figure 4-2: Plot of the range over which protons stop within the PVT and PS targets.

Simulations of 6 MeV protons through targets of 300-400 µm thickness were then conducted in order to establish the energy of particles transmitted from the target. This was used in order to estimate the amount of energy deposited by a 6 MeV proton traversing the samples, which was a parameter needed for estimating the absorbed dose upon irradiation of the samples. For a 6 MeV proton traversing through a PVT based scintillator, the estimated amount of energy deposited is 3.20 MeV through a 350 µm thick sample and 3.89 MeV through a 400 µm thick sample.

4.1.2. Sample preparation

Samples were prepared with targeted dimensions of 5 mm x 5 mm area and 350 µm thickness. Since cutting the samples caused them to become rough and opaque, samples were polished to improve their transparency. A polishing procedure based on standard metallographic techniques [27] was employed.

A “Buehler IsoMet” low speed cut-off machine was used to section rectangular bars of 5 mm x 5 mm area and with varying lengths. The lengths depended on the dimensions of the sample blocks provided by the manufacturers. The bars were further cut along their cross-section into 1 mm thick slices.

The cutting operation was carried out using a diamond finished blade with cutting fluid as a lubricant. Photographs of the Buehler IsoMet cutting machine are shown in Figure 4-3.

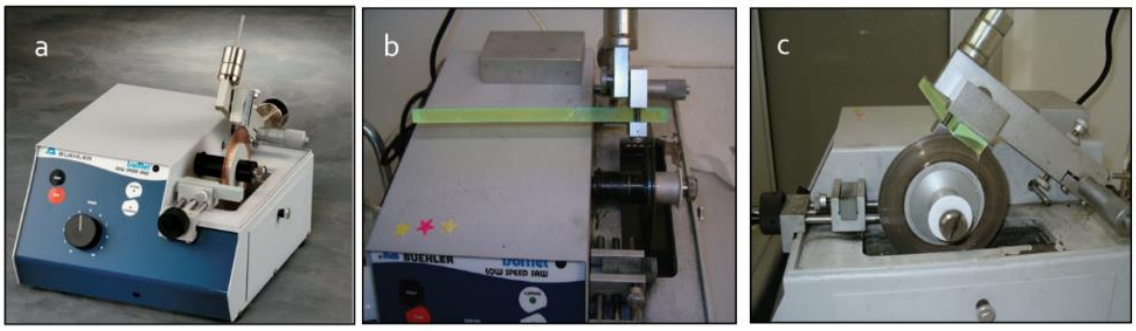


Figure 4-3: Photographs of (a) the Buehler IsoMet cutting machine, (b) a front view of an EJ260 bar being cut, (c) a side view of the EJ260 bar being cut.

The sample slices were then mounted within the 6 mm x 6 mm x 0.36 mm grove machined into aluminium sample holders. The holders were designed to be attached to the polishing machine. Several photographs of the aluminium holder are shown in Figure 4-4.

Carbon tape was chosen as the mounting medium because it did not attack the plastic scintillators like other typical mounting agents would and provided a firm enough hold during polishing. Furthermore, removing the carbon tape entailed soaking in an ultrasonic bath of ethanol as opposed to using a harsher alcohol solvent which could damage the plastic material chemically.



Figure 4-4: Aluminium holders used to mount the samples onto before polishing.

The sample polishing was performed using a “Struers” metallographic polishing machine. Samples were mounted onto a rotating polishing head, and a polishing cloth was attached onto the spinning polishing wheel. A 2 Newton force pushed down on the samples as they rotated along the polishing cloth using a complimentary polishing direction.

The setup is indicated in Figure 4-5. Two polishing stages, medium and fine polishing were employed. The medium polishing stage was carried out using a 6 µm diamond suspension on a “Struers MD-Dac” polishing cloth, which is a satin woven acetate cloth. The fine polishing was carried out using a 1 µm diamond suspension on a soft synthetic fibre cloth (Struers MD-Nap).

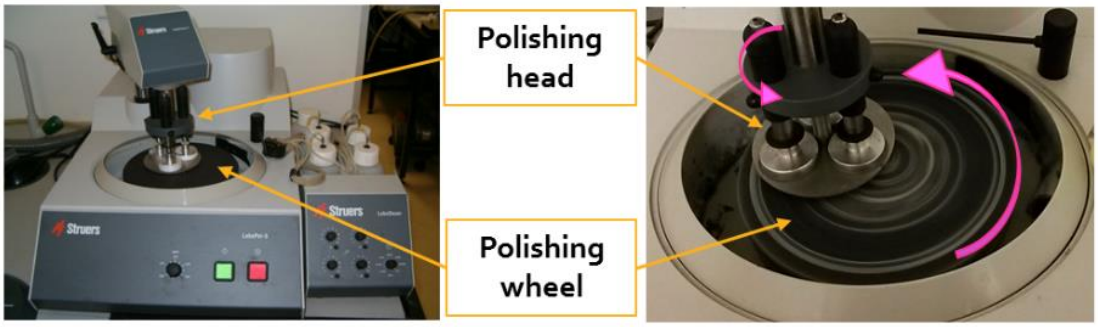


Figure 4-5: Photographs of the Struers polishing machine.

In the case of the Protvino samples, where a tile of 3 mm thickness was obtained from the Tile Calorimeter, 5 x 5 mm^2 squares were cut directly from the tile and rough polished down to 1 mm thicknesses before undergoing the medium and fine polishing stages.

All samples were polished on their transverse surfaces. After polishing, samples were soaked in the ultrasonic bath of ethanol for 30 minutes in order to remove the carbon tape and cleaned using lukewarm soapy water. Samples were then placed in brass holders in preparation for irradiation. In Figure 4-6, a final polished sample is shown being mounted into a brass holder. The transparency of the scintillator should be noted.



Figure 4-6: The final product of a polished sample, and a sample mounted into the brass holder.

4.1.3. Proton irradiation at iThemba LABS Gauteng

Plastic scintillator samples were irradiated using 6 MeV protons accelerated by the 6 MV EM Tandem accelerator of iThemba LABS. A schematic of the tandem accelerator is shown in Figure 4-7 below.

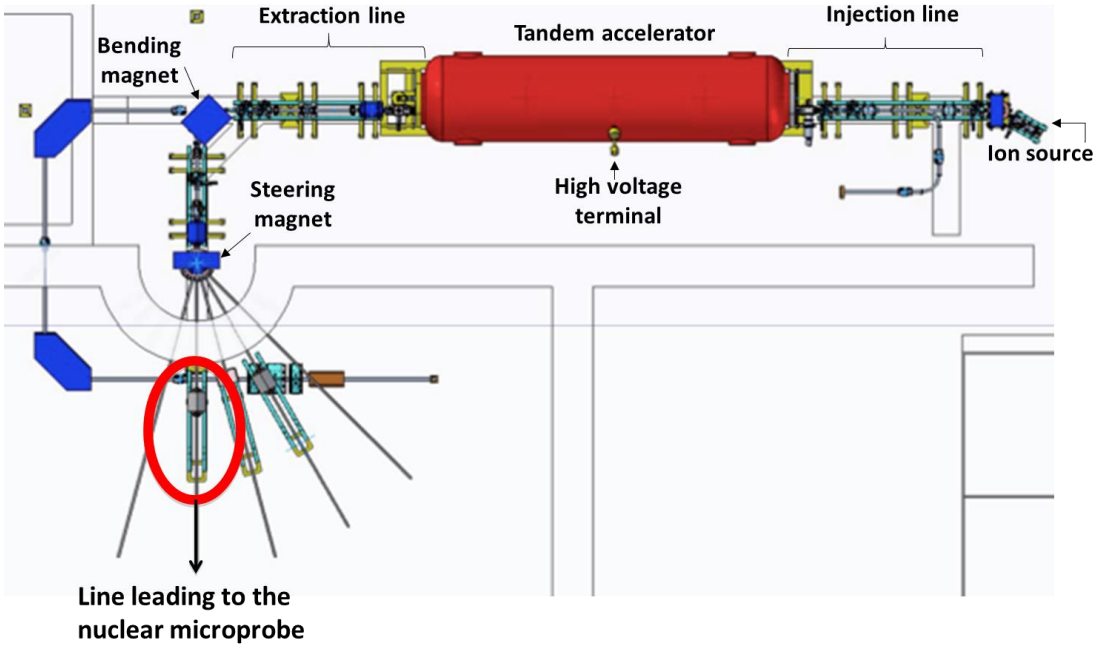


Figure 4-7: Schematic representation of the tandem accelerator at iThemba LABS.

In order to produce a beam of 6 MeV protons, the following procedure occurs. First, negative hydrogen ions are produced through Cesium sputtering by an 860A SNICS ion source and injected into the tandem accelerator. A voltage of 3 MV is applied to the central high voltage terminal whilst the entrance and exit ends of the tank are kept grounded.

A Pelletron charging system creates a potential difference, resulting in the negative ions being accelerated toward the terminal where they reach an energy of ~3 MeV. At the terminal, a gas stripping system removes the electrons from the ions.

A second Pelletron chain then creates a potential difference between the terminal and exit end, resulting in the now positive ions (protons) being further accelerated to reach ~6 MeV before being extracted from the tank. Bending and steering magnets then direct the extracted beam towards the nuclear microprobe. A photograph of the line leading to the microprobe is shown in Figure 4-8.

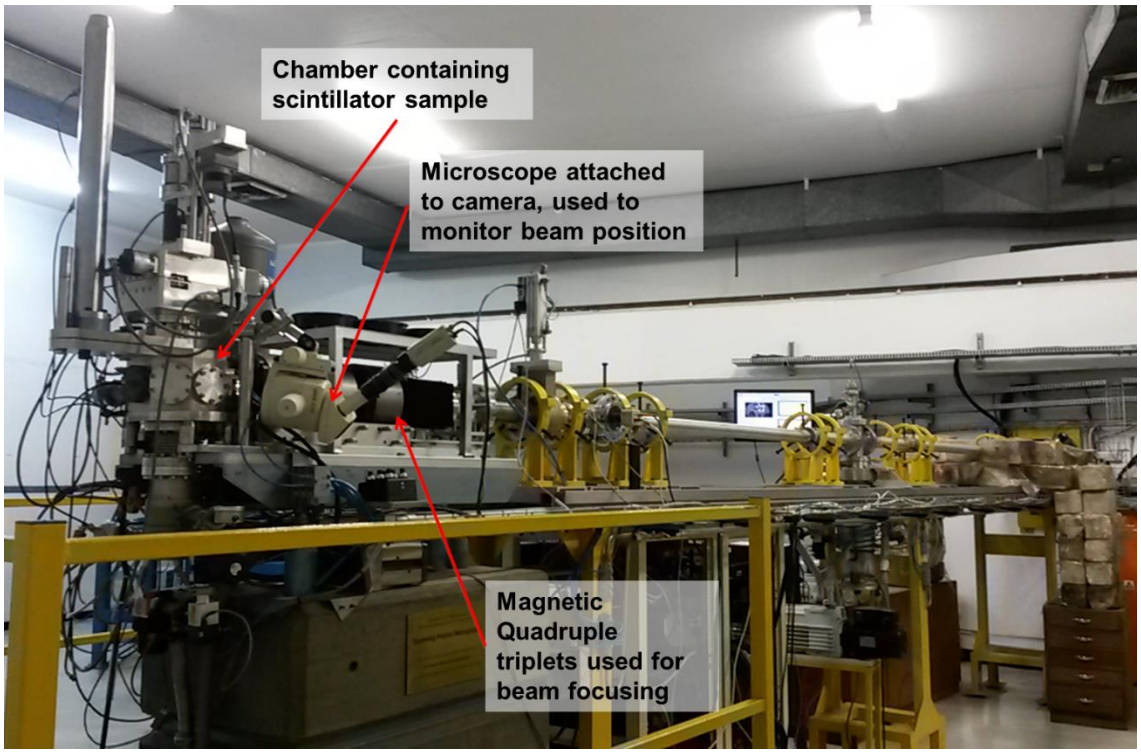


Figure 4-8: Photograph of proton beam line leading to the nuclear microprobe chamber.

For the irradiations, plastic scintillator samples were mounted on a hexagonal carousal sample holder and housed within the nuclear microprobe chamber under vacuum conditions. The proton beam was passed through an object slit and collimator slit and a set of magnetic quadrupole triplets were used to focus the beam onto a sample with a spot size of ~20-30 μm.

The beam was scanned in the x and y plane using a raster pattern to achieve a uniformly irradiated area of approximately 1.8 mm by 1.8 mm. This irradiation technique was required because using a large diameter beam which is not scanned over the sample resulted in an inhomogeneous intensity distribution of a Gaussian shape which was not conducive to the required damage analysis techniques.

The beam current was determined by measuring the current generated across a metal plate situated on the side opposite to the sample on the carousal. The beam current, integrated per second, was recorded for the duration of each irradiation. Two samples of each plastic scintillator type were irradiated per dose for targeted doses of 0.8 MGy, 8 MGy, 25 MGy and 80 MGy.

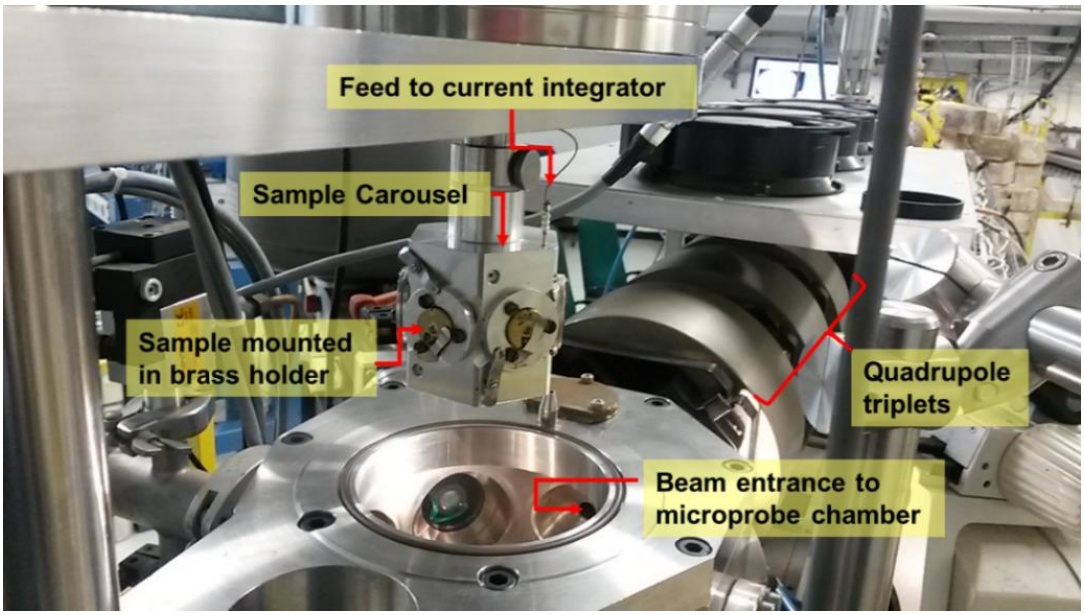


Figure 4-9: Photograph of sample carousel before being lowered into microprobe chamber

4.1.4. Calculation of dose

The radiation dose received by each scintillator was calculated using the relationship $R = \frac{N_p \times E_{loss}}{m}$. Here R is the absorbed dose in Grays, E_{loss} is the amount of energy lost per proton in units of Joules, N_p is the number of protons impinging the sample and m is the mass of the irradiated sample in units of kilograms.

The E_{loss} for each sample was determined using the SRIM simulations discussed previously. The mass was determined for the irradiated spot area (1.8 mm x 1.8 mm), using the densities given by the manufacturers and accounting for each sample's thickness.

The number of protons impinging the sample, was determined using the relationship $N_p = \frac{it}{q}$, where i is the current of the proton beam used, t is the total irradiation time and q is the charge of a proton. The total charge passed through each sample for their respective exposure times during irradiation was used for the calculations. Appendix B contains the tables summarising the beam conditions and calculated doses, as well as beam current distribution plots for all samples.

4.2. Overview of the techniques used to analyse damage

The effects of proton damage on the optical properties of the samples were characterised by conducting light transmission, light yield and fluorescence studies. Whilst the technique of Raman spectroscopy was used to investigate the structural damage undergone by the scintillators.

4.2.1. Light Transmission spectroscopy

Transmission spectroscopy was conducted using the Varian Carry 500 spectrophotometer. A photograph of the spectrophotometer is shown below. The spectrophotometer uses a lamp source and diffraction grating in order to produce a differential wavelength spectrum of light. A tungsten lamp source produces light over the visible spectrum, whilst a deuterium lamp source produces light across the ultra violet spectrum.

Light transmission measurements were conducted over the wavelength range of 300-800 nm. The spectrophotometer allows for a dual beam so that transmission

may be measured relative to a control sample. The transmission of each sample was measured relative to air.



Figure 4-10: Photograph of the Varian Cary 500 spectrophotometer.

Samples were tested prior to irradiation as well as on the day of irradiation, 1 day, 2 days, 1 week and 4 weeks after irradiation. Testing was done over several days after irradiation in order to observe healing of the transparency loss in the scintillators. Measurements were also made for a control sample for each grade on each respective day in order to correct for any day to day systematic fluctuations.

A baseline as well as zeroing calibration were performed on the machine prior to each days testing. Measurements were taken for four different mounting positions of the sample within the machine (2 per cross-sectional face) and the average spectra was processed for analysis thereafter. Samples were mounted behind a slide containing a 1 mm diameter hole through which light was incident, thereby ensuring that only the irradiated regions of each sample was measured.

4.2.2. Light yield testing in response to ^{90}Sr

The scintillator light yield in response to beta electrons emitted by a ^{90}Sr source (with average energies of 0.54 MeV and 2.28 MeV) was measured using the light

tight box set-up at CERN. In these experiments, two opposite edges of a sample were coupled to two Kuraray Y-11(200) optical fibers which were connected to a standard Tile Calorimeter photomultiplier tube. The fibers were of a 1 mm diameter and slotted into grooves in the sample holder in order to ensure more control over the contact made between the fibers and scintillator edges.

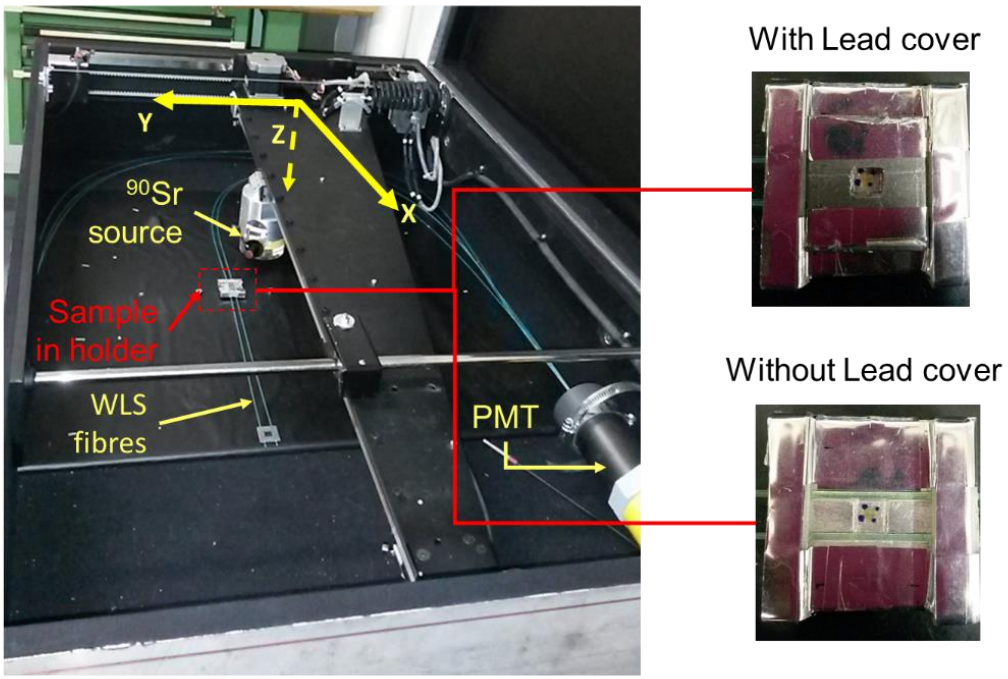


Figure 4-11: Set-up of the light box used to test the light yield.

The ^{90}Sr source was scanned over the sample in the X-Y direction whilst emitting its radiation in the Z direction. For each X-Y position of the source, a one second integrated signal registered by the PMT was recorded. A lead cover was used to ensure that only interaction with the sample regions were measured. Light yield experiments were conducted several weeks after irradiation thus providing time for partial recovery in the scintillators. Control samples and irradiated samples were tested, with three measurements made per sample.

4.2.3. Fluorescence spectroscopy

The light fluorescence of each plastic scintillator was measured using the LabRAM HR Raman spectrograph. A 229 nm laser with a power of ~3-5 mW was

employed to provide energy for molecular excitations to occur and thereby prompt light emission through luminescence. At this wavelength, the laser energy is sufficient to be absorbed by the PS or PVT base, and the successive light transfer from base to primary and secondary fluors can occur. This enables one to mimic the interaction of energetic particle showers with the plastic scintillators.

Photographs of the LabRAM HR are shown below. The laser is guided through a series of mirrors and optics in the machine, and is incident on the sample through the microscope aperture. As the sample fluoresces, the light emitted in the direction back up the aperture is collected by a detector and a differential wavelength spectrum is obtained.

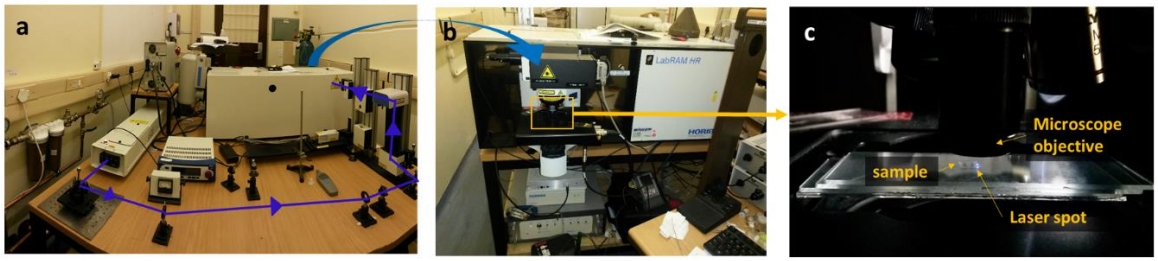


Figure 4-12: (a) Back view showing the path travelled by the laser into the LabRAM HR, (b) front view of the spectrograph, (c) zoomed view of the sample undergoing fluorescence.

The main obstacle to overcome during testing, was the effect of photo-bleaching of the fluorescent light. For excitation wavelengths below 250 nm, photo-bleaching occurs more prominently since the probability of exciting the electron to the triplet state increases. This is a stable state with a long lifetime and can interact with other molecules to produce irreversible covalent modifications. Photo-bleaching therefore results in a decrease to the fluorescence yield since molecules undergo photon induced chemical damage.

The destruction of the molecule is proportional to the emission intensity, the emission time and the number of excitation and fluorescence cycles undergone. In order to reduce the effect of photo-bleaching undergone during testing, the laser was scanned over a 20x20 μm^2 area and the acquisition time was limited to

one second per spot tested. Three spots along the irradiated region and three spots along the un-irradiated regions of each sample were tested in order to gauge the ratio of loss to fluorescence yield over the wavelength range of 350-500 nm.

Each test required manually starting the acquisition and switching the laser onto the sample simultaneously. An uncertainty in the time of exposure from laser switch on to acquisition start time was therefore estimated to be ~2-3 seconds. Photo-bleaching vs time correlation curves were therefore made over a 30 second time span. These were used to correct the data. Fluorescence experiments were conducted in the year after irradiation was performed.

4.2.4. Raman Spectroscopy

Raman spectroscopy was conducted in order to identify if a change in species occurs within the scintillators when subjected to radiation damage. The Raman Effect is the result of inelastic scattering of light, whereby incoming photons interact with lattice phonons to cause virtual excitations. These virtual excitations then de-excite by releasing a photon of wavelength corresponding to a specific virtual mode. These Raman active modes are characteristic of certain bonding structures. Thus, from a Raman spectrum, one can identify the specie and bonding structure within a solid by identifying their corresponding peaks.

Raman spectra were obtained for the un-irradiated control samples as well as on the 0.8 MGy, 8 MGy and 25 MGy irradiated samples using the LabRAM HR Raman spectrograph. A 514 nm Argon laser was used to excite the Raman modes. The spectrograph was calibrated using the 579 cm^{-1} peak (yellow doublet) expected from a mercury discharge lamp.

The Rayleigh peak that results from elastic light scattering was eliminated by using a notch filter. The noise of plasma lines that arise from the laser were filtered out with an interference filter. Raman studies for the 0.8 MGy samples were conducted 10 days after irradiation while 8 MGy and 25 MGy samples were tested 4 weeks and 6 weeks after irradiation respectively. Spectra obtained were analysed using the LabSpec5 software tool.

5 Results and analysis

5.1. Observations

After irradiation, samples obtained a yellow to brown discolouration as dose exposure increased. After removal from the microprobe, samples were exposed to air and a fading of the discolouration was observed. For the 800 kGy irradiated samples, the fading occurred within several minutes from removal and irradiated regions needed to be marked quickly so as to discern the irradiated spot.

The higher dose irradiated samples had a more gradual fade, with a region of permanent discolouration remaining after several days. Figure 5-1 shows the discolouration after irradiation in EJ208 samples of different doses. Figure 5-2 shows two ~25 MGy irradiated samples after they have healed and some of the discolouration has faded.



Figure 5-1: EJ208 samples irradiated to doses of ~80 MGy, 25 MGy, 8 MGy and 0.8 MGy from left to right.



Figure 5-2: Fading of discolouration observed in ~25 MGy irradiated EJ208 samples.

It was also observed that samples irradiated to doses of 25 MGy and higher became more rigid and brittle. Due to their small sizes, samples were handled with tweezers during placement and removal from holders. Samples were easily scratched and care had to be taken when handling them. The scintillators were handled along their corners and edges in order to prevent scratches over the irradiated regions.

5.2. Results of the light transmission

The light transmission spectra with respect to air, for all the tested samples over several days, are shown in Appendix C. At the high wavelengths, ~10-20% of the transmission loss is typically due to reflections at the sample interface. Small fluctuations in the data may be due to systematics arising from different placement of the scintillators or surface scratches formed through handling. These fluctuations fall within 3 sigma of the average, leading to a maximum of 5% uncertainty in the data.

5.2.1. Features in the transmission spectra

All the un-irradiated blue emitting scintillators have an absorption edge starting at ~410 nm, which completely falls off at around 320-330 nm. Within this absorptive edge region, additional absorption peak features (observed as transmission dips) are present and vary for the different types of scintillators. This wavelength region corresponds to where light absorption by the secondary fluors are expected.

The PVT based EJ200, EJ208 and BC408 each have a peak at ~350 nm and their spectra show similar features. The UPS923A and Tilecal types also have similar features to each other, due to their structural similarity, and show peak features at ~350 nm, 365 nm and 385 nm. EJ260, which is the green emitting scintillator, has its fall-off region starting around 475 nm, with complete absorption occurring below 350 nm. Additional absorption features occur at ~430nm and 455 nm.

After irradiation, the formation of similar features are observed in the respective spectra of the various sample types. For the lowest administered dose of ~0.8-1 MGy, changes to the absorptive features in the fall-off regions occur. In particular, an increase in transmission is observed over this region for the blue scintillators.

Since these regions correlate to absorption by the fluors, less absorption could lead to a breakdown in the light transfer mechanism and hence a loss in final light output of the scintillators. This effect is further enhanced in the ~8 MGy Tilecal samples, and partially present in the UPS923A samples, both of which contain the polystyrene base as well as a larger fraction of fluors versus the other scintillator types.

As the exposure dose is increased, a shifting of the absorptive edge to higher wavelengths is observed. This new absorptive component may mask the effect of absorption loss by the fluors. The features are a result of free radical production caused by the radiation damage. These free radicals compete for light absorption and therefore quench the eventual light yielded by the scintillator. Since this additional absorptive component corresponds to the blue wavelength region, this accounts for the yellow discolouration observed in the scintillators.

In addition, a certain portion of the shifted absorptive tint is seen to recover over time. A significant amount of this recovery occurs within the first day after irradiation. This correlates with the visual fading of the discolouration observed in the samples. Samples were stored out of direct contact with visible light between irradiation and testing, but were exposed to air. It is believed that the healing is therefore mostly driven due to free radicals interacting with oxygen thereby causing their bleaching.

Although the scintillator transmissions were monitored over a day to day bases, a time concise correlation was not made. Hence a comparison between the rates of recovery between the different scintillator types could not be drawn. The transmission spectra taken 4 weeks after irradiation were used for the comparative study.

5.2.2. Comparison of light transmission loss

The following six plots show the relative transmission of each scintillator type for the various doses, 4 weeks after irradiation.

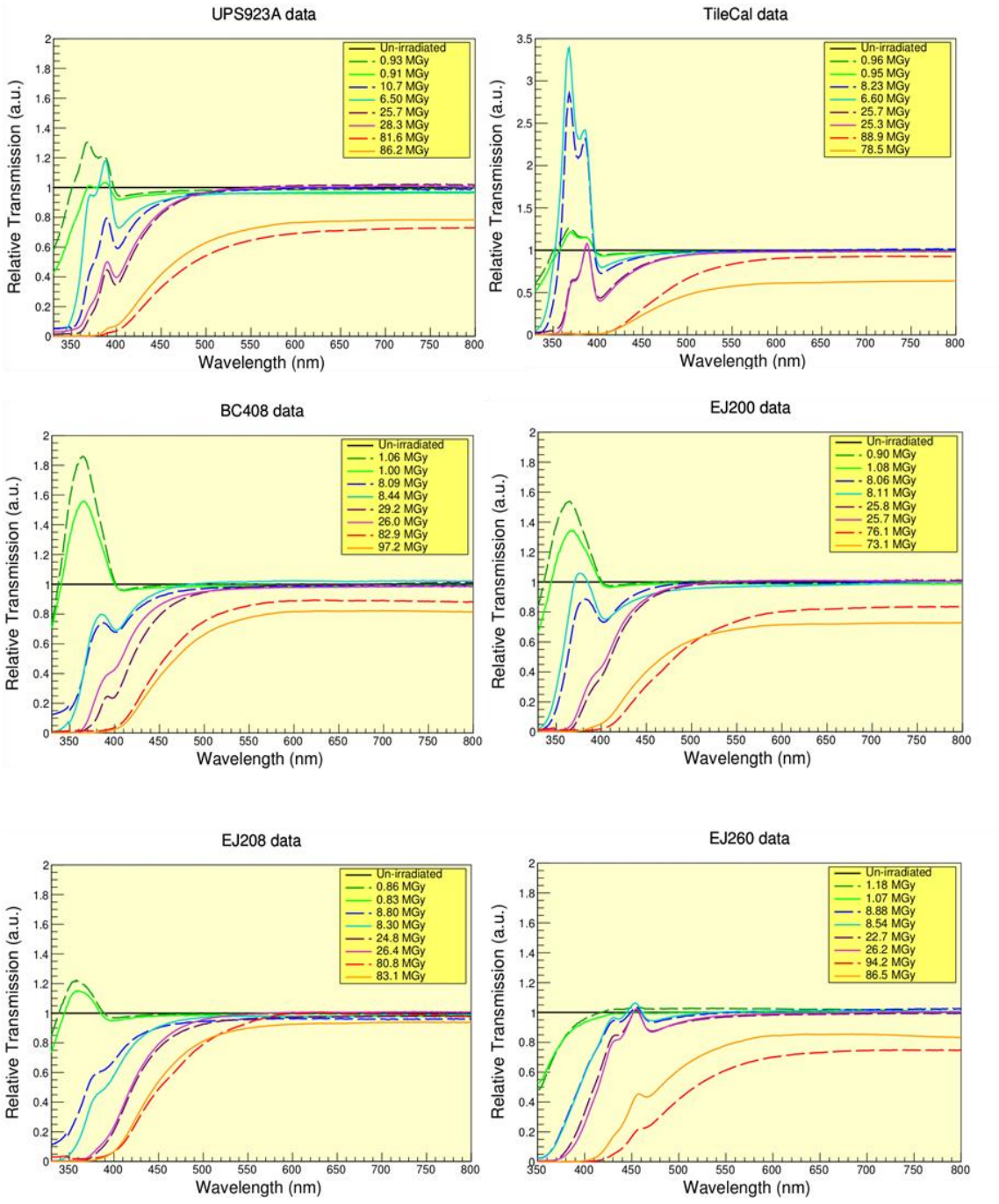


Figure 5-3: Relative transmission spectra at several dose for the different scintillator types, taken four weeks after irradiation.

The relative transmission is computed by taking the ratio between the transmissions in irradiated to un-irradiated samples. The spectra are multiplied by a correction factor computed as the ratio of the spectra of a control sample taken on the two respective days of testing. The development of an absorptive tint shifting to higher wavelengths as dose exposure is increased can be more clearly observed in these plots.

To compare the effect of transmission loss as a function of dose within the various samples, the loss at a wavelength of 430 nm is considered. This corresponds to the peak absorption wavelength of the fiber; Kuraray Y-11(200) [28]; that these scintillators are coupled to within the Tile Calorimeter and would give an indication into the performance of the scintillators as part of the coupled system. The relative transmission at 430 nm for the various samples 4 weeks after irradiation are shown in Figure 5-4 below.

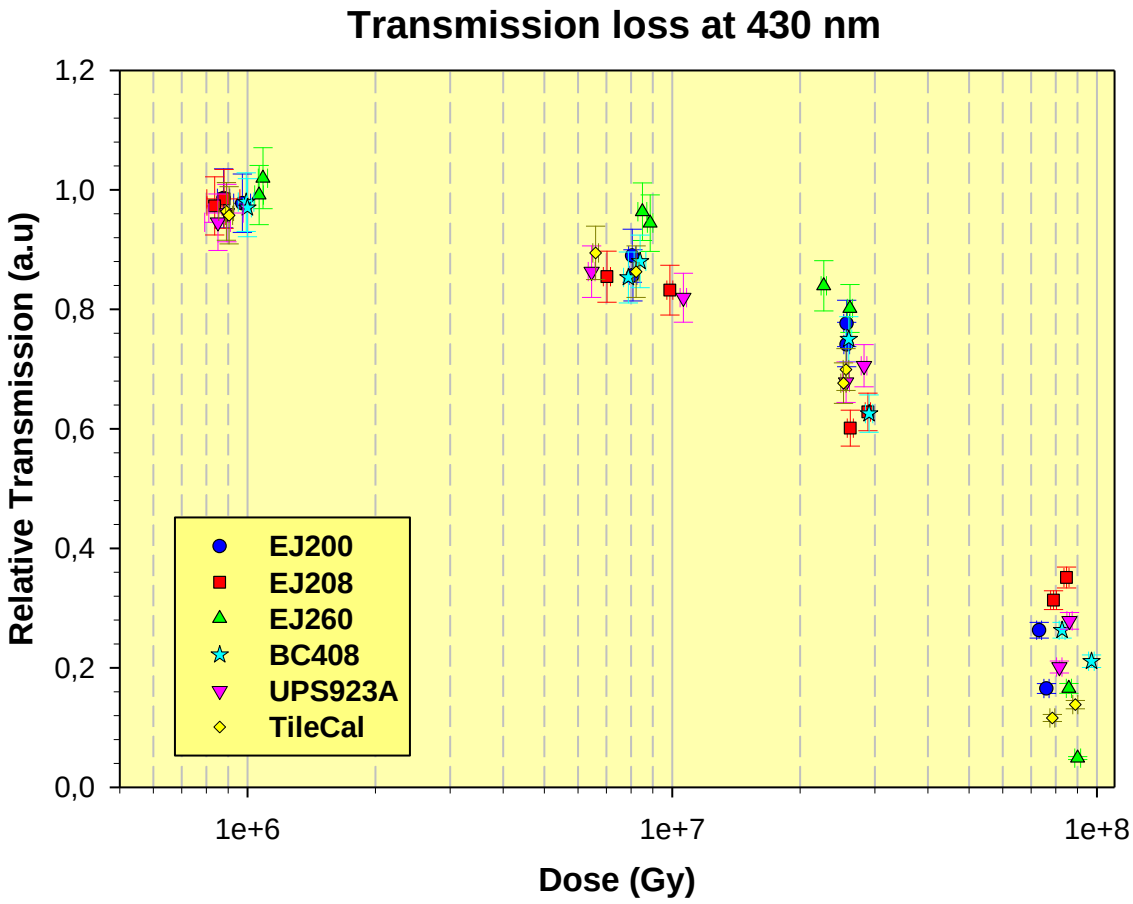


Figure 5-4: Relative transmission at 430 nm for the various sample types measured 4 weeks after irradiation.

The EJ260 scintillator has the least transmission loss at 430 nm, however at this wavelength, absorption by its fluor dopants are ongoing. In these scintillators, the free radicals formed would compete with absorption of light by the fluors, but wouldn't further quench the final wave-shifted light which has an emission peak at 490 nm. This feature is marketed as a contributor to the radiation hardness of these scintillators by the manufacturer [21].

The downside of this scintillator however is that it will not couple well to the Y11 fibers currently used in the detector, which absorb light over the range 420 -450 nm. Thus using EJ260 as a replacement candidate would require replacing the fibers as well. The radiation hardness of these would then have to be taken into account and may add additional costs.

The blue scintillators perform very similarly to each other. There aren't any major distinctions in the performance between the PVT and PS based scintillators in terms of their transparency loss at 430 nm. EJ200 appears to perform only slightly better than the other blue scintillators for the doses ranging between ~8 MGy and 25 MGy. EJ208 however, has the least transparency loss at the highest dose of ~80 MGy. It should be noted here that the peak emission wavelength of EJ208 is at 435 nm as compared to 425 nm for all the other blue scintillators.

Since all of the scintillators have slight variations in their absorption regions based on the types of fluors which they are doped with, comparing their transparency loss at one wavelength alone is not sufficient. Figure 5-5 therefore shows the relative transmission for each scintillator at their respective wavelengths of maximum light emission.

This plot further confirms that for the higher wavelength shifting scintillators, i.e. EJ260 and EJ208, less transmission loss occurs at their wavelengths of maximum light emission. Therefore, their emitted light will be subjected to less quenching via competitive absorption by free radicals as compared to the standard blue emitting scintillators. Furthermore, these standard blue emitting scintillators perform within 20% variation of each other.

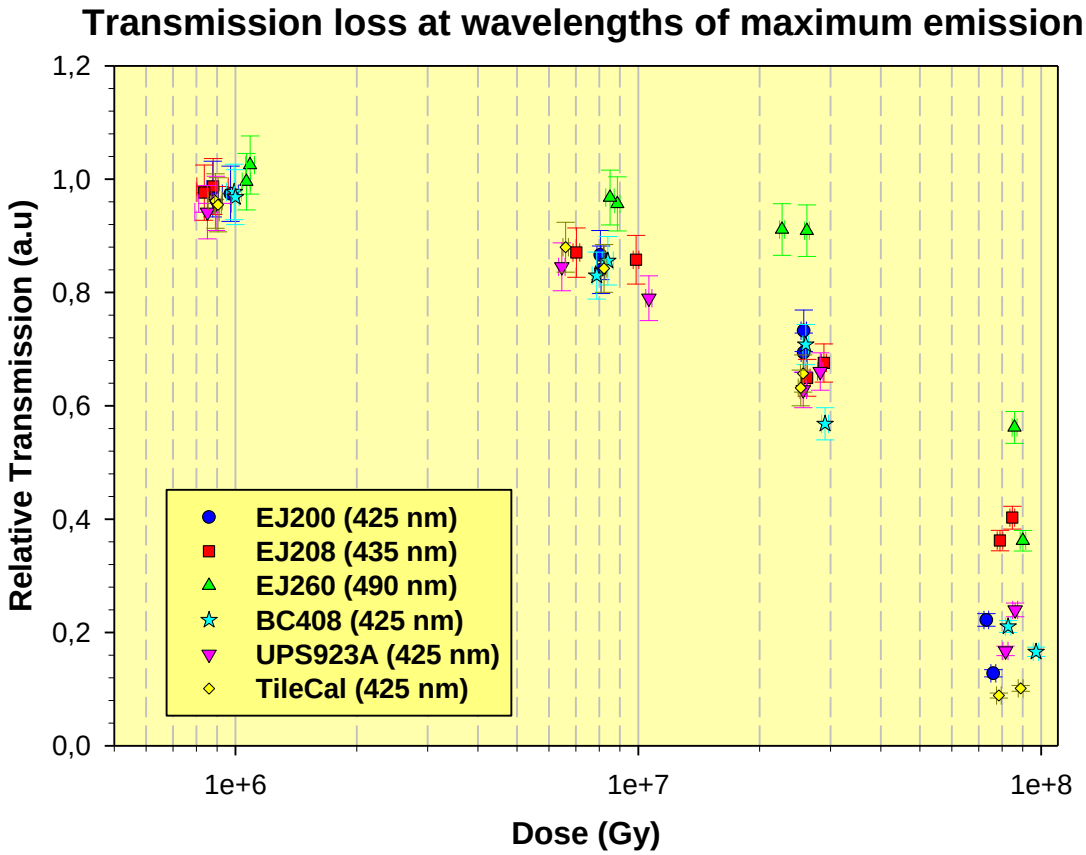


Figure 5-5: Relative transmission for the various sample types at their respective wavelengths of maximum emission, measured 4 weeks after irradiation.

Studying the transmission loss has given insight into the two possible mechanisms responsible for the optical changes observed in radiation damaged plastic scintillators. These are; damage to fluors resulting in reduced absorption and hence loss of emitted light shifted to higher wavelengths, and the formation of free radicals which quench scintillation light. Furthermore, the higher wavelength shifting scintillators (EJ260, followed by EJ208) showed the least loss in light transmission.

5.3. Results of the light yield studies

To assess the light yielded by the different radiation damaged scintillator samples, their response to a Sr^{90} beta electron source was tested. The current across a photomultiplier coupled to the scintillator via two fibers, was measured as a function of radiation source position. An example of the mapping of this

PMT signal verses source position over a scintillator sample is shown in Figure 5-6.The mapping is correlated to the position of the sample within the set-up shown to the right.

A small gap occurs between the sample holder and the lead cover, leading to a region where beta electrons emitted by the Sr90 source interact with the two fibers. This is demarcated by the yellow box. The approximate region of the sample is demarcated in the brown box. A background signal is obtained by averaging over the region within the red box, and is subtracted from the rest of the mapping before analysis.

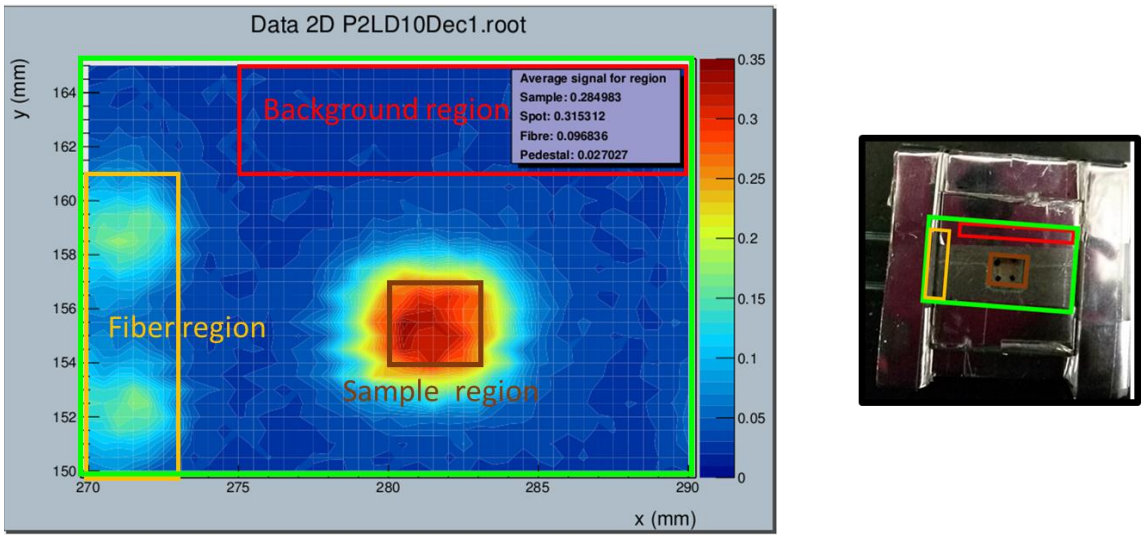


Figure 5-6: 2D mapping of the PMT signal with Sr90 source position, indicating signal regions corresponding to regions on the experimental set-up.

The beta electrons emitted by the source can interact over a 2 mm lateral radius from the actual position of the source. Hence the signal obtained for the 1 mm diameter fiber spans over ~5 mm. This is similarly observed over the sample region. Since samples were tested after irradiation only, the intention was to compute the ratio of light loss by taking the ratio between the signal over the irradiated spot region and an un-irradiated “corner region” of the same sample.

This however was not an accurate measure due to the large range of the interaction of the source. Thus, a control un-irradiated sample for each scintillator type had to be tested as well so that a comparison of the loss could be

made. Figure 5-7 shows 3D mappings indicating loss to the light yield signal for different irradiation doses of EJ200 samples. Photographs of the sample indicating where the corresponding spot regions occur are also shown.

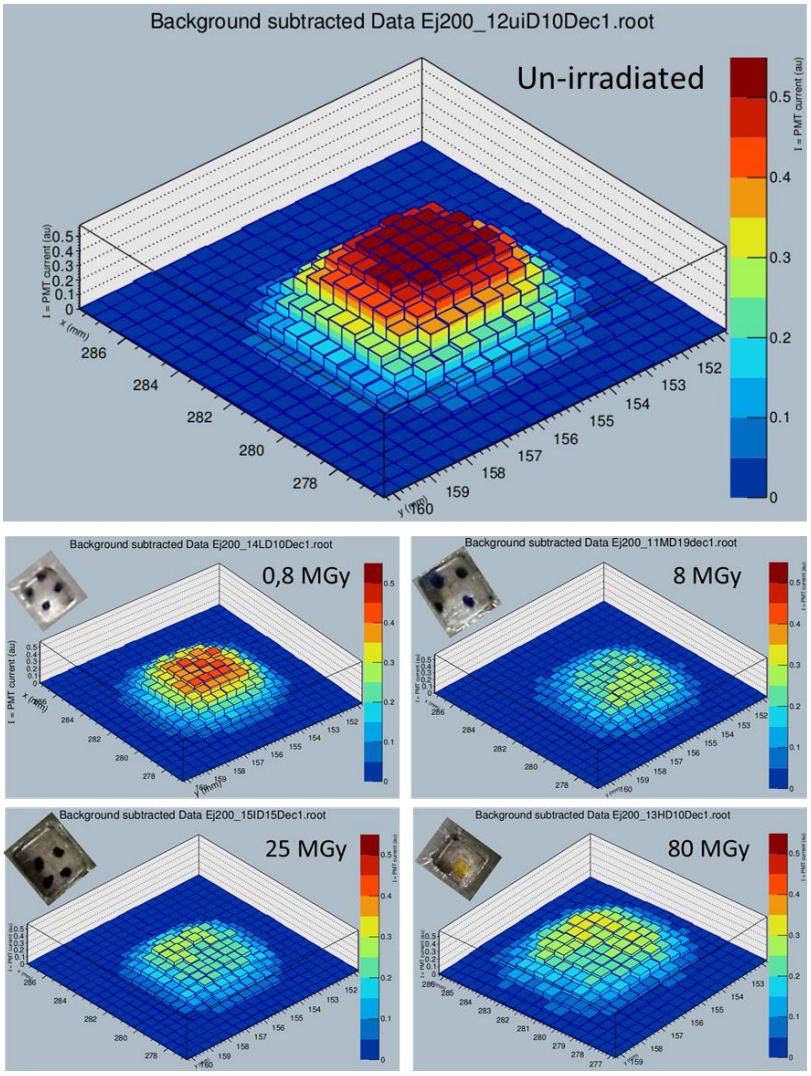


Figure 5-7: 3D mappings of the light yield for several EJ200 samples with different levels of proton induced radiation damage.

Three measurements were taken for each sample, with the sample rotated in the holder for each measurement. It was observed that the geometry of the sample tested played a large impact on the magnitude of the PMT signal measured. This is because the amount of light transferred between the scintillator and the fiber is dependent on the contact made between the two. Thicker samples therefore make a better contact and result in a larger measured signal. The different samples also varied slightly in their size, with edge lengths varying by up to 0.3

mm. This further impacted on the signal measured. A comparison between the potential systematic variations and their impact on the three measured signals tested per sample is drawn in Figure 5-8 for all the TileCal samples tested.

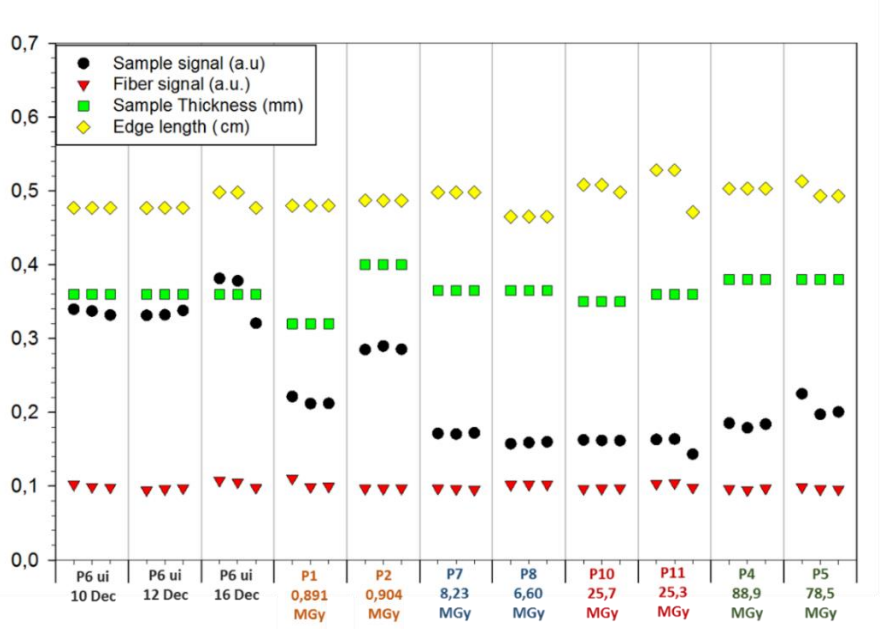


Figure 5-8: The effect of the experimental systematics on the measured light yield signal.

In Figure 5-8, the sample signal is the integrated signal over the sample region. The fiber signal is the signal integrated over the fiber region. Since the position of the fibers and holder are kept fixed, this measurement can act as a control for systematics such as variation in the particle flux of the source, fluctuations in the high voltage gain applied over the PMT, etc. The edge length is the length of the scintillator sample edge that makes contact with the two fibers. In this comparison, it is evident that these systematic variations have a large impact on the results of the experiments conducted.

In order to analyse the light yield loss as a function of irradiation dose, the sample signals were normalised by correcting for variations in thickness, contact length and fiber signal. The ratio between the corrected signals for the irradiated and un-irradiated samples was then computed. These results are shown in Figure 5-9. Whilst the correction factors slightly improved the precision of the three repetitive measurements, large uncertainties in the accuracy of the ratio computed still remain.

The results of the corrected light loss ratio however, do correlate with the expected performance of the scintillators. EJ260 exhibits the least loss, however the actual signal obtained for its un-irradiated sample was a factor of 3 smaller than that obtained for the un-irradiated EJ200 sample. The blue scintillators performed very similarly once again, with EJ208 exhibiting the most radiation resistance against loss to light yield.

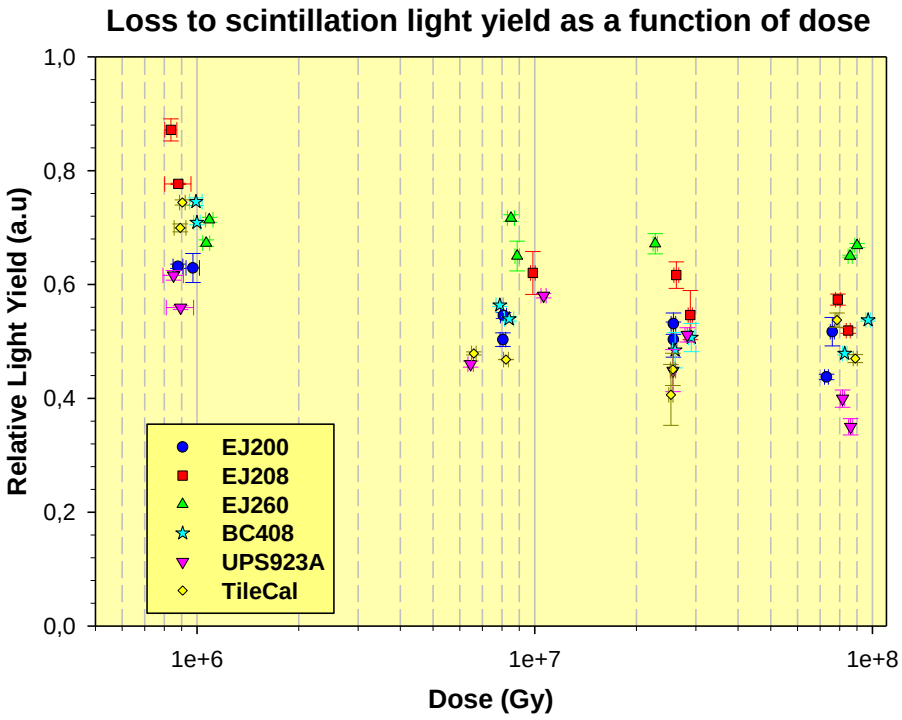


Figure 5-9: Relative light yield as a function of radiation damage dose.

The light box set-up used for these experiments typically measure much larger scintillator samples. Although a measurement could be made for the small samples in our study, the actual signals were small and sensitive to systematic errors. The UPS923A data particularly showed a large variation, but these samples also had large geometric variations. Other factors that may have led to errors in the data include the surface conditions of the scintillators. Since the edges were handled with metal tweezers, slight scratches and cracks could have formed which would influence the contact made between these edges and the read-out fibers.

5.4. Results of the fluorescence studies

The fluorescent light emitted by the plastic scintillators upon excitation with a 229 nm laser was measured. The photo-bleaching of this fluorescent light was minimised by reducing the laser exposure time as well as scanning the laser over the region being measured. These conditions coupled with the detector positioning resulted in fluorescence off the surface region being measured rather than observing "bulk" effects. Photo-bleaching time correlation tests were also performed in order to correct the data.

The average spectra of three measurements for the un-irradiated and irradiated regions respectively for all the samples under testing are shown in Appendix D. Their corresponding photo-bleaching vs time correlation curves are also shown alongside each spectra.

5.4.1. Fluorescence peak features

Several fluorescence peak features can be observed amongst the spectra. Peaks falling within the wavelength region of 300-375 nm correlate to fluorescence off the PVT/PS base. Since this fluorescence is predominantly from the benzene ring structure in both base types, the same "two-peak" feature over this region is seen in the un-irradiated spectra for all the different scintillator types tested.

In the wavelength region of 375-500 nm, the fluorescence correlates to that of the fluor dopants. These peak features therefore vary between the different scintillator types. The peaks reach a maximum between 400-430 nm for all the blue emitting scintillators.

EJ260 shows additional peak features at ~460 nm and 490 nm, however these are weaker than expected. It is possible that due to the experimental conditions, the emitted light measured had less spatial interaction with the fluors responsible for shifting the emitted light into the green wavelength region.

The effect of limited spatial interaction could also explain why peaks in the base fluorescence region have a high intensity comparable to the fluor regions for both the green and blue emitting scintillators. If fluorescence was measured over the bulk rather than at the surface, majority of the "base emitted light" would be re-absorbed and shifted to higher wavelengths through interaction with the fluors.

For the samples exposed to radiation damage, a general trend in the features are observed. For doses of ~0.8-1 MGy, an overall intensity loss occurs, with a more distinct loss to fluorescence in the fluor emission regions (375-500 nm). At this dose, very minimal transmission losses were observed in the transmission spectra, although a feature indicating loss to absorption by the fluors occurred.

At progressively higher doses, the fluorescence intensity is further decreased, with significant loss over both the base and fluor regions. At the 80 MGy dose range, a very weak signal is obtained with an additional peak feature appearing in some of the spectra. This peak feature could not be correlated to any particular damage effect and may be influenced by several factors such as sample thickness and dose rate.

5.4.2. Photo-bleaching vs time correlation

The photo-bleaching effect was assessed by acquiring several spectra along the same spot with continuous laser beam exposure over a period of ~30 seconds. An example of the bleaching effect observed is shown for an un-irradiated EJ200 sample in Figure 5-10.

The photo-bleaching vs time correlation graphs were plotted by taking the ratio between the integrated spectra for each measurement to that of the ~0 sec measurement. The photo-bleaching correlations for both the irradiated and un-irradiated regions of each sample are shown in Appendix D, alongside their respective fluorescence spectra. The curves have been fitted with the equation $f(x) = y_0 + ae^{-tb}$.

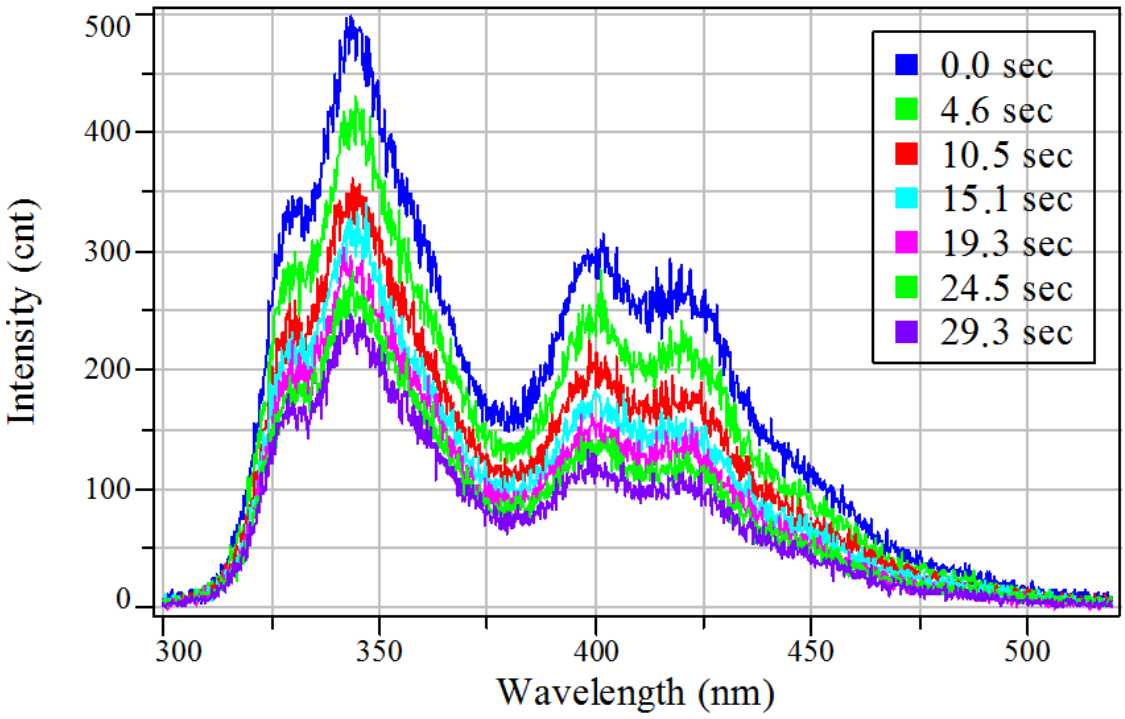


Figure 5-10: Spectra showing the photo-bleaching of fluorescence lights with laser exposure time for an un-irradiated EJ200 sample.

The trend observed in the correlations graphs indicate that the rate of photo-bleaching occurs more rapidly as irradiation exposure increases for all of the scintillator types besides BC408. BC408 shows a slowing down in the bleaching rate of the irradiated samples. The bleaching occurs over both the base and fluor emission regions.

There are several factors that could influence the rate of photo-bleaching observed, however, more investigations are needed to fully understand this effect. Potential factors to consider include the types of fluors present and their concentrations by weight; as well as structural changes influenced by dose rate dependant damage.

The photo-bleaching correlation curves were used to deduce a correction factor for the fluorescence data used in the comparative study. Figure 5-11 shows how the correction factor '*C'* was calculated, with the relevant equations used. The correction was calculated for $t = 3$ *seconds*.

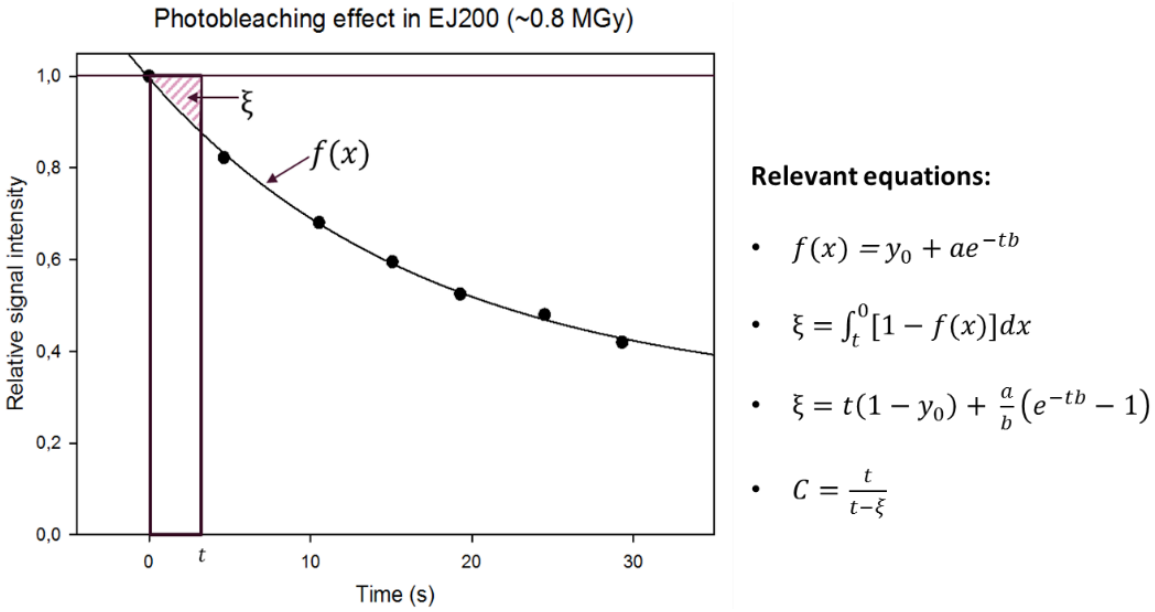


Figure 5-11: Representation of how the correction factor *'C'* was computed using the photo-bleaching correlation curves and relevant equations

5.4.3. Comparison of fluorescence results

In order to compare the effect of fluorescence loss against radiation dose for the different scintillator types, the ratio of the spectra for the irradiated and un-irradiated regions were computed. The ratio was computed using:

$$Fluorescence\ Ratio = \frac{Fluorescence_{irr} \times C_{irr}}{Fluorescence_{ui} \times C_{ui}}$$

Here *'irr'* and *'ui'* represent the irradiated and un-irradiated regions of the same sample respectively. The ratio was computed for fluorescence at 430 nm and integrated over 300-500 nm. The plots of fluorescence ratio verses irradiation dose for the various samples are shown in Figure 5-12 and Figure 5-13 respectively.

For fluorescence loss at 430 nm, EJ260 exhibits the least loss followed by EJ208. The UPS923A scintillators perform comparably well with EJ208, particularly at the higher dose exposures. The TileCal scintillators perform well against loss at the low doses, but lose light much faster at higher doses. After 25 MGy, EJ200 performs on par with EJ208 and UPS923A.

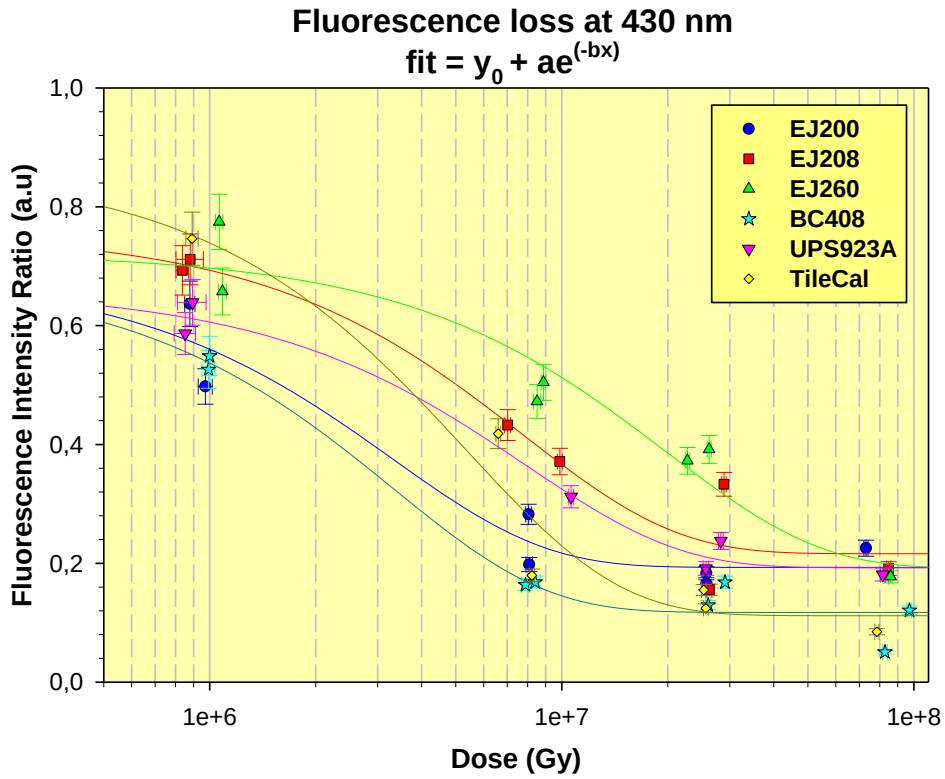


Figure 5-12: Fluorescence loss at 430 nm.

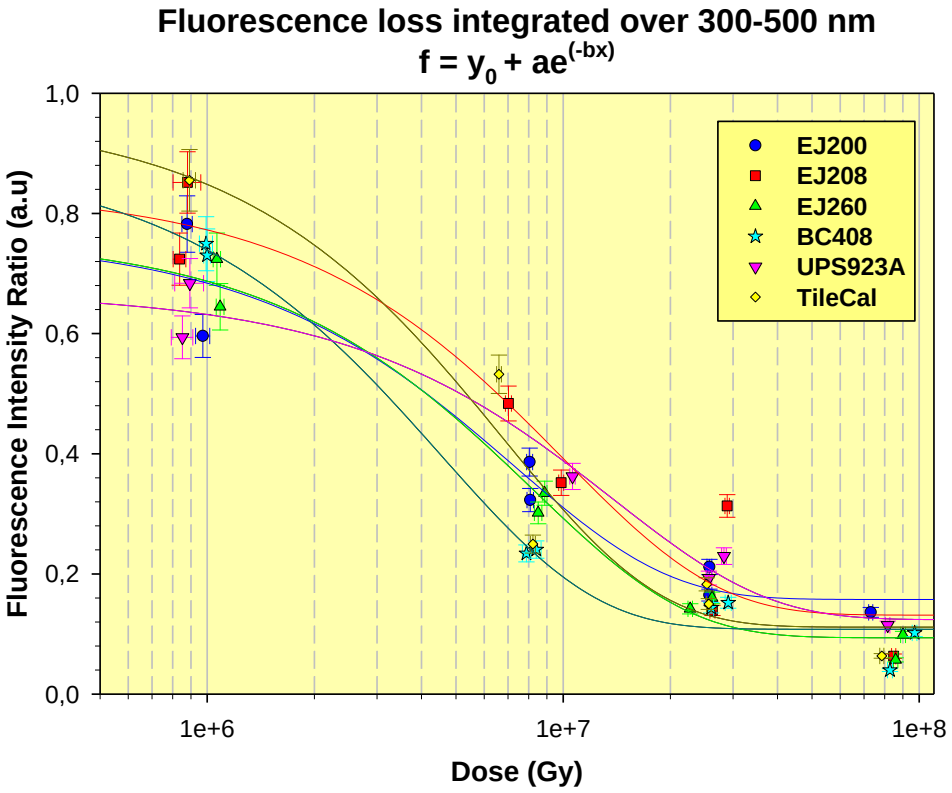


Figure 5-13: Fluorescence loss integrated over 300-500 nm

For the integrated region of 300-500 nm, the different scintillators perform within a 20% variation of each other. EJ260 no longer exhibits the least loss as would be expected based on the results of the light yield study. However, it should again be noted that only surface fluorescence is being probed in this experiment. EJ208 overall performs the best against surface fluorescence light loss in thin scintillators.

5.5. Results of Raman spectroscopy

Raman spectra for the different samples irradiated to ~800 kGy, 8MGy and 25 MGy were measured 10 days after, 4 weeks after and 6 weeks after irradiation respectively. The measurements were made using a 514 nm excitation laser. The spectra are shown in Appendix E.

As observed, an increase in dose exposure led to an increase in the fluorescent background. For this reason, samples irradiated to ~80 MGy could not be assessed since this background suppressed the Raman peaks. This additional fluorescence may arise from free radicals since the formation of an absorptive tint covering the wavelength of 514 nm increased with dose, as observed from the transmission testing.

The fluorescence background was subtracted from the data using the LabSpec5 software tool. The background subtracted spectra are also shown in Appendix E. All spectra were normalised to the 1000 cm^{-1} peak with an intensity of 5000 counts. This peak represents the C-C aromatic ring vibration typical of benzene.

Figure 5-14 shows the Raman spectra for the un-irradiated samples of each scintillator type. The range of the Raman shift (cm^{-1}) corresponds to the wavelength range of 514-620 nm. In the Raman technique, the intensity of a particular feature is proportional to the concentration of that corresponding specie.

In these scintillators, the fluor concentrations are small (< 2.5%), and hence the features observed coincide with the base structure only. Therefore, the same peak features are seen in polystyrene based UPS923A and TileCal samples.

Similarly, the same features are seen among the polyvinyl toluene based EJ200, EJ208, BC408 and EJ260 samples. Owing to the similarity in structure of PVT and PS, many of the peaks observed in the PVT based samples are also present in the PS based ones. The EJ260 spectrum has an additional fluorescence background due to its higher wavelength shifting capabilities, thus leading to a lower spectral resolution. This background has been subtracted out in Figure 5-14.

The respective peaks were assigned to their corresponding vibrational modes using the Raman Peak assignment datasheet from Horiba Jobin-Yvon (Refer to Appendix F). These are summarised in Table 5-1.

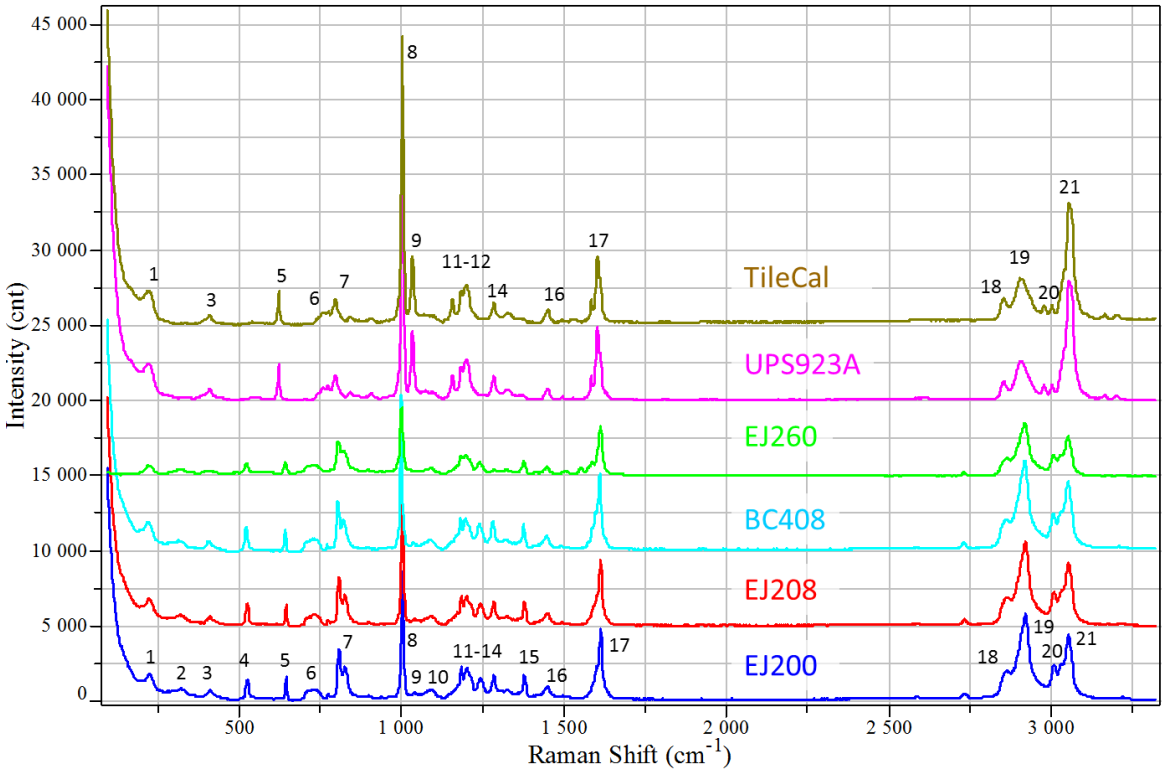


Figure 5-14: Raman spectra for the un-irradiated plastic scintillator samples

Table 5-1: Summary of peak allocation to functional and vibrational groups

Peak number	Assigned Vibrational Mode
1-2	δ(C-C) aliphatic
3-7 , 9-14	ν(C-C) alicyclic or aliphatic chain vibrations
8	ν(C-C) aromatic ring chain vibrations
15	$\delta(CH_3)$
16	$\delta(CH_2)$ or $\delta(CH_3)$asymmetric
17	ν(C=C)
18-19	ν(C-H)
20-21	ν(=(C-H))

5.5.1. Structural damage as a function of dose

This section refers to the spectra shown in Appendix E. An example of the spectra for the EJ208 type scintillator is shown below. Similar features are observed for the different scintillator types.

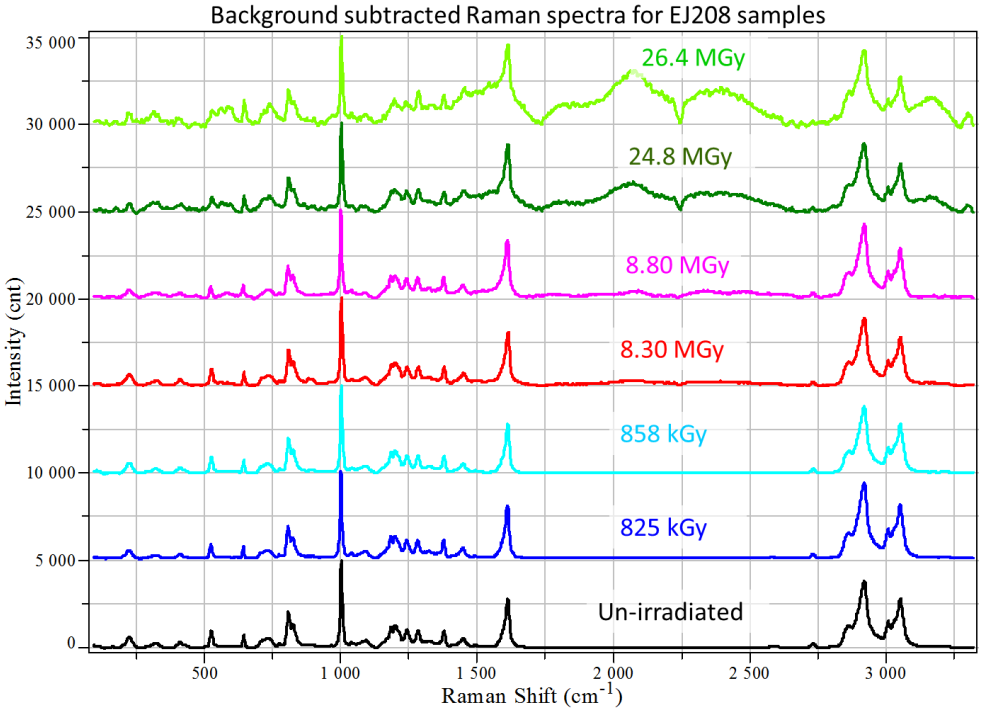


Figure 5-15: Raman spectra for EJ208 samples.

At doses of < 1 MGy, the scintillators maintain their structural characteristics and the same spectral features are observed. As the dose exposure progresses to 8 MGy, additional peak features begin to appear in the regions of 500-650 cm^{-1}, 1800-2250 cm^{-1} and 2250-2500 cm^{-1}.These peak features become more prominent as dose is increased to ~25 MGy.

The 500-650 cm^{-1} peak corresponds to that of (C-C) alicyclic or aliphatic chain vibrations. A strong peak in the region of 2100-2250 cm^{-1}, corresponds to a $\nu(C \cong C)$ bond, however no assignment data could be found to correlate for the region of 2250-2500 cm^{-1}. Since these peaks are broad, they could have arisen from an additional fluorescence process that was not accounted for in the background subtraction.

These peaks are most prominent in the EJ260 and EJ208 data, both of which contain wavelength shifting fluors that absorb and emit light to higher wavelengths. The Raman spectra for EJ260 samples irradiated to 25 MGy could not be obtained since fluorescence had saturated the signal.

A possible explanation for the formation of the additional peak at 500-650 cm^{-1}, can be made by considering bond breakage in the benzene ring. If the C-H bonds are broken, this could result in dehydrogenation (loss of hydrogen) or even loss of larger mass C_nH_n structures. This effect was observed by Torrisi [17] upon conducting in situ mass spectroscopy on polyvinyl toluene undergoing proton irradiation. In particular, stripping the benzene of its hydrogen would result in the formation of alicyclic rings, aliphatic chains or even $C \cong C$ bonds.

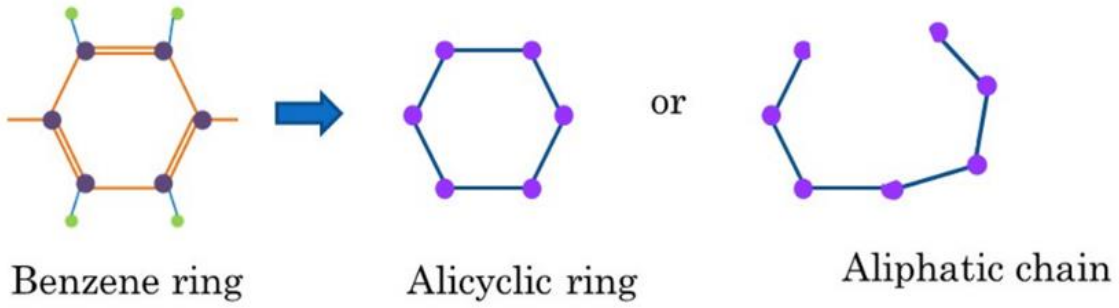


Figure 5-16: Possible configurations resulting from dehydrogenation of benzene.

5.5.2. Healing of structural damage

Raman spectra for the 8.11 MGy irradiated EJ200 sample were measured 3 days, 10 days and 4 weeks after irradiation. The background subtracted Raman spectra for these are shown in Figure 5-17. A plot of the ratios between each peak intensity to the intensity of peak 8 (C-C aromatic) is shown in Figure 5-18.

Three days after irradiation, the structure contains a larger amount of specie related to the vinyl backbone (peaks 15-21) verses benzene ring type vibrations, thus indicating damage to the benzene ring. There is an increase in the higher vibrational energy aliphatic modes and small decreases in the lower energy modes.

After 10 days, some recovery of the original ratios are observed. After 4 weeks, the ratios are significantly recovered. A small increase in some aliphatic modes remain as well as a 4% increase in the ratio of C=C bonds. It should also be noted that the additional peak forming at 500-650cm^{-1}, loses a small amount of intensity as the recovery occurs

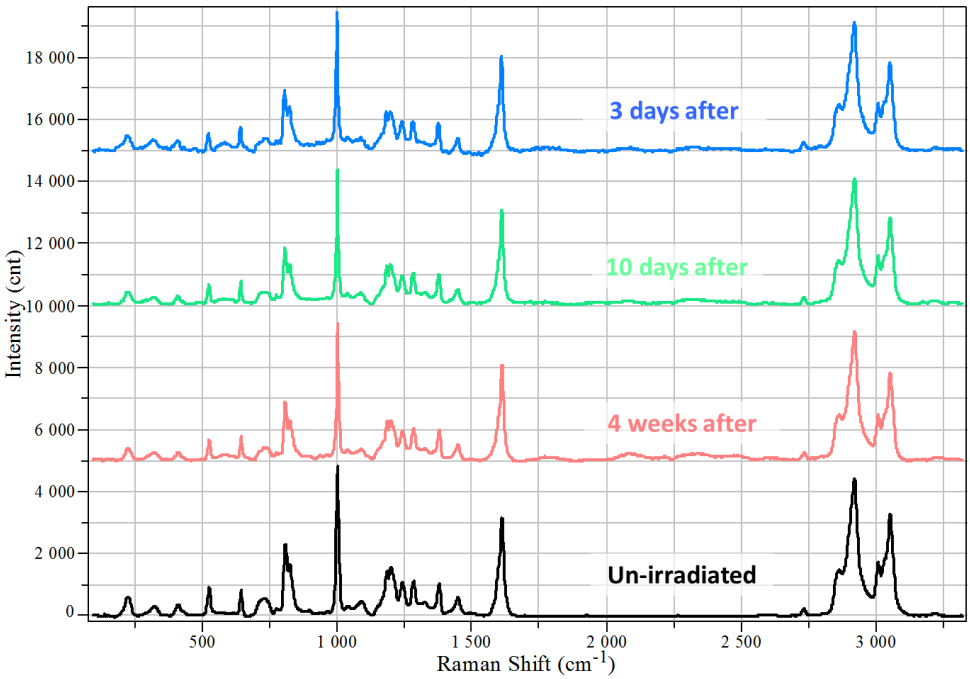


Figure 5-17: Background subtracted Raman spectra for EJ200 sample measured several days after radiation exposure to a dose of 8.11 MGy.

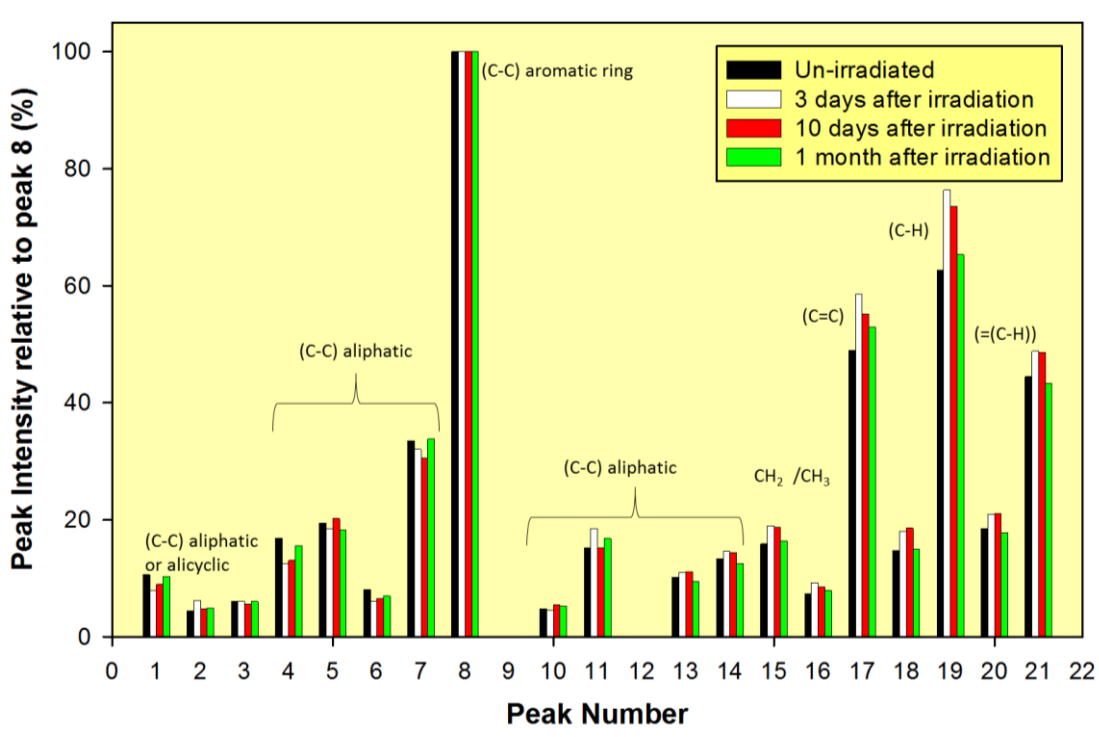


Figure 5-18: Plot of Raman peak intensity ratios relative to the C-C aromatic peak intensity for EJ200 sample irradiated to 8.11 MGy.

6 Conclusion

The Tile Calorimeter of the ATLAS detector will be replacing the plastic scintillators employed in its Gap region as part of the 2018 upgrade. These upgrades are being implemented in order to ensure an optimal performance of the detector during the next several data taking periods, where particles will be collided at higher energies and increased luminosity. Since these conditions will result in a harsher radiation environment, the scintillators used will need to exhibit a strong radiation damage tolerance.

As such, the radiation damage undergone by several polyvinyl toluene and polystyrene based plastic scintillators was investigated. Samples of 350 µm thickness were subjected to 6 MeV proton irradiation at doses of approximately 0.8, 8, 25 and 80 MGy using the 6 MV tandem accelerator of iThemba LABS. Transmission spectroscopy, fluorescence spectroscopy and light yield studies were used to assess the optical changes undergone by the damaged scintillators. Raman spectroscopy was used to study the structural properties.

Overall, the extent of damage undergone was proportional to the exposure dose. For doses of ~0.8 MGy, scintillators maintained their transmission character over the visible wavelength range, however a loss in absorption correlating to the fluor absorption region occurred. This lead to a loss in light yield, which corresponded to a reduced fluorescence over the fluor emission region. The scintillators maintained their structural properties and damage could therefore be correlated to a bleaching related effect of the fluors.

As the exposure progressed to higher doses (> 8 MGy), the following were observed:

- Visible discolouration progressing from yellow to brown with dose.
- Formation of an absorptive component shifting to higher wavelengths with dose. As a result, scintillators lose transparency to their own scintillation light. Linked to free radicals or colour centre formation.

- Increasing loss to light yield with increasing dose.
- Loss to the 229 nm excitation driven fluorescence yield over both base and fluor emission regions.
- Structural changes to the PVT or PS base of the scintillators

The scintillators showed recovery of transmission character as well as structural recombination within 4 weeks after irradiation. The most significant recovery of transmission occurred within 3 days after irradiation with exposure to air. It was noted that oxygen could be a driving factor since it may react with free radicals and result in bleaching of the competitive absorption that they cause.

The scintillators were prone to photo-bleaching upon excitation with a 229 nm excitation laser (also in the presence of air), and dose exposure impacted on the rate of bleaching undergone by the scintillators. This would be an interesting effect to study in further detail since bleaching of the fluors in plastic scintillators is a driving factor behind radiation damage as well. The same fundamental mechanism is responsible for bleaching effects, photo-bleaching and natural aging of scintillators driven by sunlight exposure.

The Raman spectra for 8 MGy samples showed small changes to the structure of the polymer base, with less aromatic ring type vibrations and additional alicyclic/aliphatic chain vibrations, C=C bonds and potentially $C \cong C$ bonds. Damage to the C-H bonds of the benzene ring may lead to hydrogen degassing and hence could account for the observed structural changes. The degassed hydrogen may be lost to free radicals.

The Raman technique using the 514 nm excitation laser was not sufficient enough to accurately study the structural damage undergone for the higher dose exposures due to the additional fluorescence background. The use of a longer excitation wavelength, such as 718 nm, could reduce this background effect and may be considered for future experiments. The downside of this would be a loss in the number of Raman active modes that could be studied.

Overall, EJ260 and EJ208 exhibited the most tolerance against radiation damage effects to their optical properties. Both these scintillators have secondary fluors that shift the final scintillation light to higher wavelengths. As a result, less competition for re-absorption of light by free radicals occurs in these scintillators as compared to the other common blue emitting ones.

EJ260, however, is a green emitting scintillator and its emission range will not couple well to the current optical fibers used by the Tile Calorimeter. These fibers were tested to have a greater radiation and stress tolerance versus clear fibers. If EJ260 is to be considered as a candidate for the upgrade, further studies on the radiation damage of the coupled scintillator-fiber-PMT system would be needed.

EJ208 on the other hand, performs considerably well in comparison to EJ260. It's wavelength of maximum emission at 435 nm couples well to the absorption maximum at 430 nm of the Y11 optical fibers. It also has a faster response time verses EJ260 according to the manufacturers. EJ208 is therefore recommended as a viable candidate to consider for replacing the current scintillators in the Gap region of the Tile calorimeter.

Since these studies were conducted on 350 μm thin samples, the influence of radiation damage on their bulk properties have not been considered. Future studies will therefore be conducted on thick scintillators so that the effect of their transmission loss to the attenuation length may be better understood. Scintillators having geometries similar to those used by the TileCal will be investigated.

Alongside this study, several other investigations into radiation damage of plastic scintillators are being conducted. These include electron paramagnetic resonance (EPR) studies [29], neutron induced radiation damage studies and dose rate dependence studies [30].The collaboration wishes to extend the studies further by investigating the radiation damage in coupled scintillator-fiber-PMT systems. The radiation damage in inorganic YSO (Y_2SiO_5) crystal samples will also be studied in collaboration with the JINR. The feasibility of plastic scintillators versus these YSO scintillating materials will be investigated for future HEP applications.

Appendix A

Description of the different sub-detector layers of the ATLAS detector

I. The Inner detector

The Inner Detector (ID) is situated closest to the beam pipe, and consists of three sub-detectors; the Pixel detector, the Semi-Conductor Tracker (SCT) and the Transition Radiation Tracker (TRT). It is surrounded by a superconducting solenoid magnet which generates a 2 Tesla magnetic field. The ID measures the curved tracks of charged particles which have been bent by the magnetic field generated by the solenoid magnet. It is designed to make high precision measurements, using the technologies of silicone sensors and straw drift tubes.

Both the Pixel detector and SCT contain modules with silicone microstrips. Charged particles passing through these modules remove electrons from the silicone layer, which migrate towards solder spheres hence generating a current. The current is read out by a layer of electronics and consequently digitized. Since the solder spheres are distributed in an array across the modules, the trajectory of the particle can be determined by tracking which spheres have a signal.

The TRT surrounds the SCT and pixel detectors. It is composed of ~50 000 gas filled tubes, each containing a gold plated tungsten wire in the centre. As charged particles traverse through the TRT, they ionise the gas and radiate photons which further interact with the gas to free electrons. The gold wire acts as an electrode to which electrons migrate and the current across the wire is measured. The TRT can distinguish between different types of charged particles since electrons generate more photons versus a pion and thus more negative charge is measured across the wire. Since the charged particle paths are measured by the inner detector under the influence of a known magnetic field, the momentum of these particles can hence be calculated. Neutral particles pass through the inner detector without leaving any track signatures behind.

II. The Calorimeters

Surrounding the ID concentrically are the Electromagnetic Calorimeters and the Tile Calorimeter, hadronic end-cap and forward calorimeters. The Calorimeters are based on "Sampling Calorimeter" technologies whereby particles interact with an absorber medium to generate particle showers which then deposit energy into an active sampling medium. The calorimeters measure the energy of both charged and neutral particles. They are designed to contain all electromagnetic and hadronic showers developing within them, and only neutrinos and muons manage to exit from these layers.

a. The Electromagnetic calorimeter

The Electromagnetic (EM) calorimeter measures mainly the energy of electrons and photons. It consists of a barrel region housed in a cryostat, flanked by two end-caps (EMEC). The barrel component has an accordion shaped structure containing layers of lead and stainless steel that act as the particle absorbers. Between these layers are copper grids immersed in liquid Argon (LAr) cooled to -183°C. The EMEC has a similar structure, but consists of a parallel plate geometry instead.

As a particle, for example an electron, passes through several layers of the EM calorimeter, it generates a large shower of low energy electrons, positrons and photons. The shower particles then ionise atoms in the LAr, thus creating more electrons and positive ions. The copper grid then functions as an electrode which the negative charges migrate to and the current is measured.

The EM calorimeter is designed such that electrons and photons stop within it. Therefore, by measuring the total charge deposited on the copper electrodes by a particular particle shower, the total energy of the original particle as it entered the EM calorimeter can be reconstructed.

b. The Tile Calorimeter

The Tile Calorimeter is responsible for measuring the hadronic component for energy reconstruction. It consists of a central barrel flanked by two extended barrels, each containing 64 azimuthally distributed modules. Each module contains a matrix of 4 mm thick steel plates with 3 mm thick tiles of plastic scintillators sandwiched in between. The scintillators are coupled to wavelength shifting optical fibers along two of their edges. These fibers are in turn connected to photo-multiplier tubes (PMT's).

As a high energy hadron passes through the tile modules, it interacts with the atomic nuclei of the steel absorber, to produce a shower of lower energy particles (typically quarks and gluons). These particle showers then interact with the scintillator tiles which absorb energy from the incoming particles and fluoresce to emit light. This blue emitted light is absorbed by the fibers along the scintillator edges and emitted at shifted wavelengths near the green region. The PMT's then detect the green shifted light and the signal is further processed with readout electronics in order to digitize the data for analysis thereafter [9].

c. The Hadronic End-cap and Forward Calorimeters

The hadronic end-caps (HEC) are situated in regions where stringent radiation environments need to be sustained and therefore utilise liquid argon detectors. They are housed along with the forward calorimeter (FCAL) and the EMEC in cryostats. The HEC is composed of two wheels on either side of the detector, each containing 32 modules composed of copper plates with gaps for the liquid argon to flow through. The detector works with a similar concept to that of the EM calorimeter.

III. The Muon spectrometer

The Muon spectrometer surrounds the calorimeters and operates within a magnetic field generated by eight toroidal magnets. The Muon spectrometer measures the tracks of muons as they are bent by this magnetic field. The spectrometer consists of Monitored Drift Tubes (MDTs), Resistive Plate Chambers (RPCs), Thin Gap Chambers (TGCs) and Cathode Strip Chambers (CSCs). The TGCs and RPCs provide precision triggers for muons at the detector ends and centre respectively. The MDT's are 0.85-6.5 meters long, with a diameter of 3 cm and are filled with gas. As a muon passes through the tubes, it interacts with the gas and leaves a trail of electrons and ions behind. These then drift to the sides and centre of the tube, and the time it takes to drift is measured. By correlating the drift time between several tubes, the position of the muon as it passes through the detector can be determined.

Appendix B

Table B-1 summarising the proton irradiation conditions for EJ200, EJ208 and EJ260 samples.

Sample		Thickness (um)	Average beam current (nA)	Irradiation time (min:sec)	E_loss per proton (J)	Integrated charge (C)	Absorbed dose (Gy)	Dose Error (Gy)	Estimated average dose rate (Gy/s)
EJ200	14	385	0,425	12:00	5,78E-13	310,3	8,78E+05	2,91E+04	1,20E+03
	18	330	0,627	7:00	4,72E-13	360,2	9,71E+05	4,44E+04	1,69E+03
	11	340	1,25	38:05	4,91E-13	2953	8,04E+06	1,55E+05	3,41E+03
	17	360	1,45	35:30	5,33E-13	2894	8,08E+06	1,68E+05	4,05E+03
	15	335	3,47	45:15	4,82E-13	9496	2,57E+07	4,00E+05	9,41E+03
	16	330	3,53	44:35	4,72E-13	9541	2,57E+07	4,05E+05	9,52E+03
	13	365	14,1	32:00	5,44E-13	27063	7,61E+07	1,07E+06	3,96E+04
	19	390	8,18	52:40	5,89E-13	25669	7,31E+07	9,74E+05	2,33E+04
EJ208	13	300	0,409	18:40	4,34E-13	322,9	8,80E+05	7,89E+04	1,11E+03
	17	330	0,608	8:20	4,72E-13	310,0	8,36E+05	3,42E+04	1,64E+03
	12	300	0,964	44:15	4,34E-13	2574	7,02E+06	1,36E+05	2,63E+03
	18	350	1,92	30:55	5,12E-13	3577	9,87E+06	1,59E+05	5,30E+03
	15	350	2,53	63:00	5,12E-13	9518	2,63E+07	4,31E+05	6,98E+03
	16	360	3,81	45:15	5,33E-13	10345	2,89E+07	4,18E+05	1,06E+04
	11	320	17,0	29:00	4,53E-13	29609	7,90E+07	1,26E+06	4,54E+04
	14	370	10,3	48:00	5,55E-13	29955	8,48E+07	1,18E+06	2,91E+04
EJ260	17	330	0,486	13:00	4,72E-13	402,9	1,09E+06	2,74E+04	1,31E+03
	18	340	0,454	14:20	4,91E-13	390,6	1,06E+06	2,54E+04	1,24E+03
	15	360	2,24	24:40	5,33E-13	3177	8,87E+06	1,31E+05	6,25E+03
	16	380	0,788	64:10	5,78E-13	2966	8,50E+06	2,04E+05	2,26E+03
	b6	370	2,99	57:20	5,55E-13	9258	2,62E+07	3,65E+05	8,46E+03
	19	350	2,74	50:10	5,12E-13	8243	2,27E+07	3,36E+05	7,56E+03
	11	320	12,7	41:55	4,53E-13	33759	9,01E+07	1,44E+06	3,39E+04
	13	365	7,96	64:00	5,44E-13	30550	8,59E+07	1,21E+06	2,24E+04

Table B-2 summarising proton irradiation conditions for BC408, UPS923A and TileCal samples.

Sample		Thickness (um)	Average beam current (nA)	Irradiation time (min:sec)	E_loss per proton (J)	Integrated charge (C)	Absorbed dose (Gy)	Dose Error (Gy)	Estimated average dose rate (Gy/s)
BC408	10	360	0,754	8:00	5,33E-13	355,5	9,92E+05	4,19E+04	2,10E+03
	11	360	0,839	7:10	5,33E-13	357,8	9,99E+05	2,19E+04	2,34E+03
	2	320	0,868	56:40	4,53E-13	2952	7,88E+06	1,99E+05	2,32E+03
	6	320	0,657	79:50	4,53E-13	3146	8,39E+06	2,66E+05	1,75E+03
	13	370	2,845	60:10	5,55E-13	10270	2,91E+07	5,74E+05	8,05E+03
	14	320	3,351	48:40	4,53E-13	9755	2,60E+07	4,24E+05	8,94E+03
	7	330	10,17	50:30	4,72E-13	30689	8,28E+07	1,32E+06	2,74E+04
	8	335	12,66	47:10	4,82E-13	35802	9,71E+07	1,48E+06	3,43E+04
UPS923A	11	335	0,414	13:30	4,82E-13	329,5	8,93E+05	8,31E+04	1,12E+03
	19	360	0,645	8:10	5,33E-13	305,1	8,51E+05	5,93E+04	1,80E+03
	12	335	1,11	59:00	4,82E-13	3916	1,06E+07	1,88E+05	3,01E+03
	18	360	2,26	17:10	5,33E-13	2314	6,46E+06	1,18E+05	6,31E+03
	14	350	3,03	51:10	5,12E-13	9302	2,57E+07	4,68E+05	8,36E+03
	16	350	3,57	47:50	5,12E-13	10253	2,83E+07	4,26E+05	9,85E+03
	13	350	10,8	45:50	5,12E-13	29555	8,15E+07	1,19E+06	2,98E+04
	17	380	11,6	43:20	5,78E-13	30059	8,62E+07	1,23E+06	3,32E+04
Tilecal	1	320	0,814	6:50	4,53E-13	333,9	8,91E+05	3,58E+04	2,17E+03
	2	400	0,856	6:00	6,22E-13	308,2	9,04E+05	1,72E+04	2,51E+03
	7	365	0,819	59:30	5,44E-13	2923	8,21E+06	1,35E+05	2,30E+03
	8	365	0,714	54:50	5,44E-13	2348	6,60E+06	1,04E+05	2,01E+03
	10	350	2,17	71:20	5,12E-13	9294	2,56E+07	3,93E+05	5,99E+03
	11	360	3,27	46:10	5,33E-13	9063	2,53E+07	3,65E+05	9,13E+03
	4	380	13,3	39:00	5,78E-13	31019	8,89E+07	1,22E+06	3,81E+04
	5	380	12,4	36:50	5,78E-13	27386	7,85E+07	1,06E+06	3,55E+04

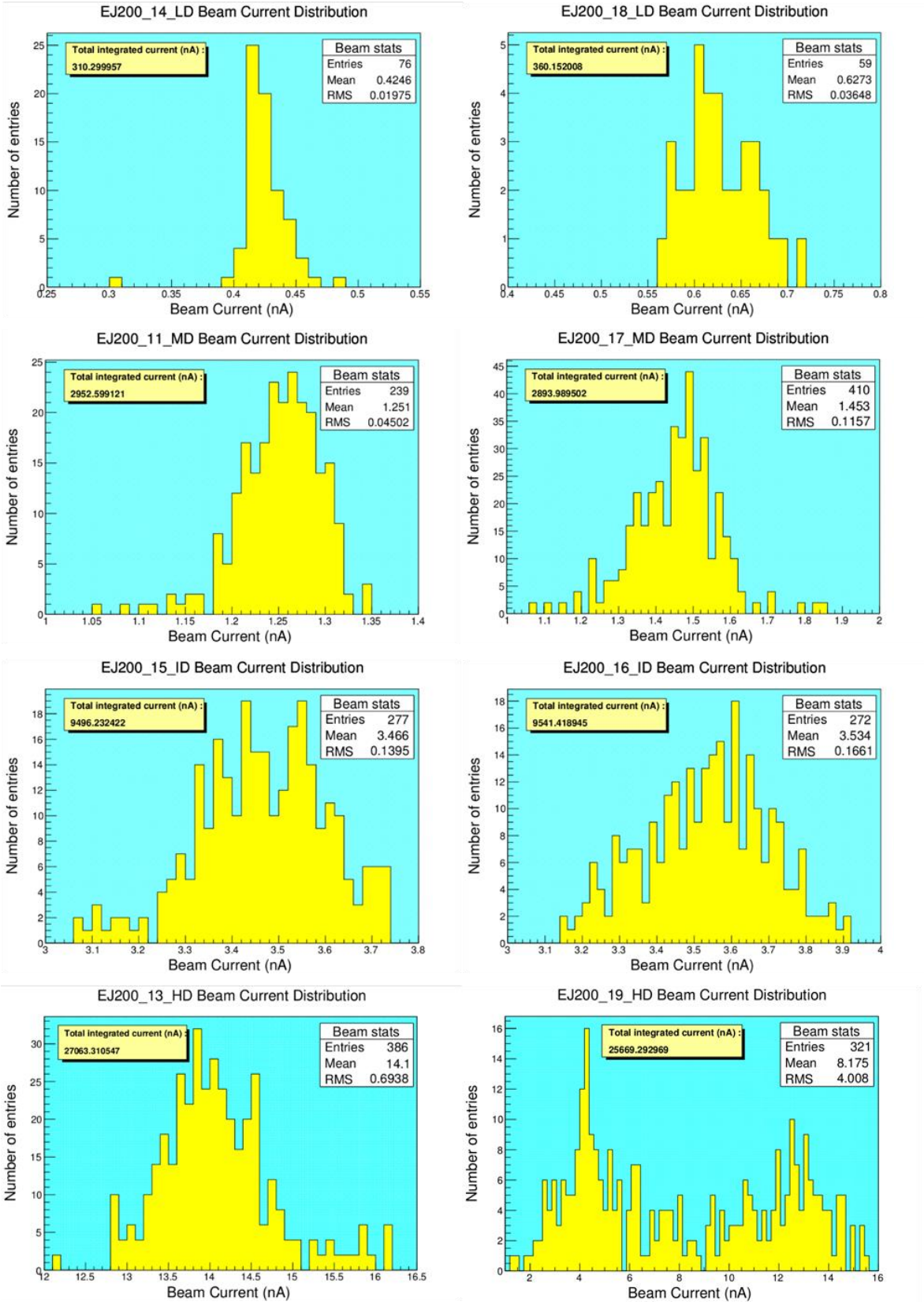


Figure B-1: Beam current distributions for the various EJ200 samples.

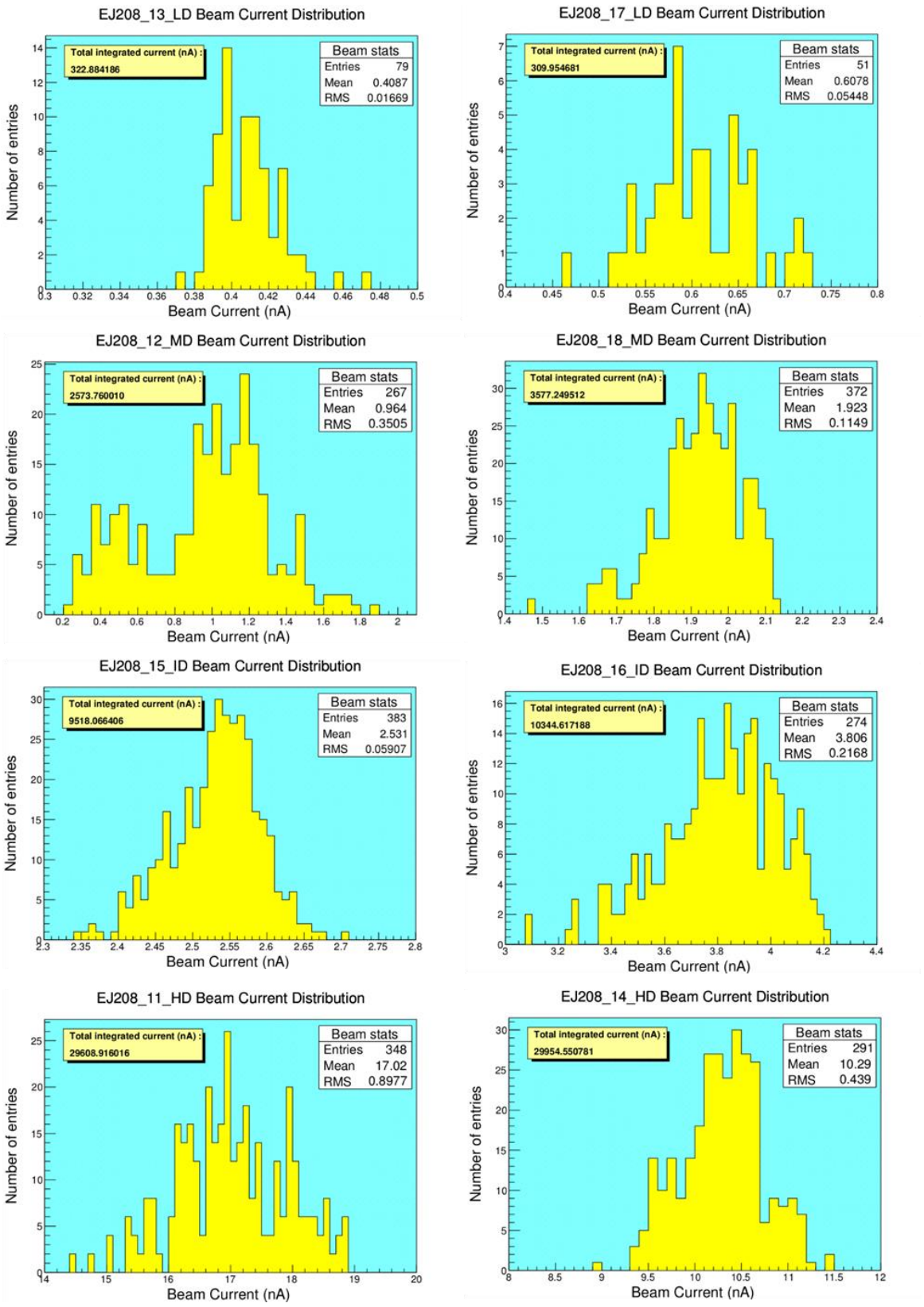


Figure B-2: Beam current distributions for the various EJ208 samples.

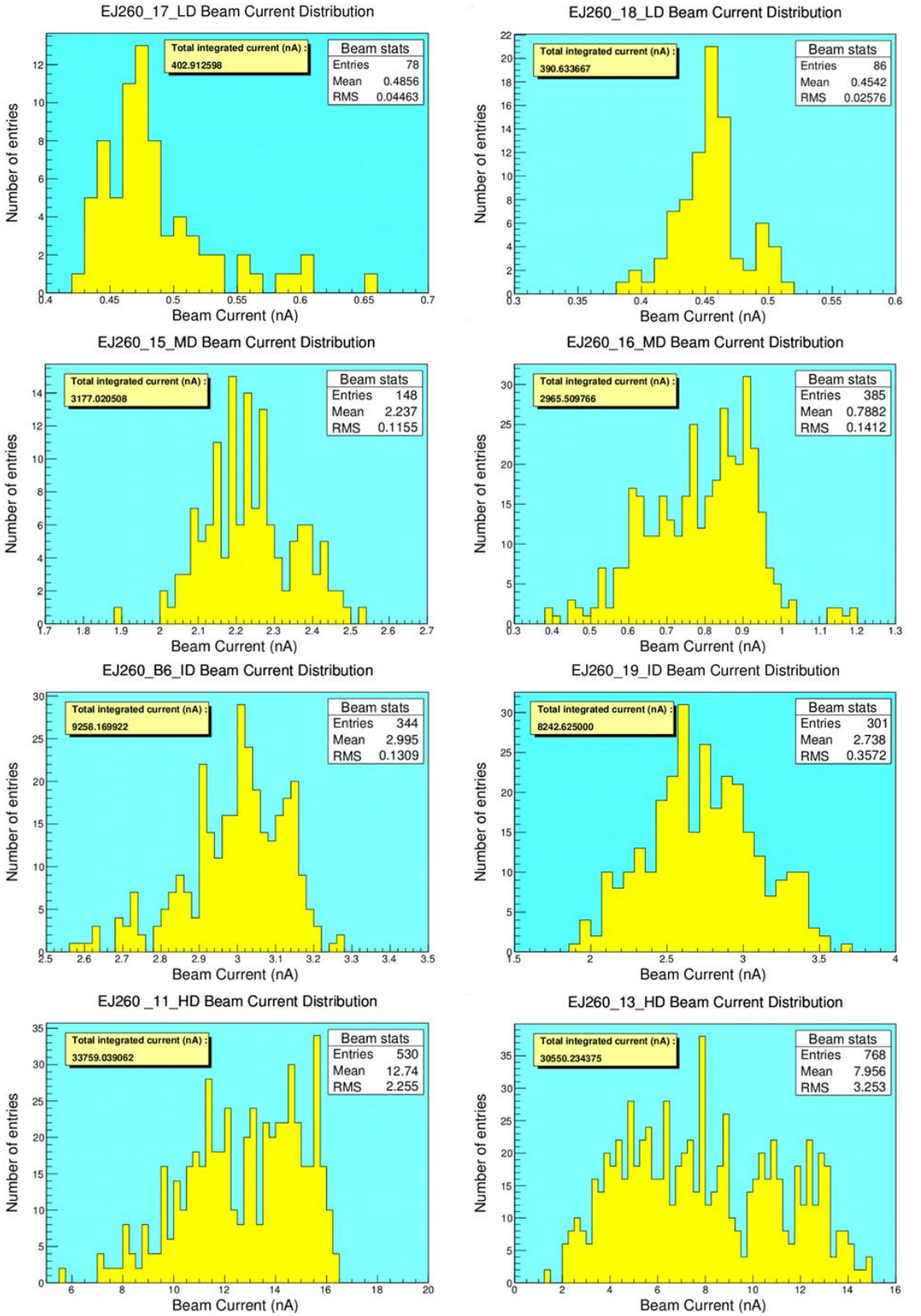


Figure B-3: Beam current distributions for the various EJ260 samples.

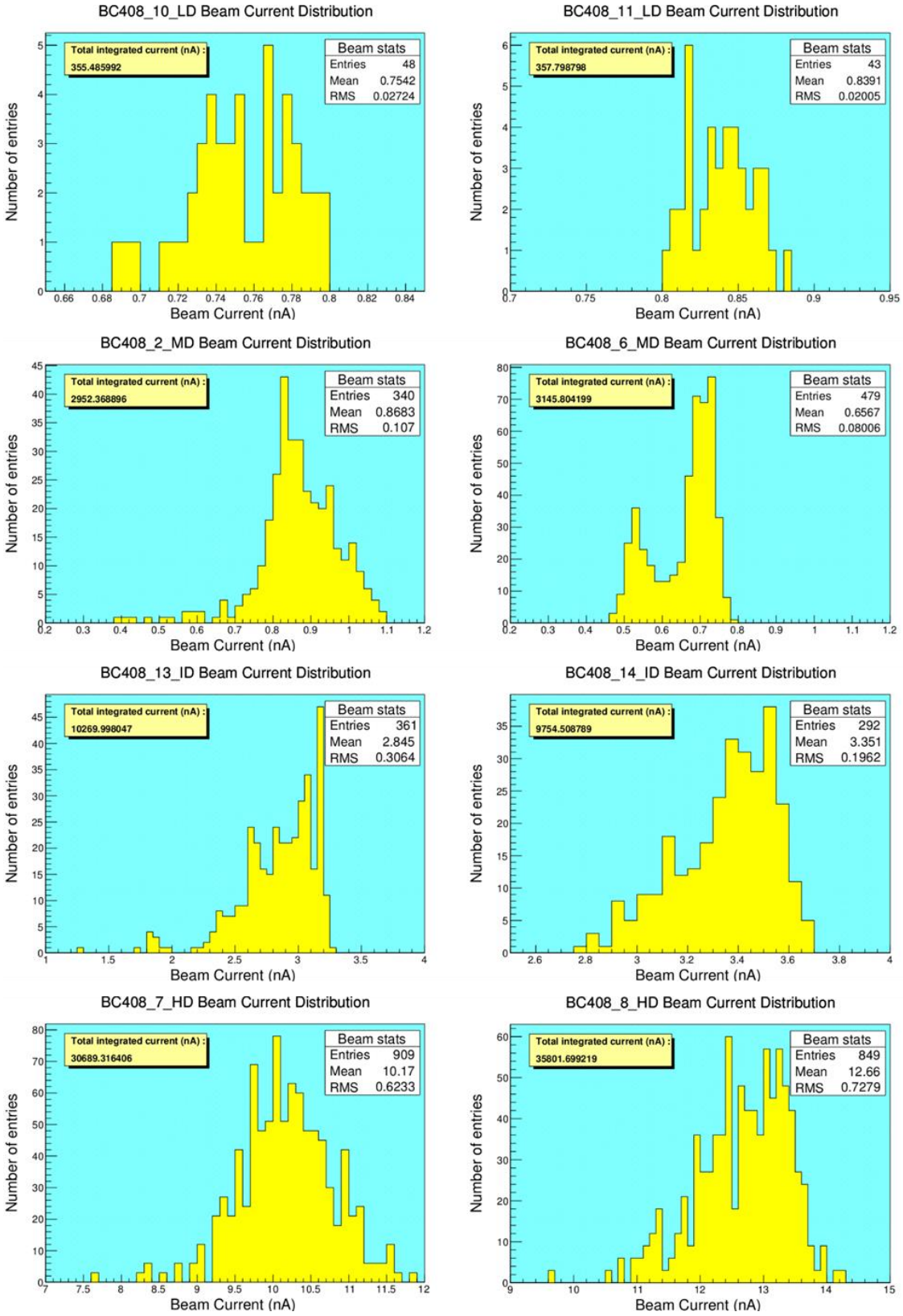


Figure B-4: Beam current distributions for the various BC408 samples.

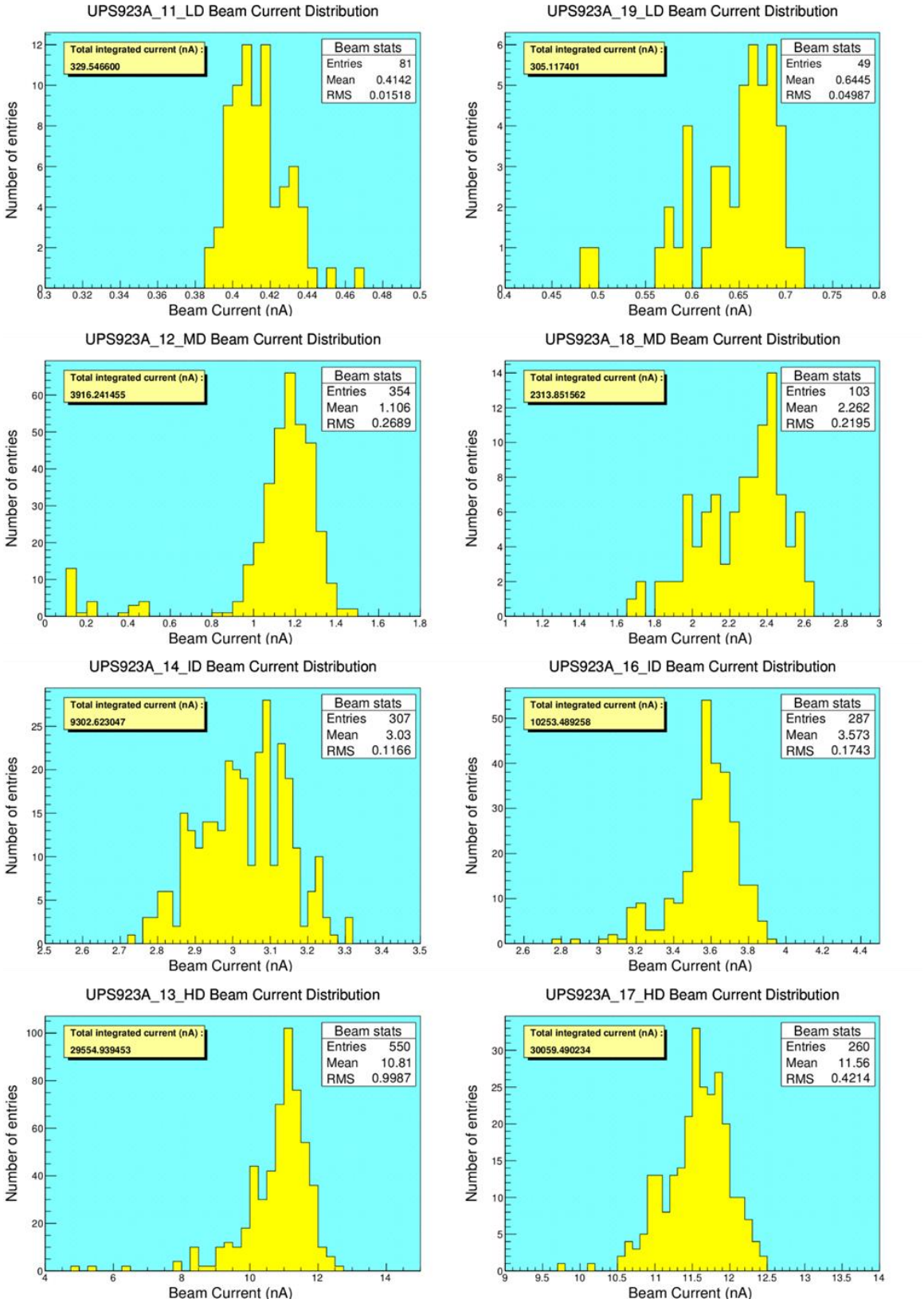


Figure B-5: Beam current distributions for the various UPS923A samples.

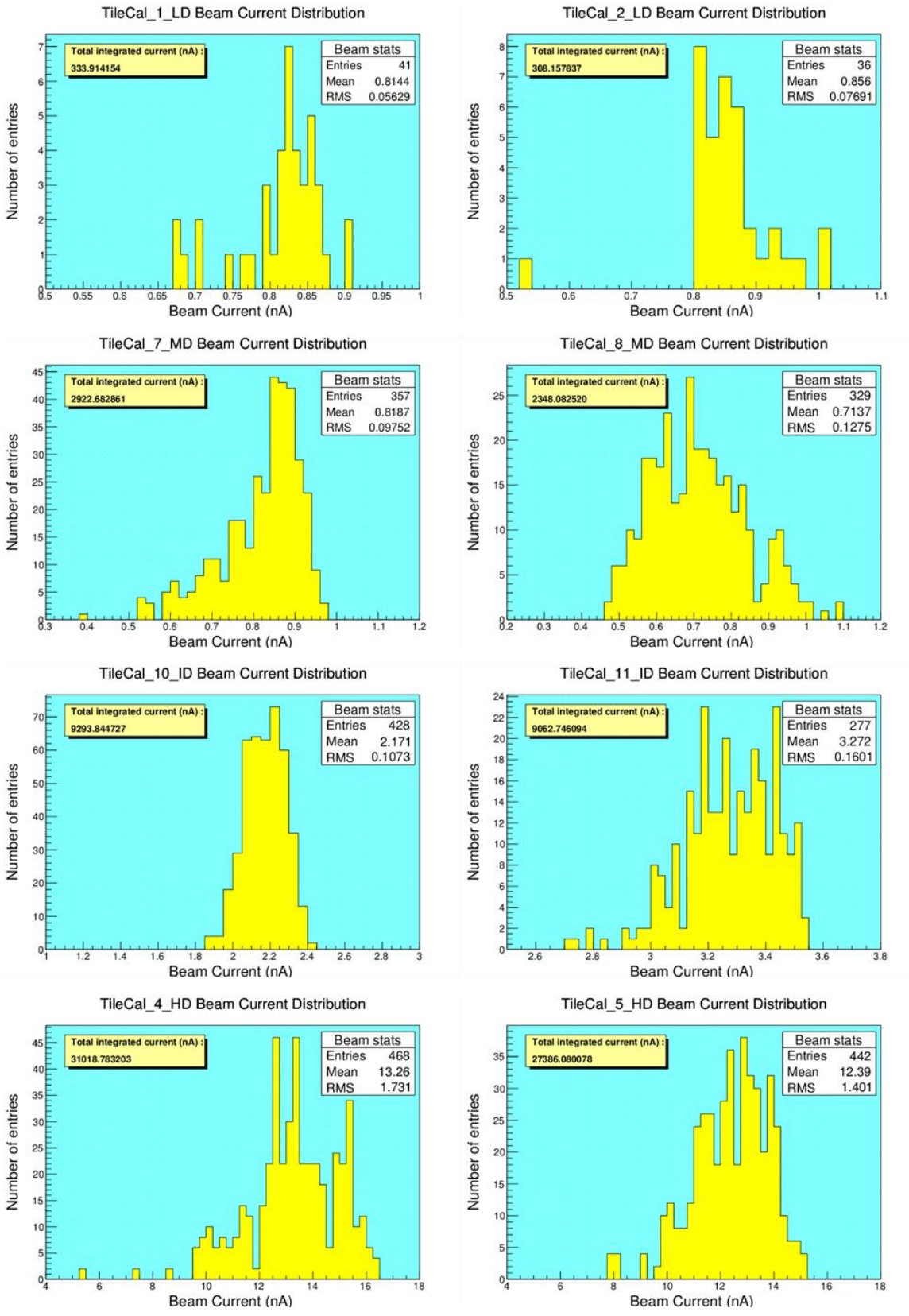


Figure B-6: Beam current distributions for the various TileCal samples.

Appendix C

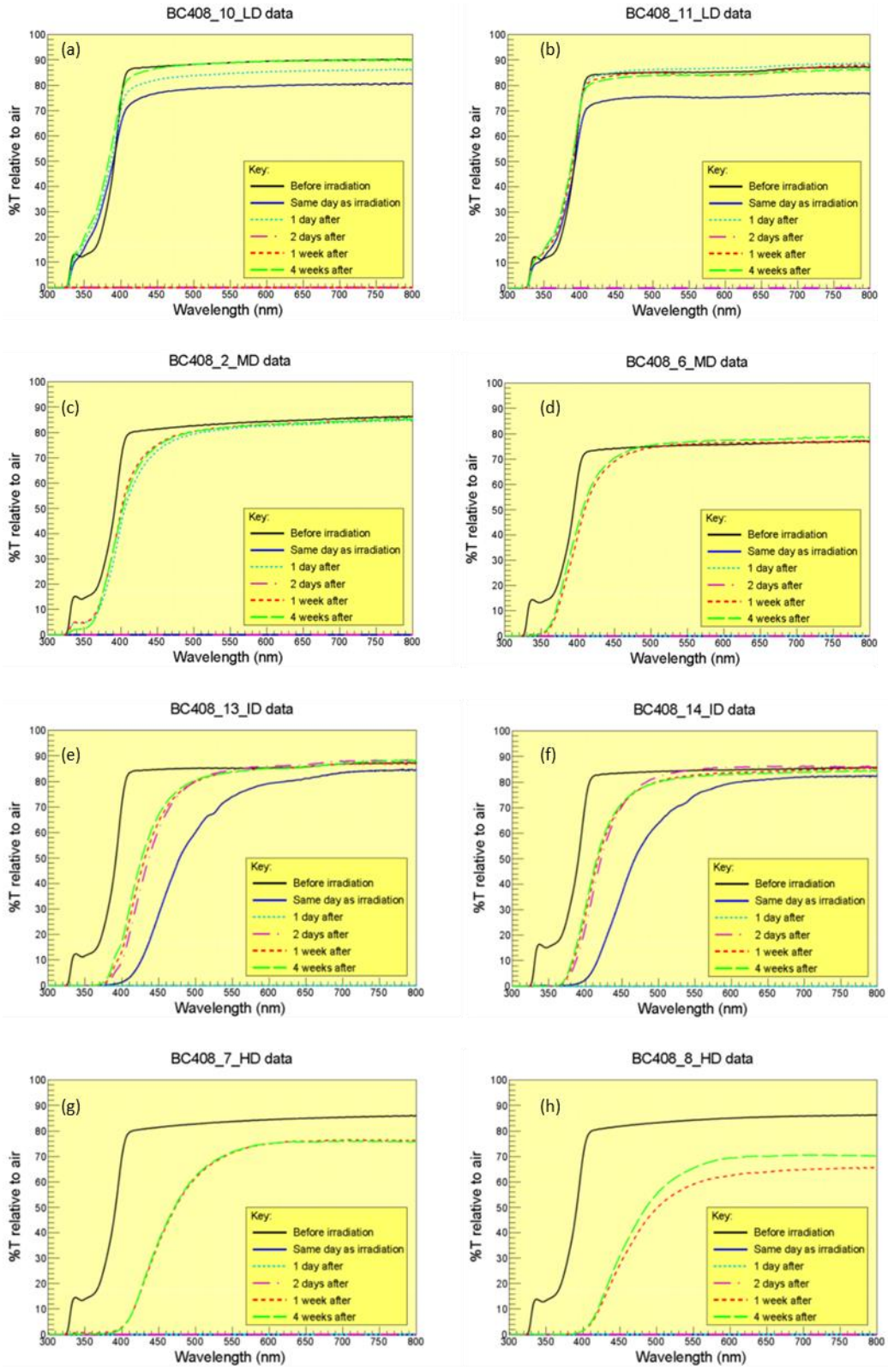


Figure C-1: Transmission spectra relative to air for BC408 samples irradiated to doses of: (a) 1.06, (b) 1.00, (c) 8.07, (d) 8.44, (e) 29.2, (f) 26.0, (g) 82.9 and (h) 97.2 MGy.

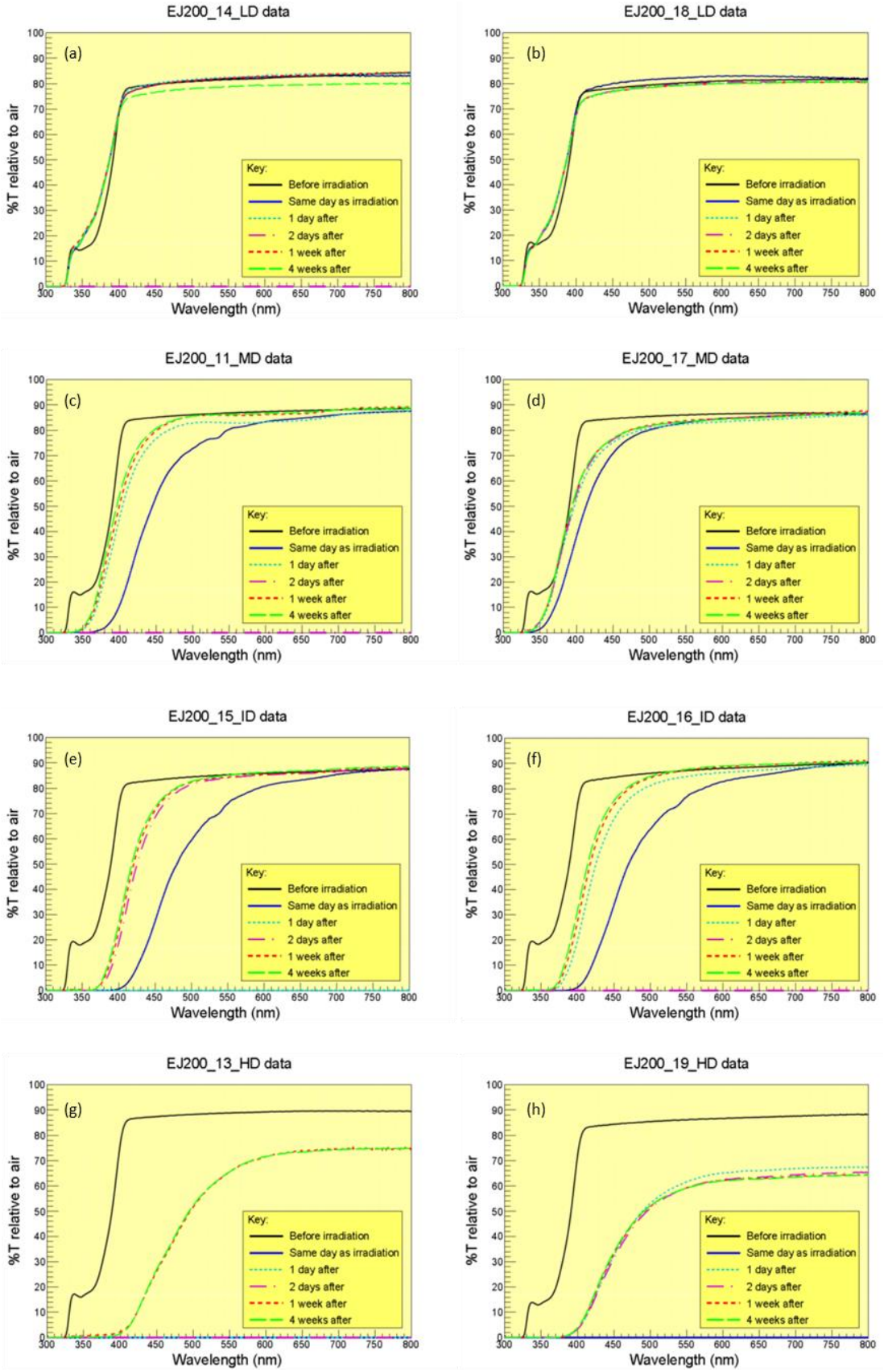


Figure C-2: Transmission spectra relative to air for EJ200 samples irradiated to doses of: (a) 0.90, (b) 1.08, (c) 8.06, (d) 8.11, (e) 25.8, (f) 25.7, (g) 76.1 and (h) 73.1 MGy.

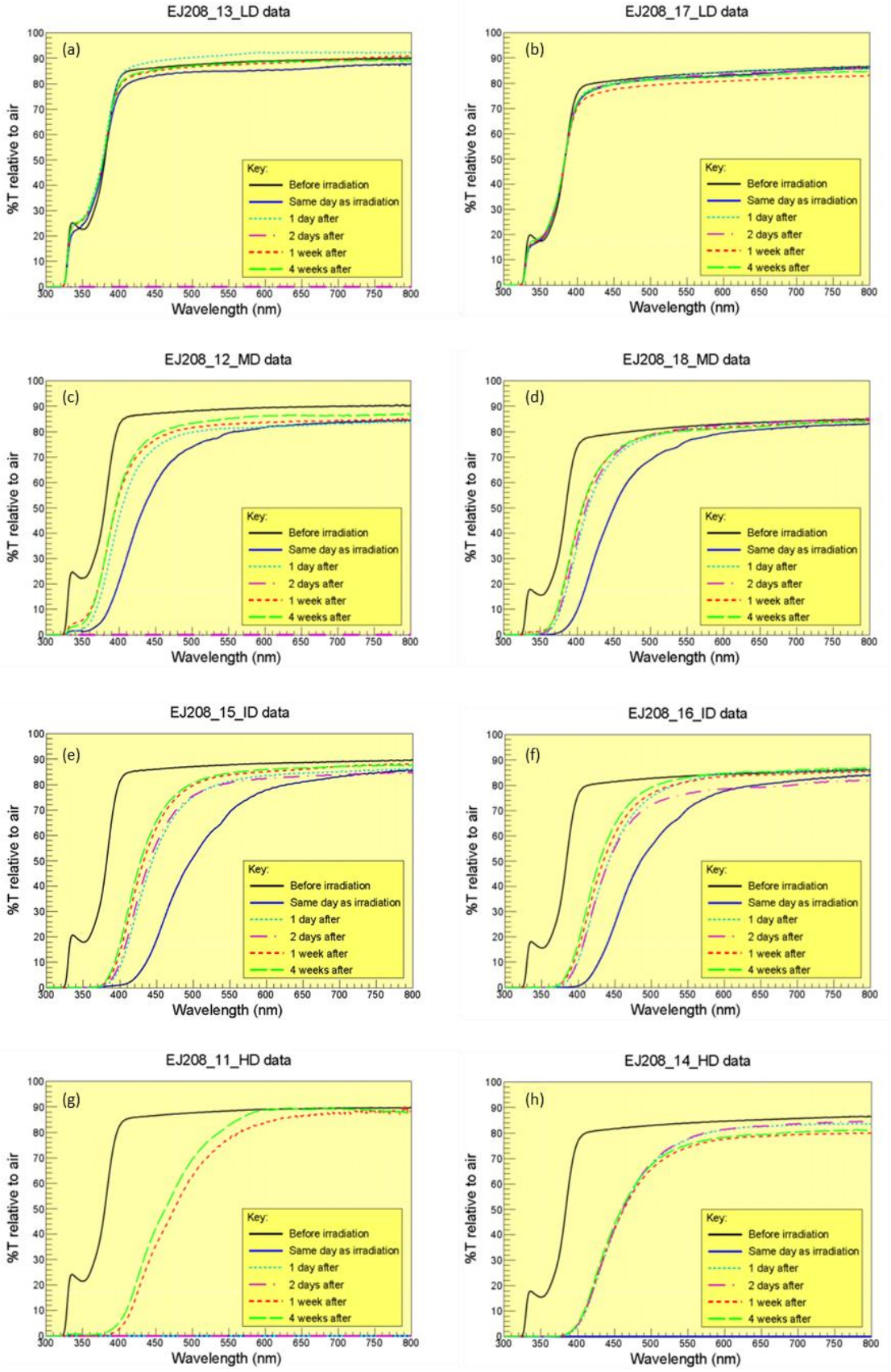


Figure C-3: Transmission spectra relative to air for EJ208 samples irradiated to doses of: (a) 0.858, (b) 0.825, (c) 8.80, (d) 8.30, (e) 24.8, (f) 26.4, (g) 80.8 and (h) 83.1 MGy.

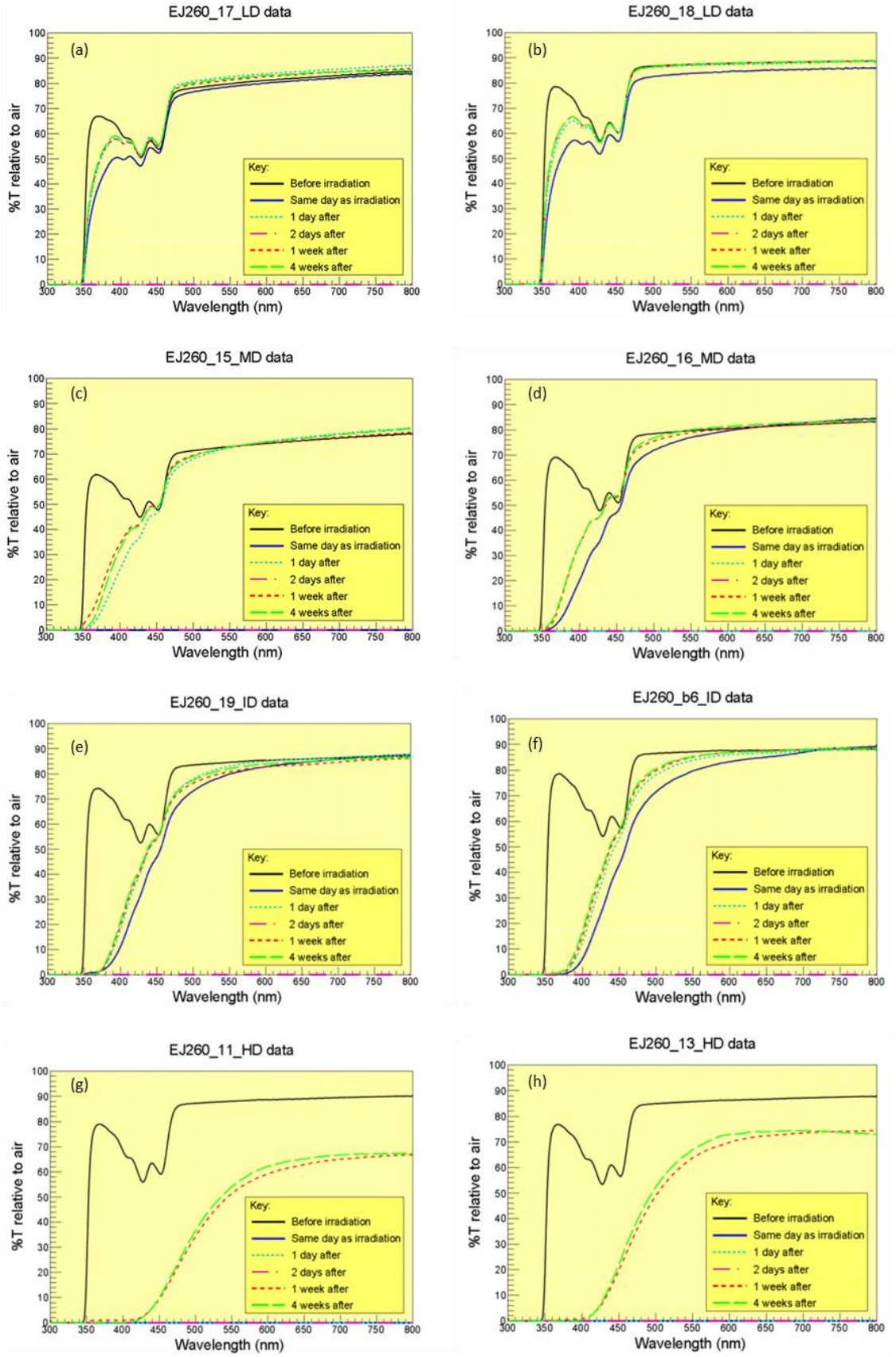


Figure 6-4: Transmission spectra relative to air for EJ260 samples irradiated to doses of: (a) 1.18, (b) 1.07, (c) 8.88, (d) 8.54, (e) 22.7, (f) 26.2, (g) 94.2 and (h) 86.5 MGy.

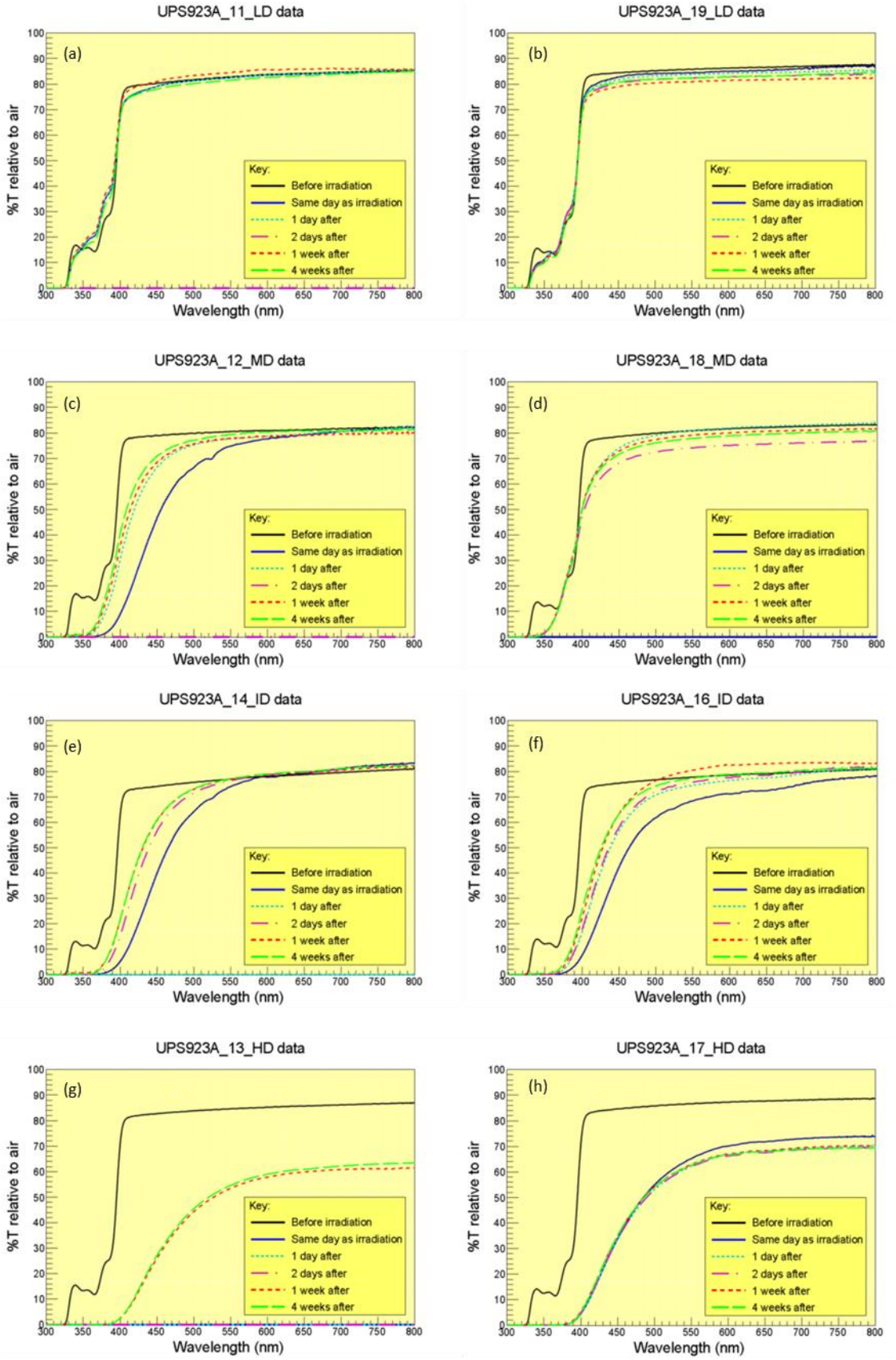


Figure C-5: Transmission spectra relative to air for UPS923A samples irradiated to doses of: (a) 0.934, (b) 0.904, (c) 10.7, (d) 6.50, (e) 25.7, (f) 28.3, (g) 81.6 and (h) 86.2 MGy.

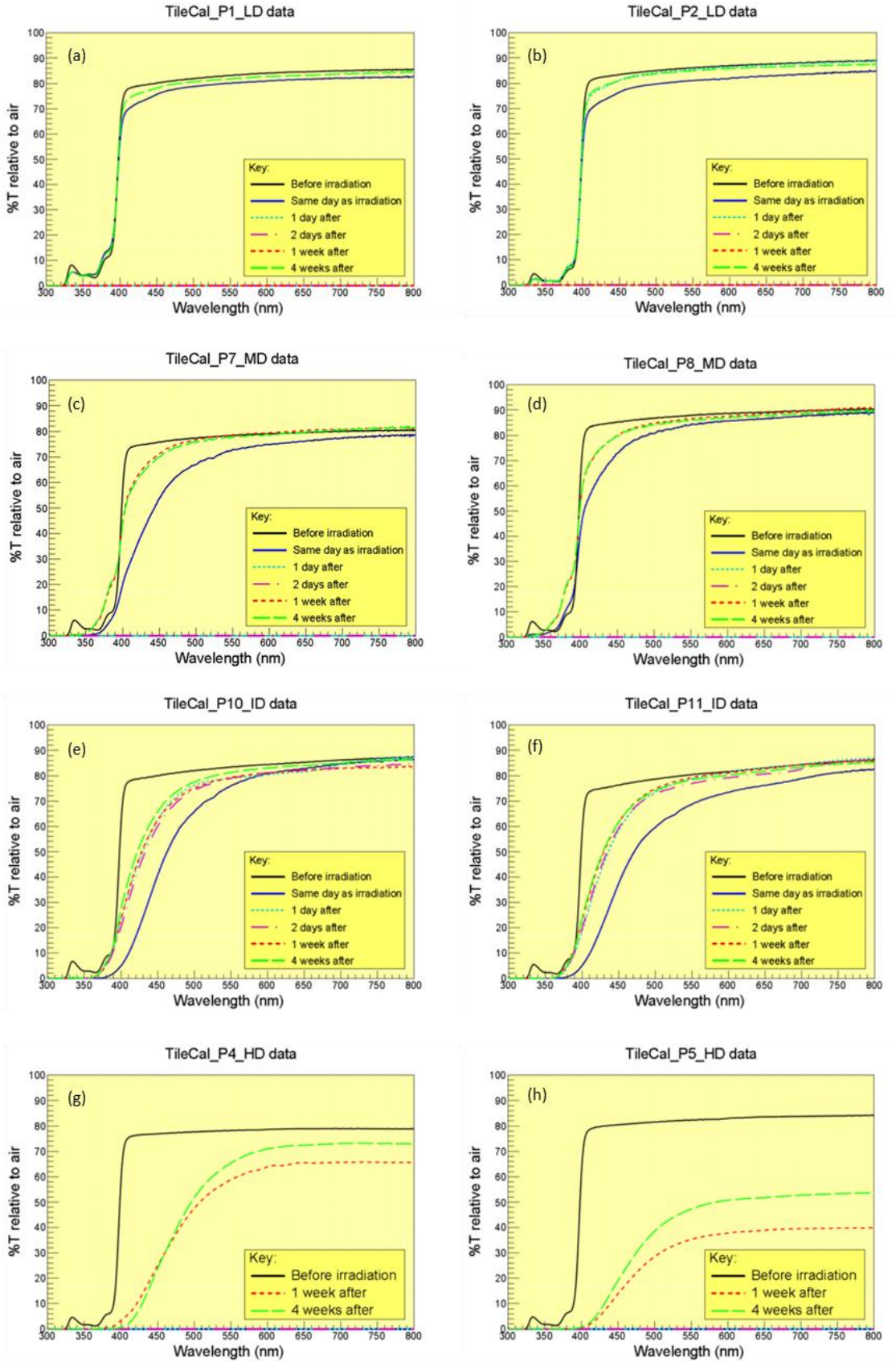


Figure C-6: Transmission spectra relative to air for TileCal samples irradiated to doses of: (a) 0.955, (b) 0.948, (c) 8.23, (d) 6.60, (e) 25.7, (f) 25.3, (g) 88.9 and (h) 78.5 MGy.

Appendix D

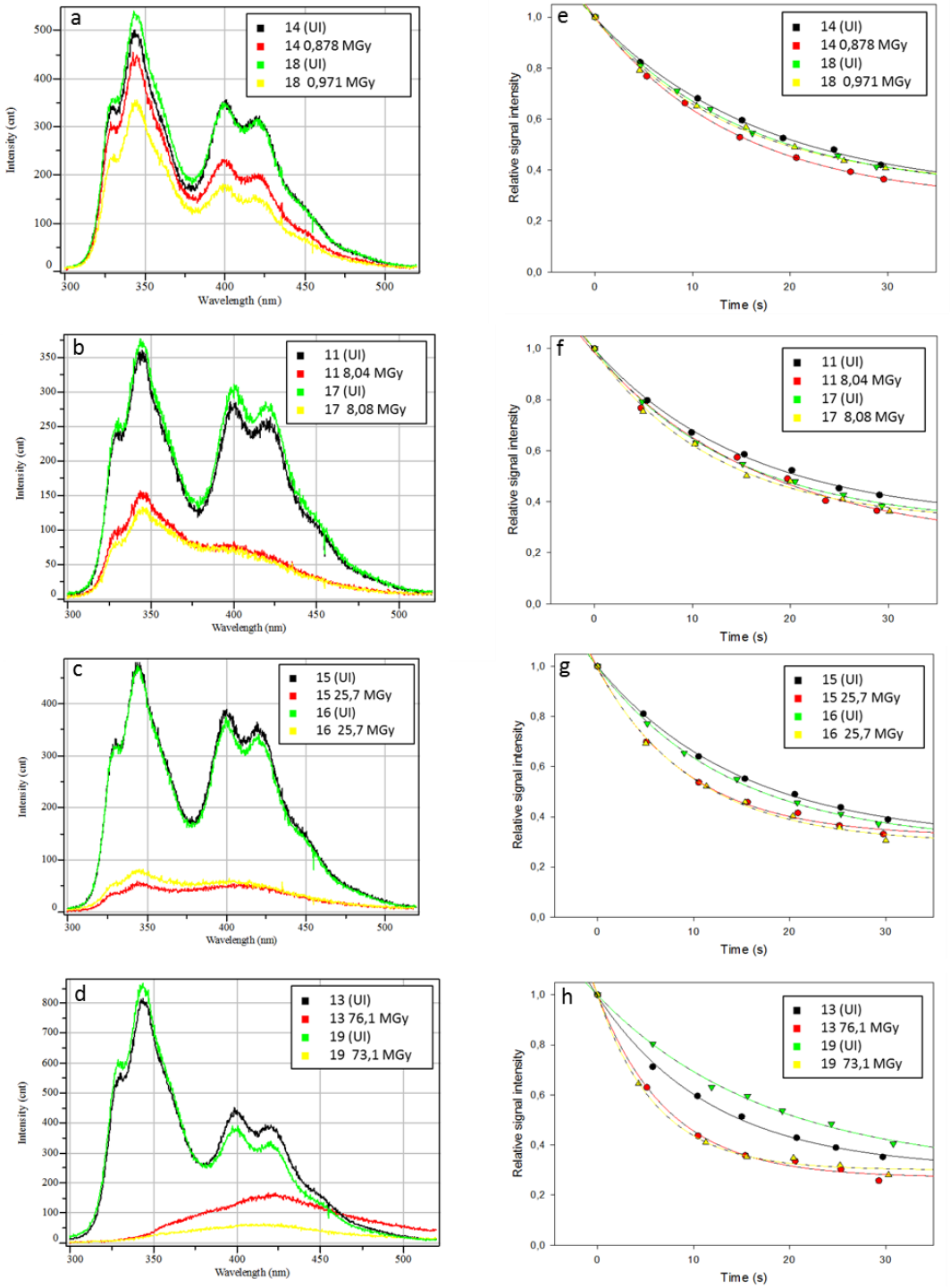


Figure D-1: Fluorescence spectra for various EJ200 samples (a-d), and their respective photo-bleaching rate curves (e-h).

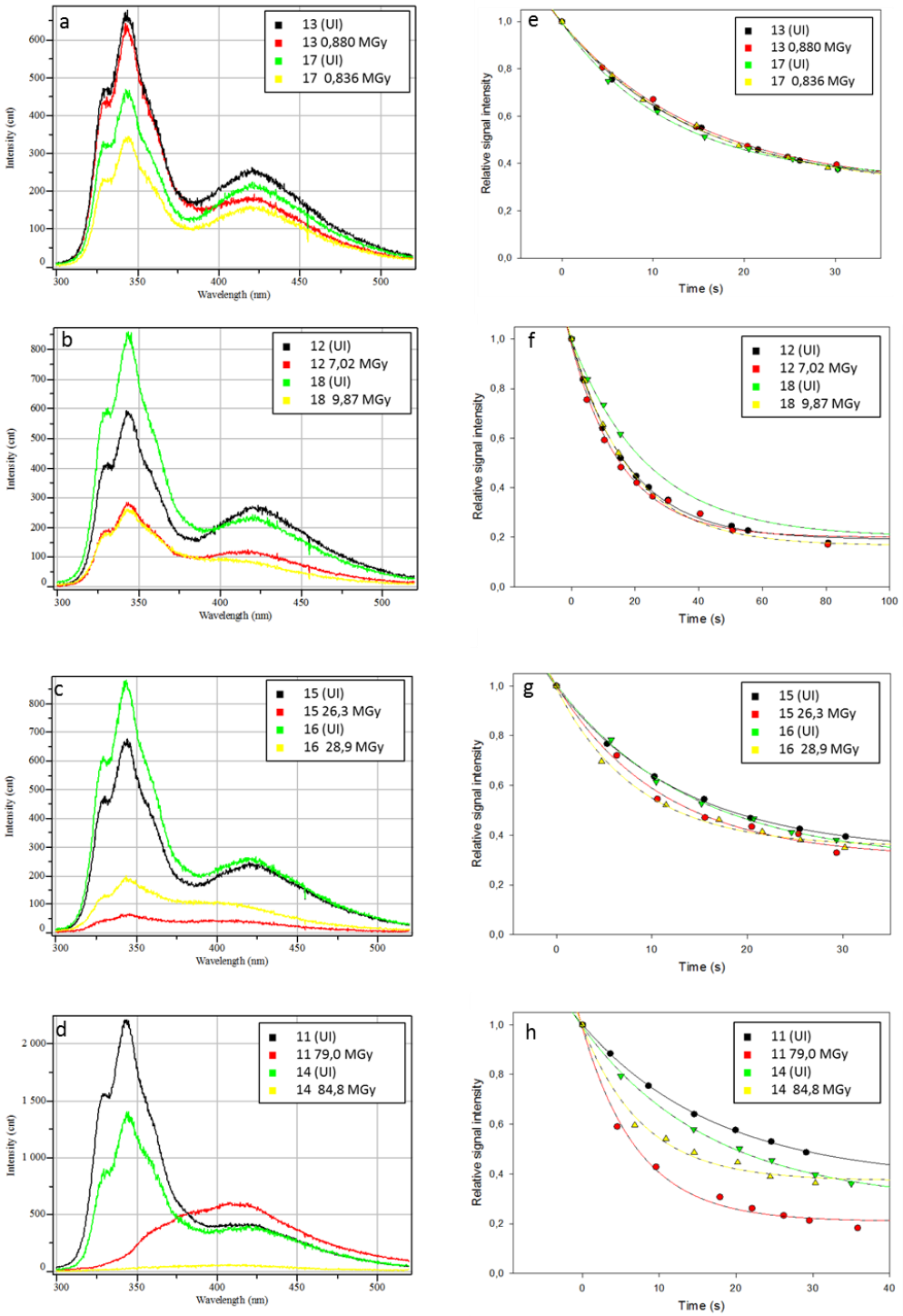


Figure D-2: Fluorescence spectra for various EJ208 samples (a-d), and their respective photo-bleaching rate curves (e-h).

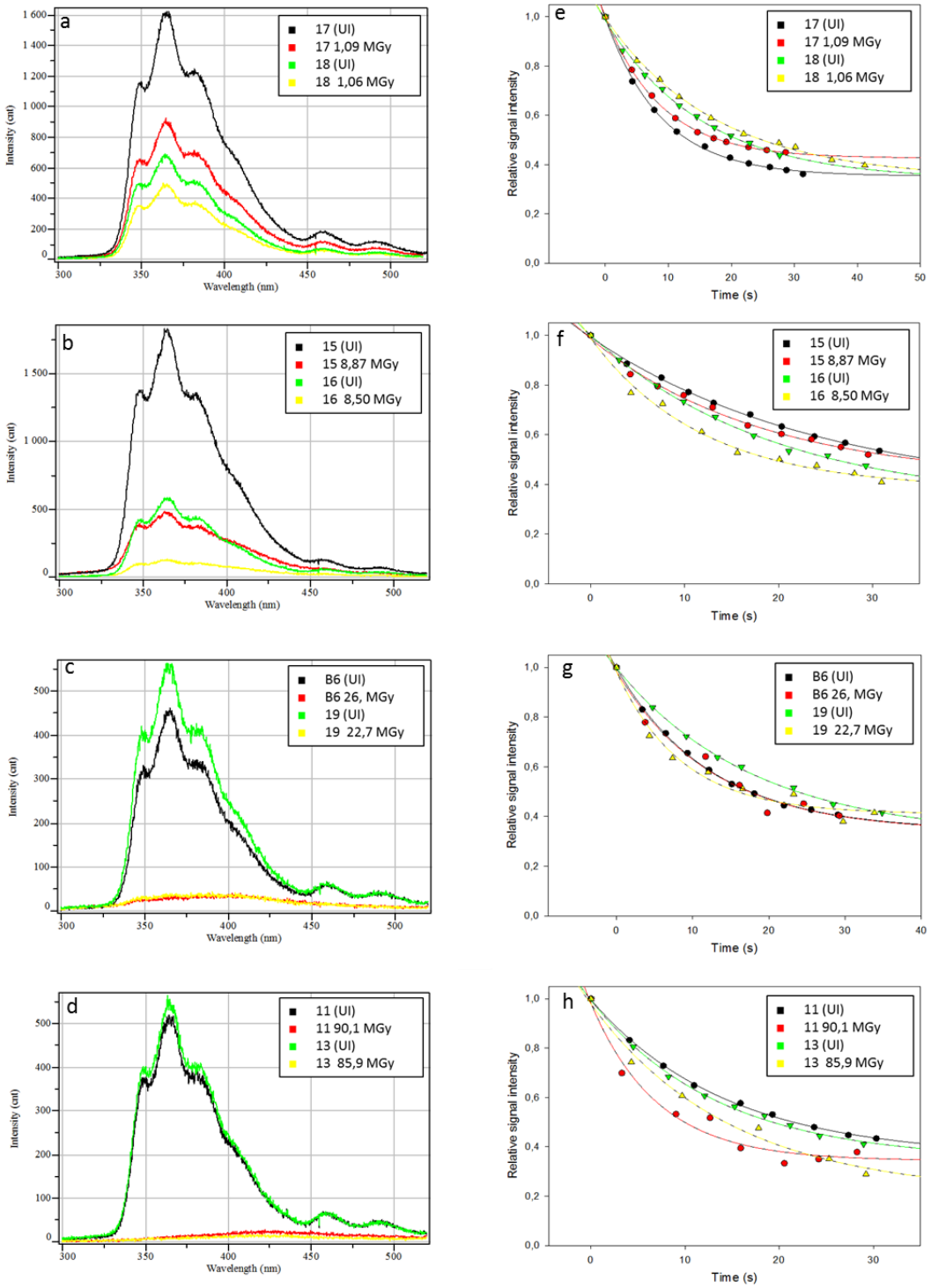


Figure D-3: Fluorescence spectra for various EJ260 samples (a-d), and their respective photo-bleaching rate curves (e-h).

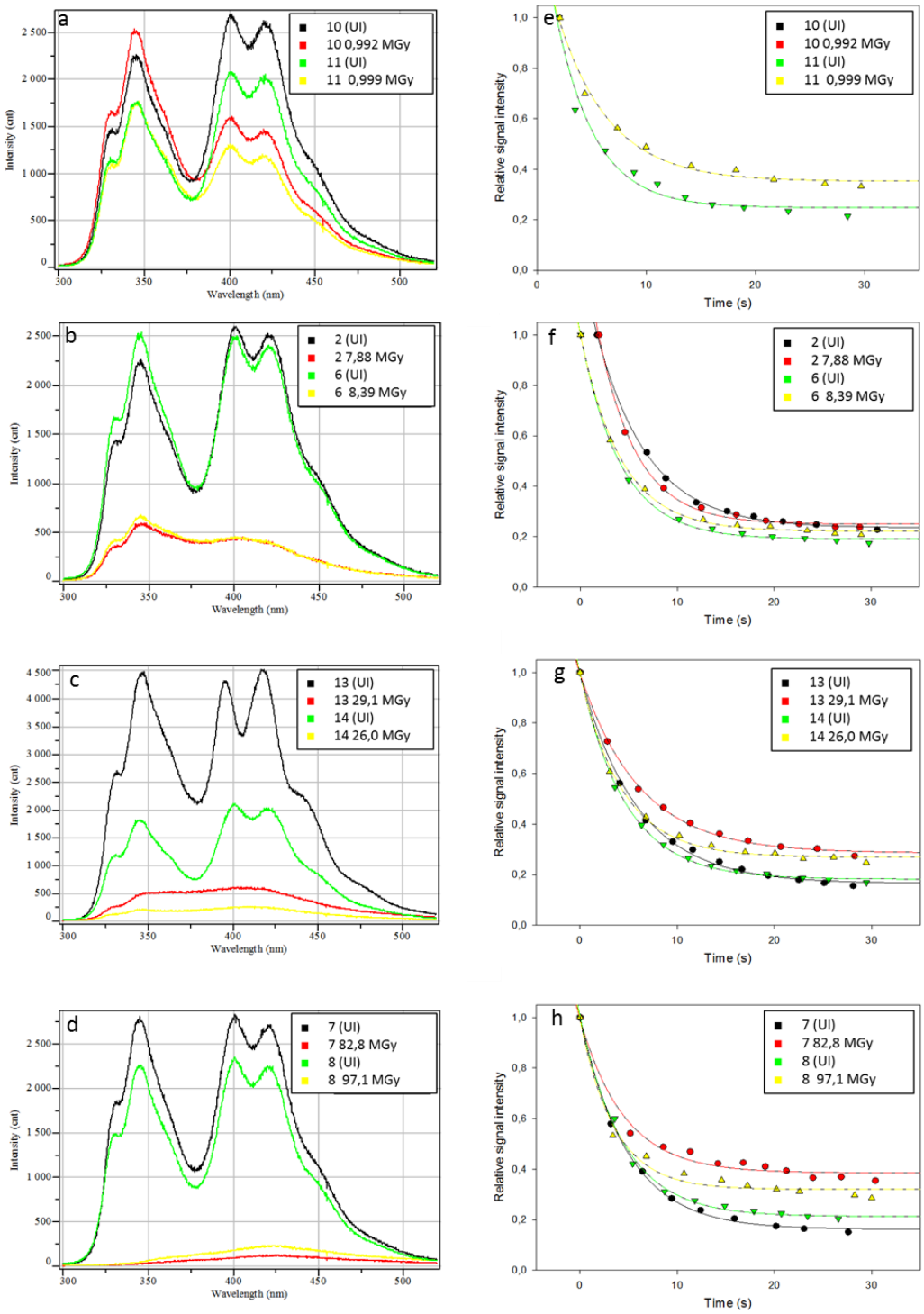


Figure D-4: Fluorescence spectra for various BC408 samples (a-d), and their respective photo-bleaching rate curves (e-h).

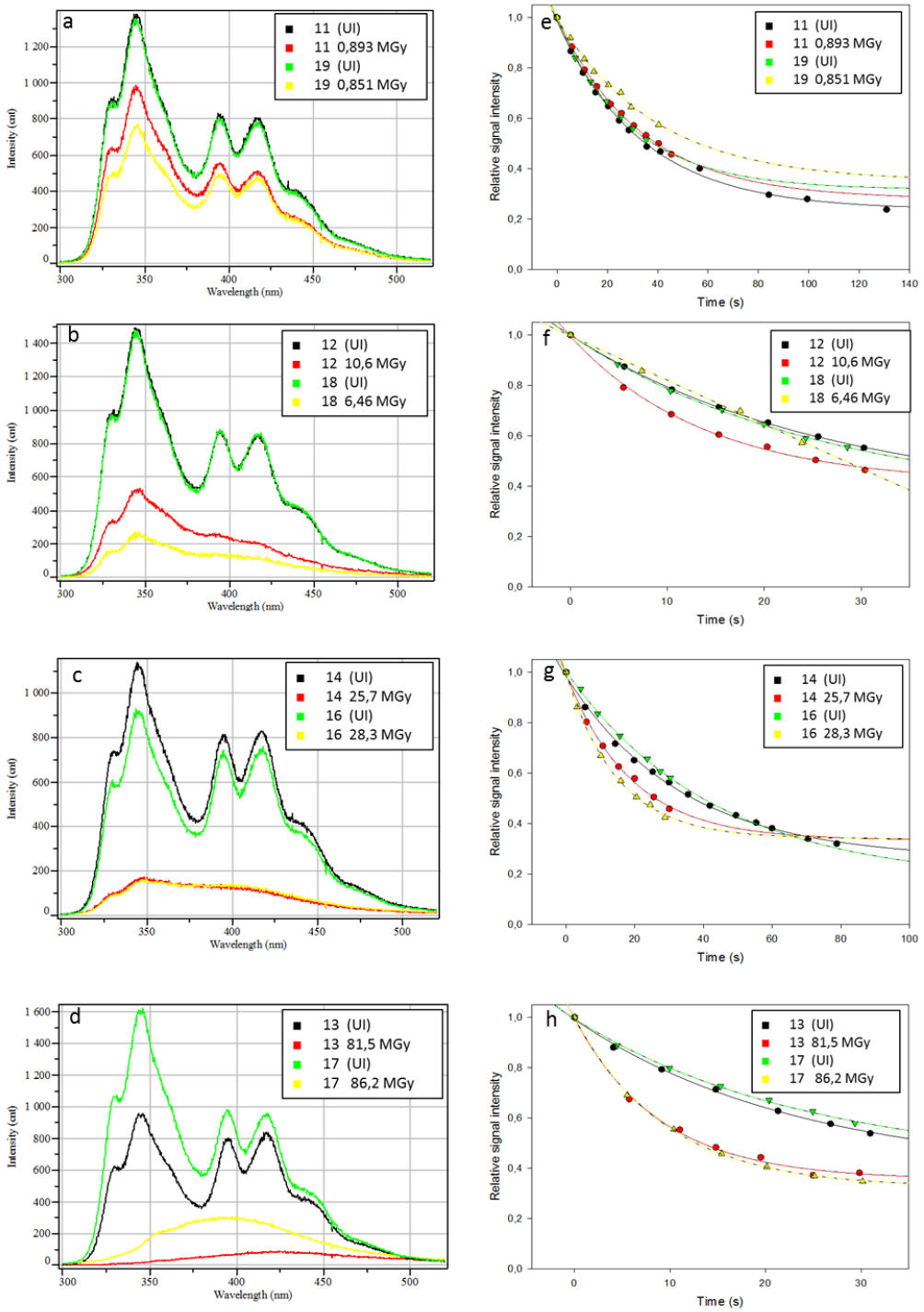


Figure D-5: Fluorescence spectra for various UPS923A samples (a-d), and their respective photo-bleaching rate curves (e-h).

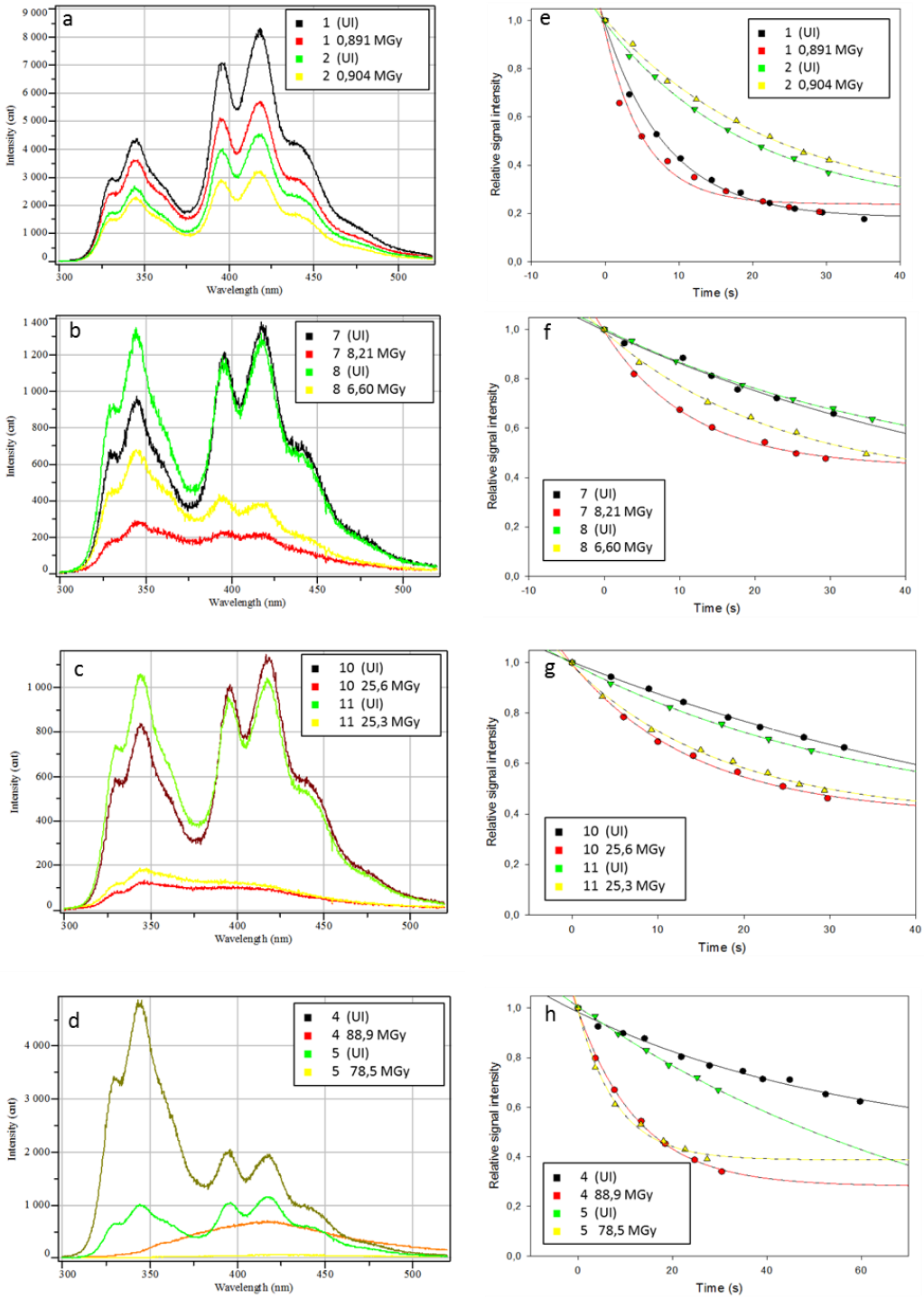


Figure D-6: Fluorescence spectra for various Tile Cal samples (a-d), and their respective photo-bleaching rate curves (e-h).

Appendix E

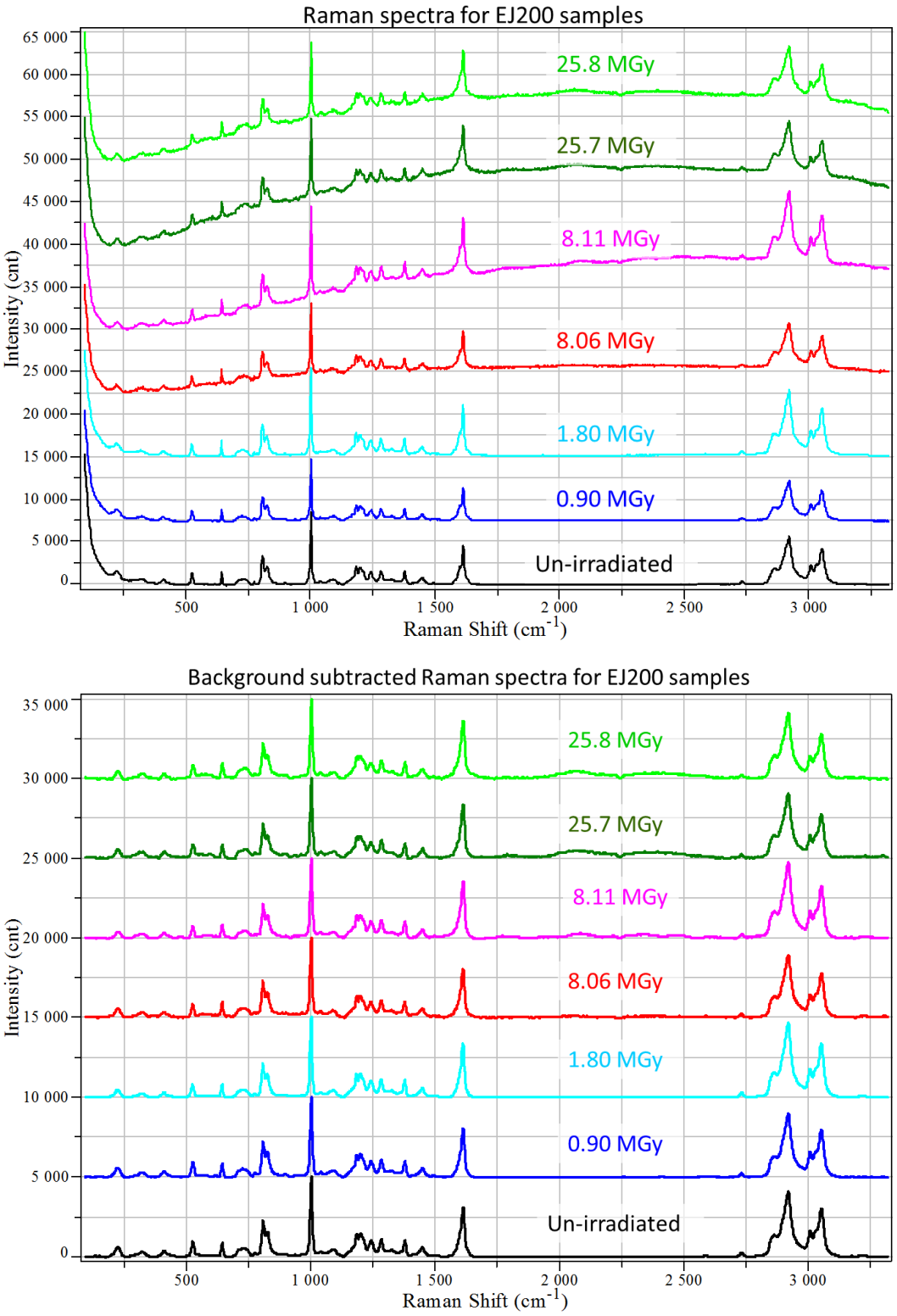


Figure E-1: Raman spectra for EJ200 samples.

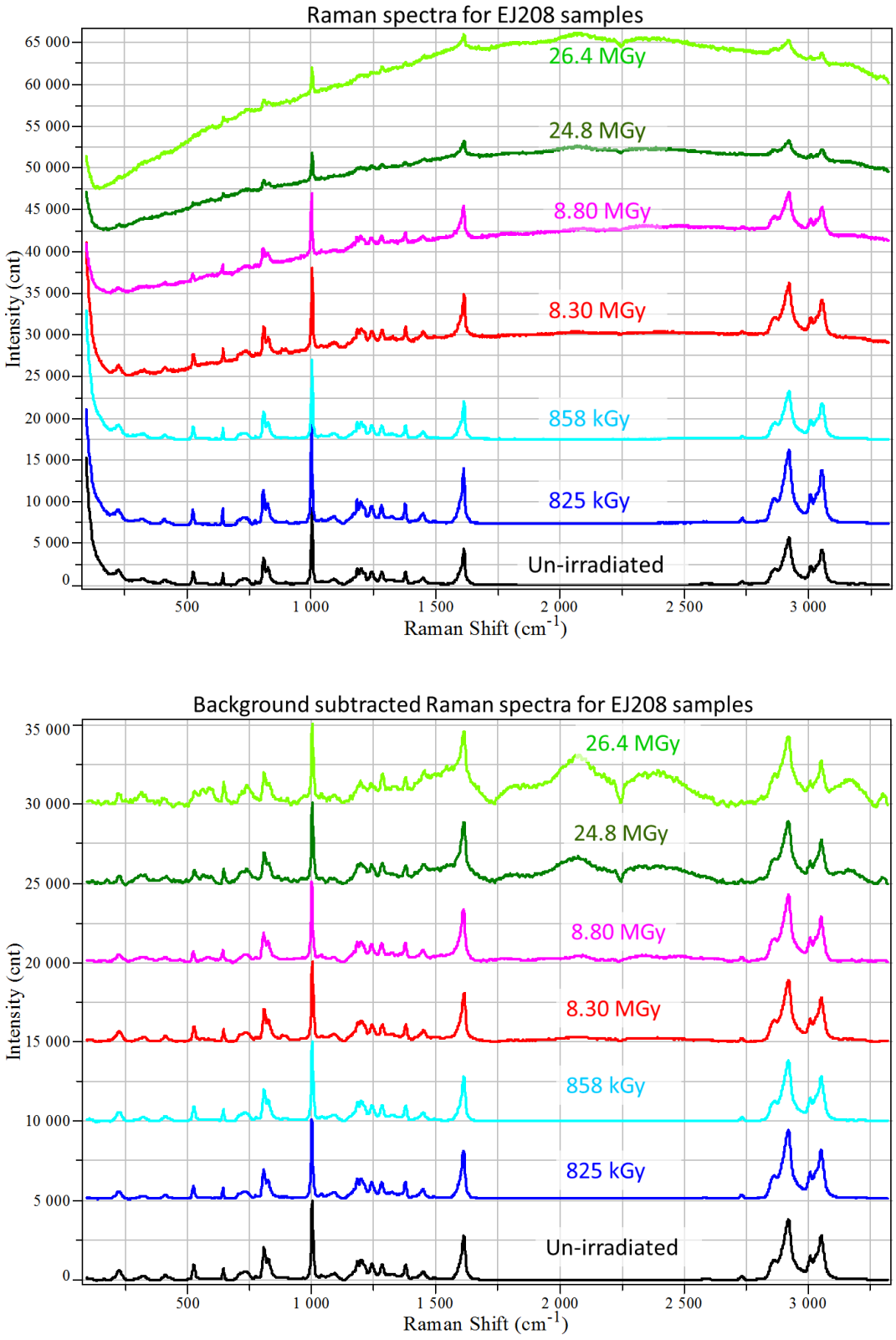


Figure E-2: Raman spectra for EJ208 samples.

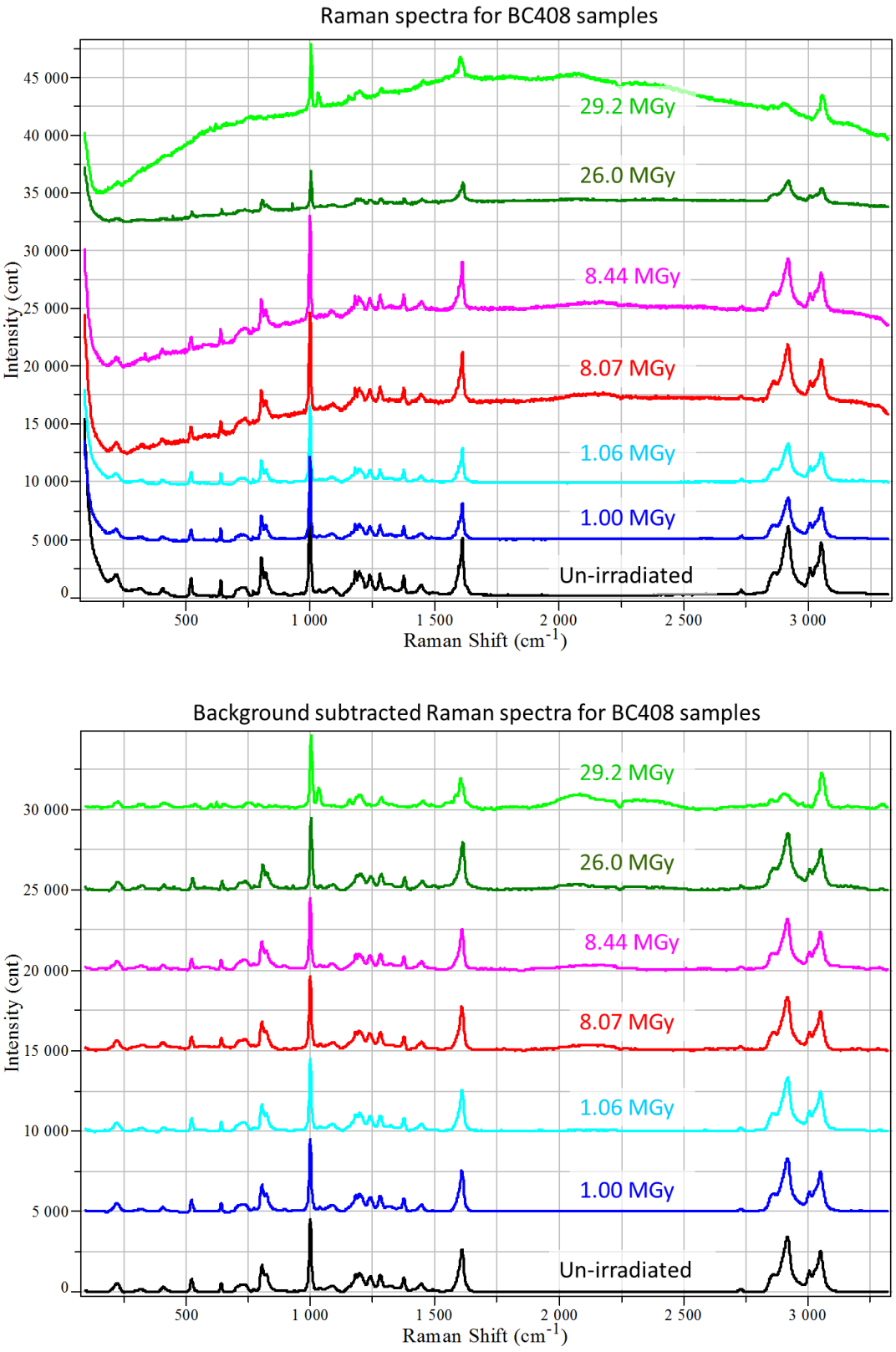


Figure E-3: Raman spectra for BC408 samples.

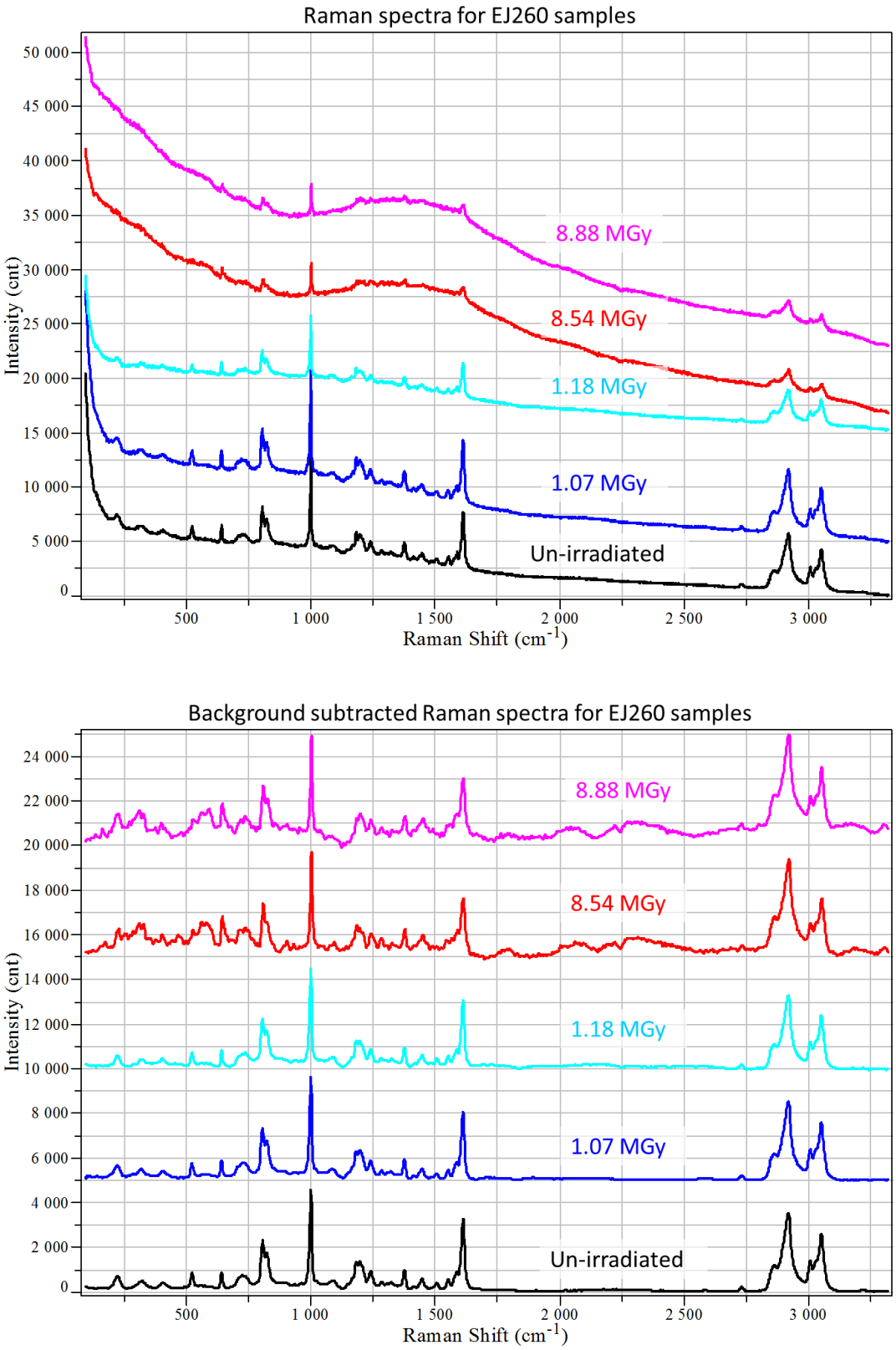


Figure E-4: Raman spectra for EJ260 samples.

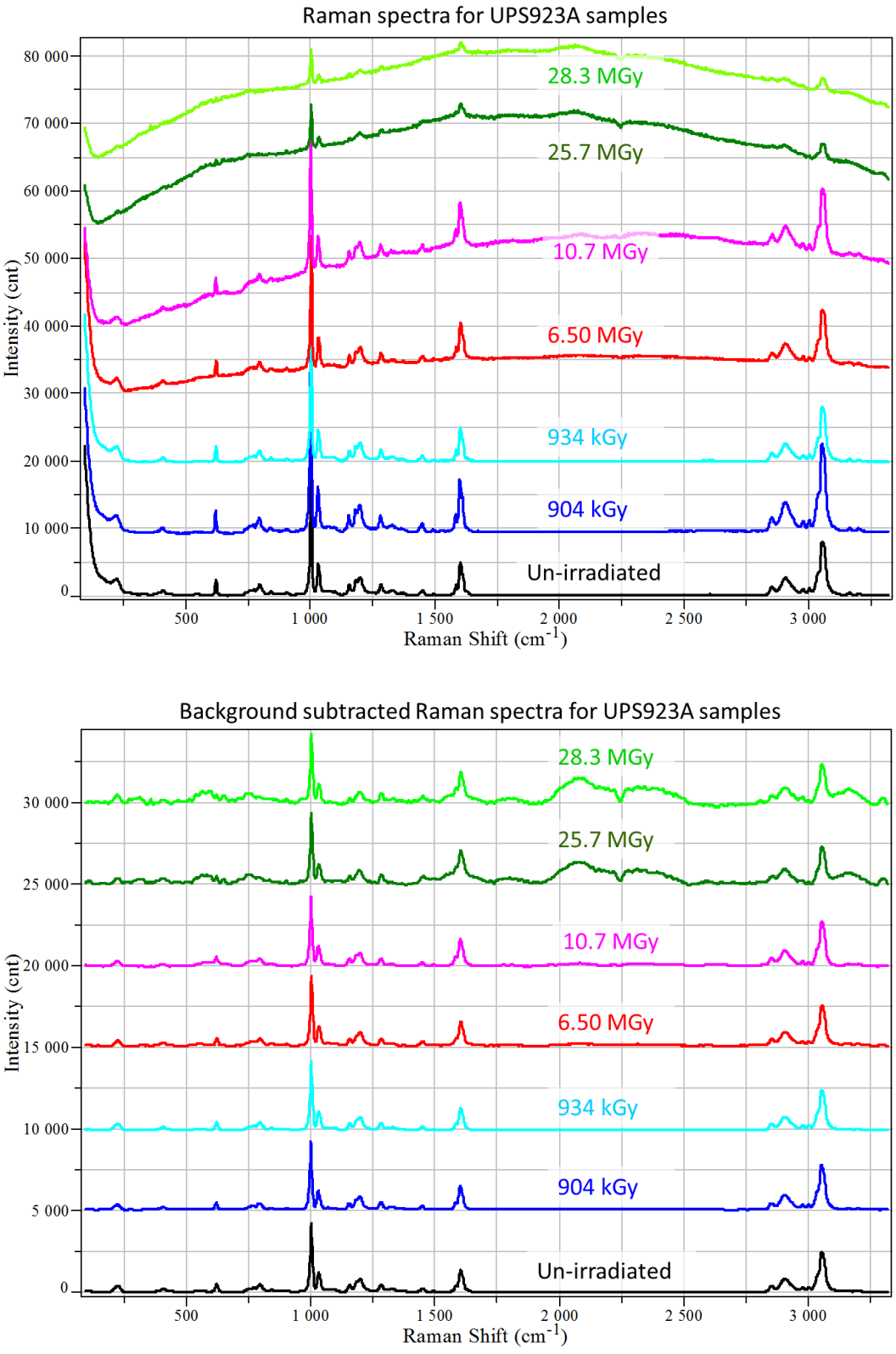


Figure E-5: Raman spectra for UPS923A samples.

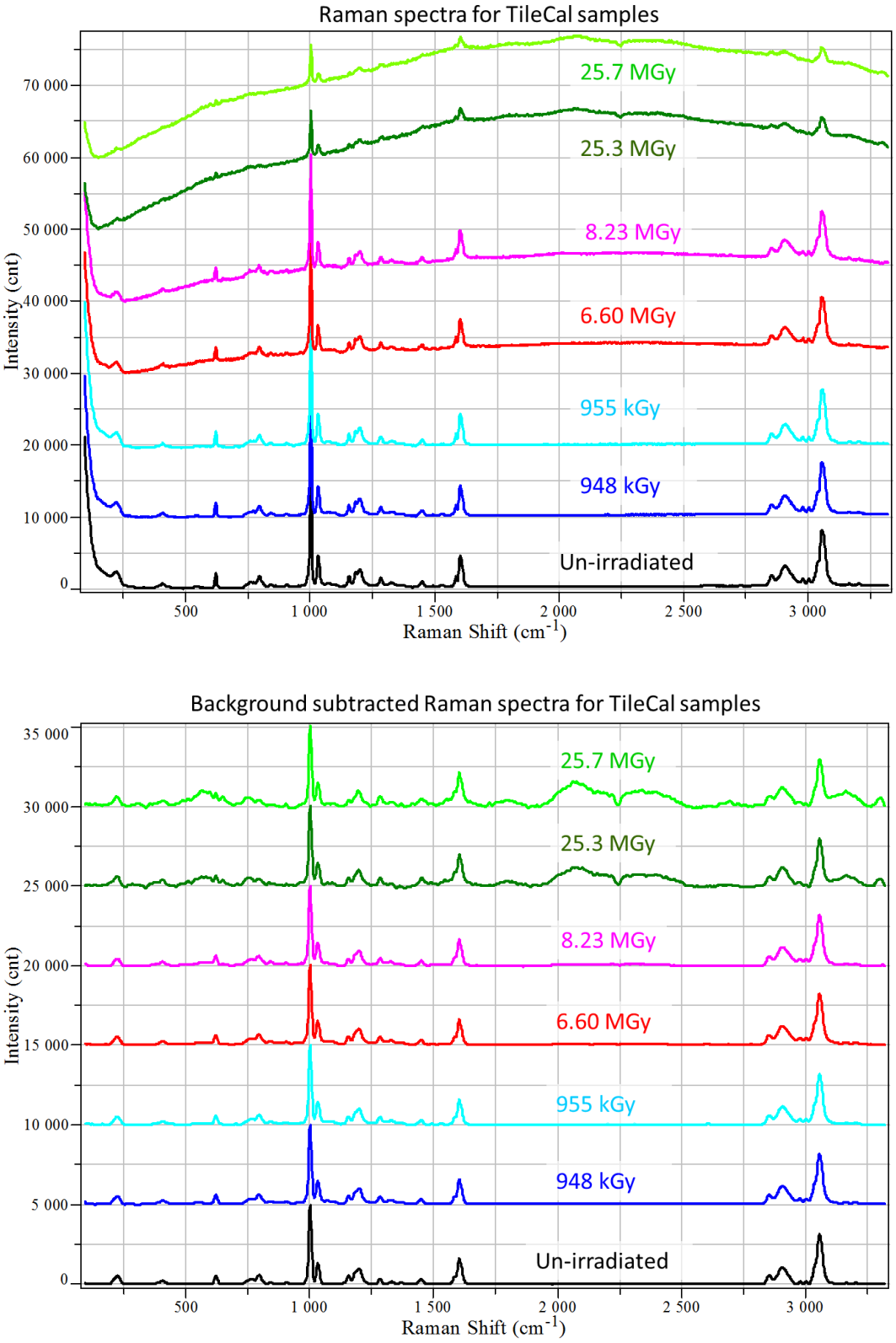


Figure E-6: Raman spectra for Tile Cal samples.

Appendix F



HORIBA JOBIN YVON Raman Application Note

RAMAN DATA AND ANALYSIS

Raman Spectroscopy for Analysis and Monitoring

The Raman scattering technique is a vibrational molecular spectroscopy which derives from an inelastic light scattering process. With Raman spectroscopy, a laser photon is scattered by a sample molecule and loses (or gains) energy during the process. The amount of energy lost is seen as a change in energy (wavelength) of the irradiating photon. This energy loss is characteristic for a particular bond in the molecule. Raman can best be thought of as producing a precise spectral fingerprint, unique to a molecule or indeed and individual molecular structure. In this respect it is similar to the more commonly found FT-IR spectroscopy. However, unlike FT-IR, there are a distinct number of advantages when using Raman.

- ***Raman can be used to analyse aqueous solutions since it does not suffer from the large water absorption effects found with FT techniques.***
- ***The intensity of spectral features in solution is directly proportional to the concentration of the particular species***
- ***Raman spectra are generally robust to temperature changes***
- ***Raman requires little or no sample preparation. It does not need the use of Nujol, or KBr matrices and is largely unaffected y sample cell materials such as glass.***
- ***The use of a Raman microscope such as the LabRAM provides very high level of spatial resolution and depth discrimination, not found with the FT methods of analysis***

These advantages and its highly specific nature, mean that Raman has become a very powerful tool for analysis and chemical monitoring. Depending upon instrumentation, it is a technique which can be used for the analysis of solids, liquids and solutions and can even provide information on physical characteristics such as crystalline phase and orientation, polymorphic forms, and intrinsic stress.

Functional Group/ Vibration	Region	Raman	InfraRed
Lattice vibrations in crystals, LA modes	10 - 200 cm^{-1}	strong	strong
δ(CC) aliphatic chains	250 - 400 cm^{-1}	strong	weak
υ(Se-Se)	290 -330 cm^{-1}	strong	weak
υ(S-S)	430 -550 cm^{-1}	strong	weak
υ(Si-O-Si)	450 -550 cm^{-1}	strong	weak
υ(Xmetal-O)	150-450 cm^{-1}	strong	med-weak
υ(C-I)	480 - 660 cm^{-1}	strong	strong
υ(C-Br)	500 - 700 cm^{-1}	strong	strong
υ(C-Cl)	550 - 800 cm^{-1}	strong	strong
υ(C-S) aliphatic	630 - 790 cm^{-1}	strong	medium
υ(C-S) aromatic	1080 - 1100 cm^{-1}	strong	medium
υ(O-O)	845 -900 cm^{-1}	strong	weak
υ(C-O-C)	800 -970 cm^{-1}	medium	weak
υ(C-O-C) asym	1060 - 1150 cm^{-1}	weak	strong

1/2

Explore the future HORIBA

Raman Bands

υ(CC) alicyclic, aliphatic chain vibrations	600 - 1300 cm^{-1}	medium	Medium
υ(C=S)	1000 - 1250 cm^{-1}	strong	weak
υ(CC) aromatic ring chain vibrations	*1580, 1600 cm^{-1}	strong	medium
	*1450, 1500 cm^{-1}	medium	medium
	*1000 cm^{-1}	strong/medium	weak
δ(CH3)	1380 cm^{-1}	medium	strong
δ(CH2) δ(CH3) asym	1400 - 1470 cm^{-1}	medium	medium
δ(CH2) δ(CH3) asym	1400 - 1470 cm^{-1}	medium	medium
υ(C-(NO2))	1340 - 1380 cm^{-1}	strong	medium
υ(C-(NO2)) asym	1530 - 1590 cm^{-1}	medium	strong
υ(N=N) aromatic	1410 - 1440 cm^{-1}	medium	-
υ(N=N) aliphatic	1550 - 1580 cm^{-1}	medium	-
δ(H2O)	~1640 cm^{-1}	weak broad	strong
υ(C=N)	1610 - 1680 cm^{-1}	strong	medium
υ(C=C)	1500 - 1900 cm^{-1}	strong	weak
υ(C=O)	1680 - 1820 cm^{-1}	medium	strong
υ(C≅C)	2100 - 2250 cm^{-1}	strong	weak
υ(C≅N)	2220 - 2255 cm^{-1}	medium	strong
υ(-S-H)	2550 - 2600 cm^{-1}	strong	weak
υ(C–H)	2800 - 3000 cm^{-1}	strong	strong
υ(=(C-H))	3000 - 3100 cm^{-1}	strong	medium
υ(≅(C-H))	3300 cm^{-1}	weak	strong
υ(N-H)	3300 - 3500 cm^{-1}	medium	medium
υ(O-H)	3100 - 3650 cm^{-1}	weak	strong

HORIBA JOBIN YVON

(All HORIBA Jobin Yvon companies were formerly known as Jobin Yvon)

France : HORIBA Jobin Yvon S.A.S., 231 rue de Lille, 59650 Villeneuve d'Ascq. Tel : +33 (0)3 20 59 18 00, Fax : +33 (0)3 20 59 18 08. Email : raman@jobinyvon.fr www.jobinyvon.fr
USA : HORIBA Jobin Yvon Inc., 3880 Park Avenue, Edison, NJ 08820-3012. Tel : +1-732-494-8660, Fax : +1-732-549-2571. Email : raman@jobinyvon.com www.jobinyvon.com
Japan : HORIBA Ltd., JY Optical Sales Dept., 1-7-8 Higashi-kanda, Chiyoda-ku, Tokyo 101-0031. Tel: +81 (0)3 3861 8231, Fax: +81 (0)3 3861 8259. Email: raman@horiba.com
Germany: +49 (0) 6251 84 75-0 **Italy:** +39 02 57603050 **UK:** +44 (0)20 8204 8142
China: +86 (0) 10 6849 2216

References

[1] G. F. Knoll, “Chapter 8: Organic Scintillators,” in *Radiation Detection and Measurement, Third Edition*, Michigan, John Wiley & Sons, Inc., 1999, pp. 220-222.

[2] ATLAS, “ATLAS News,” October 2012. [Online]. Available: http://www.atlas.ch/news/2012/atlas-and-the-higgs.html.

[3] M. Chen, “Queen's University, PHYS 352: Measurement, Instrumentation and Experiment Design,” 4 May 2011. [Online]. Available: http://www.physics.queensu.ca/~phys352/lect19.pdf.

[4] V. D. Shiltsev, “High energy particle colliders: Past 20 years, next 20 years and beyond,” *Physics-Usphekhi*, vol. 55, no. 10, p. 965, 2012.

[5] ATLAS Collaboration, “ATLAS Detector and physics performance Technical Design Report Vol. 1,” *CERN/LHCC 99-14*, 25 May 1999.

[6] E. Daw, “Lecture 7 - Rapidity and Pseudorapidity,” 23 March 2012. [Online]. Available: http://www.hep.shef.ac.uk/edaw/PHY206/Site/2012_course_files/phy206rlec7.pdf.

[7] ATLAS collaboration, “ATLAS Tile Calorimeter Technical Design Report,” *CERN/LHCC/96-42*, 1996.

[8] The ATLAS Tile Calorimeter community, “The optical instrumentation of the ATLAS Tile Calorimeter,” *Journal of Instrumentation*, vol. 8, no. 01, p. P01005, 2013.

[9] ATLAS Collaboration, “The ATLAS Experiment at the CERN Large Hadron Collider,” IOP Publishing and SISSA, 2008.

[10] K. Anderson, T. Del Prete, E. Fullana, J. Huston, C. Roda and R. Sttanek, “TILECAL: The Hadronic section of the central ATLAS Calorimeter,” *International Journal of Modern Physics A*, vol. 25, no. 10, pp. 1981-2003, 2010.

[11] C. Zeitnitz and T. Gabriel, “The GEANT-CALOR interface, User's guide (Version 1.05/03),” [Online]. Available: www.atlas.uni-wuppertal.de/zeitnitz/docs/gcalor/gcalor_manual.ps.

[12] A. Ferrari, P. Sala, A. Fasso and J. Ranft, “FLUKA: A multi-particle transport code (Programe version 2005)”.

[13] S. Baranov, M. Bosman, I. Dawson, V. Hedberg, A. Nisati and M. Shupe, “Estimation of Radiation Background, Impact on Detectors, Activation and Shielding Optimization in ATLAS,” *ATL-GEN-2005-00,* 13 January 2005.

[14] A. Sidoti, “Minimum Bias Trigger Scintillators in ATLAS Run II,” in *International Conference on Instrumentation for Colliding Beam Physics*, Novosibirsk, 2014.

[15] C. Zorn, “A pedestrian's guide to radiation damage in plastic scintillators,” *Radiation Physics and Chemistry,* vol. 41, no. 1/2, pp. 37-43, 1993.

[16] Universität Heidelberg, “Scintillation Detectors: Particle Detection via Luminescence,” May 2011. [Online]. Available: http://www.kip.uni-heidelberg.de/~coulon/Lectures/Detectors/Free_PDFs/Lecture4.pdf.

[17] L. Torrisi, “Radiation damage in polyvinyltoluene (PVT),” *Radiation Physics and Chemistry,* no. 63, p. 89–92, 2002.

[18] K. Wick, D. Paul, P. S. V. Schroder and B. Bicken, “Recovery and dose rate dependence of radiation damage in scintillators, wavelength shifters and light guides,” *Nuclear Instruments and Methods in Physics Research B,* vol. 61, pp. 472-486, 1991.

[19] W. Busjan, K. Wick and T. Zoufal, “Shortlived absorption centers in plastic scintillators and their infuence on the fuorescence light yield,” *Nuclear Instruments and Methods in Physics Research B,* no. 152, pp. 89-104, 1999.

[20] C. Zorn, S. Majewski and R. Wojcik, “Preliminary study of radiation damage in liquid scintllators,” *IEEE Transactions on Nuclear Science,* vol. 37, no. 2, pp. 487-491, 1990.

[21] ELJEN Technology, “Products: Plastic Scintilators,” [Online]. Available: http://www.eljentechnology.com/index.php/products/plastic-scintillators.

[22] Saint-Gobain, “Plastic Scintilators Specifications,” 2015. [Online]. Available: http://www.crystals.saint-gobain.com/Plastic_Scintillators.aspx.

[23] ScintiTech, “Products: Plastic Scintillators,” 2014. [Online]. Available: http://www.scintitech.com/CompanyPage.aspx?MenuId=39&MainId=3.

[24] A. N. Karyukhin, S. V. Kopikov, M. E. Kostrikov, V. Lapin and A. Zaitsev, “Injection molding scintillator for ATLAS Tile Calorimeter,” *ATL-TILECAL-96-086, ATL-L-PN-86,* 14 October 1996.

[25] D. Jankowski and R. Stanek, “Response of ATLAS injection molded scntillator,” *ATLAS Internal Note, TILECAL-NO-010,* 18 April 1994.

[26] J. Ziegler, J. Biersack and M. Ziegler, “Chapter 7,” in *SRIM The Stopping and Range of Ions in Matter*, Maryland, SRIM Co., 2008.

[27] D. C. Zipperian, “Metallographic Specimen Preparation Basics,” [Online]. Available: http://www.metallographic.com/Technical/Basics.pdf.

[28] Kuraray Co., Ltd., “Wavelength shifting fibers,” [Online]. Available: http://kuraraypsf.jp/psf/ws.html.

[29] C. Pelwan, H. Jivan, D. Joubert, J. Keartland, S.-M. Liao, G. Peters and E. Sideras-Haddad, “Characterization of plastic scintillators using magnetic resonance techniques for the upgrade of the Tile Calorimeter in the ATLAS detector,” in *Journal of Physics: Conference Series 645 012023*, Johannesburg, 2015.

[30] S. Tlou, H. Jivan, B. Mellado, R. Erasmus, M. Madhuku, K. Sekonya and E. Sideras-Haddad, “Impact of dose rate on radiation damage of plastics scintillators for the Tile Calorimeter of ATLAS,” in *submitted to Proceedings of SAIP2015*, Port Elizabeth, 2015.

[31] G. Socrates, Infrared and Raman Characteristic Group Frequencies Tables and Charts, John Wiley and Sons, 2004.

[32] J. Clark, “Bonding in benzene,” 2000. [Online]. Available: http://www.chemguide.co.uk/basicorg/bonding/benzene2.html.

[33] E. Dubreuil, “Calibrating and preserving the energy scale of the Tile Calorimeter cells during four years of LHC data-taking,” *Journal of latex class files*, vol. 11, no. 4, 2012.

[34] U. Holm, D. Horstmann and S. Schacht, “Oxygen diffusion and recovery of damage in irradiated polystyrene,” *Nuclear Instruments and Methods in Physics Research* , vol. B, no. 151, pp. 453-456, 1999.

[35] D. Horstmann and U. Holm, “Fluorescence quenching of plastic scintillators in oxygen,” *Radiation Physics and Chemistry*, vol. 41, no. 1/2, pp. 395-400, 1993.